Experimental investigation on low-temperature electrical resistivity of silver thin films

The effects of fabrication, design, purity and storage

Sezen Kadir

Delft University of Technology

TU Delft

Experimental investigation on low-temperature electrical resistivity of silver thin films

The effects of fabrication, design, purity and storage

by

Sezen Kadir

to obtain the degree of Master of Science
at the Delft University of Technology,
to be defended publicly on Monday November 13, 2023 at 13:00.

Student number:	5605369	
Project duration:	January, 2023 – November, 2023	
Thesis committee:	Dr. A. J. Böttger,	TU Delft, supervisor
	Dr. Ir. D. Bouman,	Delft Circuits, supervisor
	Dr. Ir. M. H. F. Sluiter	TU Delft

This thesis is confidential and cannot be made public until November 13, 2025.

Cover: Microstructure of a silver thin film
Style: TU Delft Report Style, with modifications by Daan Zwaneveld

TUDelft

Delft Circuits
Hardware for quantum engineers

Acknowledgements

Firstly, I would like to express my deepest gratitude to my supervisors, Dr. ir. Amarante Böttger and Dr. ir. Daniël Bouman, for their unwavering guidance and support throughout the project. Amarante, thank you for sharing your knowledge and expertise, which significantly enhanced the scientific depth of my thesis. I am profoundly grateful to Daniel, who was my daily supervisor, and always ready to address any questions or concerns. He ensured that I received the necessary guidance while providing me with the freedom to foster creativity and take initiative. His invaluable support proved essential to the successful completion of my thesis.

I would also like to extend my gratitude to Delft Circuits for placing their trust in me and providing the opportunity to work on a captivating project. Special thanks go to Daniel, Marina, and Jakob for creating this thesis project. My journey would have been incomplete without the support of my colleagues at Delft Circuits. Zyanya, Marina, Kiefer, Linda, and Djemaal were consistently available to train me on lab equipment, share their knowledge, and address any questions. They made the time in the lab an enjoyable experience and showed remarkable patience and understanding, even during my clumsiest moments. I'd also like to express my appreciation to Ruben and Art for their assistance with cryogenic measurements and for patiently dealing with my programming skills. Lastly, I would like to thank Wouter for providing vitamin C to ward off illness and for his valuable feedback during my thesis writing journey.

Furthermore, I extend my sincere gratitude to the laboratory technicians at the Materials Science and Engineering Department and the Applied Physics faculty. Kees Kwakernaak's assistance with SEM analysis significantly enriched the scientific content of my thesis and provided fresh perspectives on my samples. Ruud Hendrikx's contribution to XRD analysis was important in validating my theories. I also wish to acknowledge Olaf Benningshof for sharing his expertise with me at the outset of my thesis, as his insights greatly assisted in structuring my project.

I would also like to express my appreciation to Dionysis for his endless support and encouragement and for creating a safe space, no matter how challenging the day may have been, whether due to broken lab equipment, mysterious code errors, or the occasional lovely Dutch weather.

I extend my gratitude to Gee Whiz for making my time in Delft an enjoyable experience over the past two years. Our trips, drinks at the faculty pubs, and post-long-day dinners transformed this master's journey into an unforgettable adventure. I am grateful to have had the opportunity to meet you through this university. I offer a very special thanks to my friends in Turkey for their support and love, recharging me to embark on new adventures every time I return home.

Last but not least, I wish to express my deep appreciation for my parents and my brother for their enduring love and support. They have always been, and will continue to be, my solid foundation—a place I cherish returning to after life's rollercoasters.

Sezen Kadir
Delft, November 2023

Abstract

Quantum computing has gained a lot of interest from researchers and industry due to its great potential to solve some complex problems in various fields. One of the biggest challenges is developing hardware suitable for the extremely low operation temperatures required by quantum computers. Specifically, the wiring material of a quantum computer must provide good electrical conductivity while keeping the thermal load to a minimum. Delft Circuits' cryogenic flexible cable design made from metalized Polyimide (PI) with Silver (Ag) thin films as conductors offers a promising solution for quantum computer i/o systems. This thesis aims to investigate the effect of fabrication and design parameters on the electrical and thermal properties of silver thin films, utilizing the Residual Resistivity Ratio (RRR) as an indicator to assess the thermal load of cryogenic flexible cables. The RRR is calculated by taking the ratio of electrical resistivity measured at room temperature and extremely low temperatures of liquid He (4.2 K). The key parameters for the experimental investigation include oven heat treatment, lamination, silver purity, film thickness, aging and storage. The RRR behavior of samples with varying fabrication and design characteristics is explored through cryogenic measurements. Subsequently, the RRR results are analyzed and supported by material characterization via SEM and XRD. The results show that heat treatment results in higher RRR values due to grain growth and lower grain boundary density, leading to lower electrical resistivity at low temperatures. Heat treatment parameters including temperature, pressure, duration, ambiance, and cooling rate play a significant role in the resulting microstructure of the silver film, and consequently, in their RRR values. Furthermore, the study reveals that the lower purity level leads to decreased RRR values of the silver film due to higher electron scattering caused by impurities. A linear relationship is found between the film thickness and the RRR behavior of silver thin films. Lastly, aging and storage do not result in a significant change in the RRR values of heat-treated silver thin films. This thesis provides a deeper understanding on the influence of fabrication and design parameters on the low-temperature resistivity of silver thin films. It highlights the key role of these parameters in tailoring the microstructure of silver thin films to achieve desired material properties.

Key Words: Quantum computers, cryogenic flexible cables, silver thin films, electrical resistivity, heat load, residual resistivity ratio (RRR), heat treatment, purity, film thickness, aging and storage

Contents

Acknowledgements **i**

Abstract **ii**

1 Introduction **1**

2 Literature Review **3**
2.1 Motivation . . . 3
2.2 Current state of the Art . . . 4
2.3 Challenges . . . 4
2.4 Temperature dependence of electrical and thermal properties . . . 4
2.4.1 Electrical properties . . . 5
2.4.2 Thermal properties . . . 8
2.5 Metallic thin films . . . 12
2.5.1 Thin film technology . . . 12
2.5.2 Thin film deposition techniques . . . 12
2.5.3 Microstructural aspects of metallic thin film deposition . . . 13
2.6 Factors affecting low-temperature material properties . . . 15
2.6.1 Heat treatment . . . 15
2.6.2 Purity level . . . 21
2.6.3 Film thickness . . . 22
2.6.4 Aging and storage . . . 24
2.7 Concluding remarks . . . 25
2.8 Research question . . . 25

3 Materials and Methods **26**
3.1 Materials . . . 26
3.2 Methods . . . 27
3.2.1 Sample preparation . . . 27
3.2.2 Cryogenic measurements . . . 29
3.2.3 Data analysis . . . 32
3.2.4 Material characterization . . . 33

4 Results and Discussion **34**
4.1 Heat effects . . . 34
4.1.1 Lamination . . . 34
4.1.2 Oven heat treatment . . . 36
4.1.3 Comparison of oven heat treatment and lamination . . . 38
4.1.4 Spread investigation . . . 40
4.1.5 White surface finish . . . 45
4.2 Silver Purity . . . 50
4.3 Film Thickness . . . 52
4.4 Aging and Storage . . . 54

5 Conclusions and Recommendations **56**
5.1 Conclusions . . . 56
5.2 Future Recommendations . . . 57

References **58**

A Sample Data **61**

B RRR vs Film Thickness **67**

C Additional Figures **70**

1 Introduction

Quantum computing holds great promise in various industries, including materials, pharmaceuticals, finance, weather forecasting, and cybersecurity, thanks to its ability to harness quantum mechanics principles [1]. It can accelerate drug development, enhance financial decision-making, and improve weather predictions [2]. However, building quantum computers is challenging due to the need for extremely cold operation temperatures with limited cooling power and scalable hardware that is suitable for a complex quantum computer system [3]. Traditional coaxial cables are inadequate to meet these requirements. Flexible cables made from metalized polymer films like Polyimide (PI) with Silver (Ag) conductors offer a promising solution with their low weight, low volume, and flexibility. Delft Circuits is a scale-up company that develops and fabricates cryogenic flexible cables (Cri/oFlex) for the i/o system of quantum computers. This thesis is conducted in collaboration with Delft Circuits. The scope of this thesis centers on the effect of the fabrication steps of cryogenic flexible cables on the electrical and thermal characteristics of silver thin film.

In quantum applications, wiring materials must meet stringent requirements, including good electrical conductivity for efficient signal transmission while simultaneously maintaining a relatively low thermal conductivity to prevent excessive thermal loads on the system. PI films are suitable to be the substrate material for cryogenic and flexible cabling systems with their excellent mechanical, thermal, and electrical properties at low temperatures [4]. Ag also serves as an ideal conductor for flexible electronics, thanks to its high ductility [5, 6]. The unique combination of polyimide and silver has great potential for flexible cables in quantum computers, but they must be adapted for cryogenic use. Key factors affecting cable performance are the electrical and thermal conductance of silver. Increasing electrical conductivity tends to raise thermal conductivity as well. Effective cable performance requires good electrical conductivity to prevent signal losses, however, very good thermal conductivity can lead to heat load issues during cooling and operation. Thus, achieving an optimal balance between the electrical and thermal conductivities of silver is essential. This highlights the importance of material science behind the performance of new and advanced material systems in the sense that the material properties should be combined, altered, and improved for innovation and technology. Materials science nicely links the theory and the design of new technologies to real-world engineering developments such as cryogenic flexible cables.

The Residual Resistivity Ratio (RRR) is a critical parameter to estimate the thermal load of the system by using the electrical resistivity of conductor material [7]. It is defined as the ratio of the material's electrical resistance measured at room temperature (~ 300 K) to the one measured at liquid He temperature (4.2 K) [8]. Taking the ratio eliminates all dimensional factors affecting the electrical resistance and, in this way, provides a tool to assess the quality of materials used in electronics and determine their suitability for cryogenic applications. For wire manufacturing for cryogenic applications, materials with low RRR values are preferred. This preference arises from their characteristic higher electrical resistivity at low temperatures and consequently lower thermal conductivity. In this way, materials with low RRR values can provide high electrical conductance at high temperatures ensuring efficient signal transmission while minimizing the thermal load at low temperatures owing to their low thermal conductance.

In the product design of Delft Circuits' Cri/oFlex cables, ground planes, which consist of a thin film of silver evaporated onto the PI are the primary contributors to the heat load. These ground planes serve as the shields on the top and bottom layers of the stack-up configuration of Cri/oFlex cables. They ensure signal integrity by effectively preventing signal interference, noise, and losses. However, their extensive conducting surface area inherently leads to high heat conductance. Therefore, this thesis focuses on the RRR values of the ground planes in the cable design to estimate the heat load while maintaining sufficient electrical conductivity. The parameters that are investigated in this project are oven heat treatment, lamination runs, silver purity, film thickness, and aging and storage conditions because these parameters are involved in the real fabrication procedure of the Cri/oFlex cables. Oven heat treatment is a regular step in Delft Circuits' cable manufacturing procedure that is used to improve the adhesion between the silver and the PI substrate. Lamination is another fabrication step utilized in cable production for layering by applying heat and physical pressure through pistons.

This thesis aims to gain a better understanding of the temperature dependence of the electrical and thermal conductance of silver thin films on the fabrication processes, purity levels, and external factors like aging and storage conditions. First of all, a literature review is conducted, covering the physical phenomena of the electrical and thermal conductivity of metals, and an overview of thin film technology. Based on the review, research questions are formulated to evaluate the microstructural aspects of silver thin films on their electrical and thermal properties. Following that, research methodologies for sample fabrication and cryogenic measurements are given. Results and discussions are then presented followed by the conclusions of the study and future recommendations.

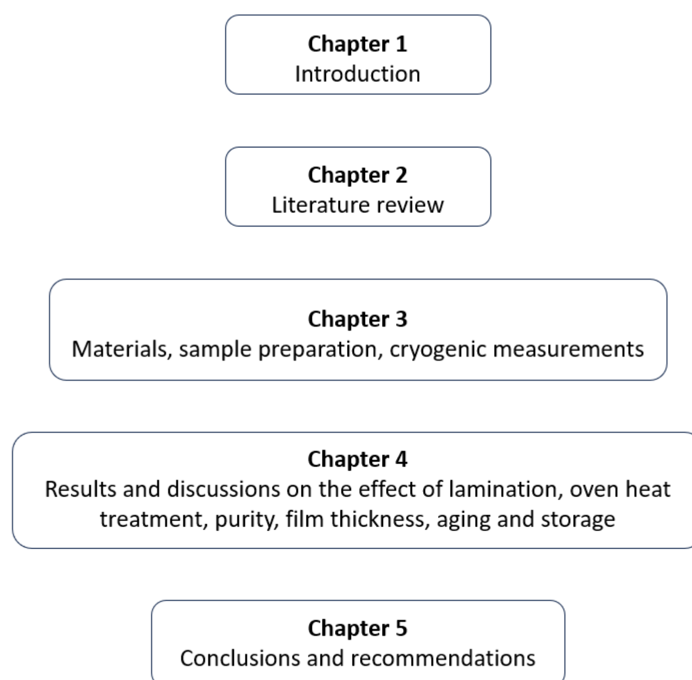

Figure 1.1: Thesis outline

2

Literature Review

2.1. Motivation

Quantum computers have various potential benefits from society's point of view but building a quantum computer is not a straightforward process since it involves many design challenges [1]. Hence, advanced scientific knowledge and systematic research involving measurements and experiments are required to achieve the benefits of this revolutionary technology [1]. Initially, quantum computers need extremely cold temperatures to function, therefore cryogenic dilution refrigerators are usually used to provide such low temperatures down to a few Kelvin. One of the biggest challenges of creating a quantum computer is the need for a scalable hardware system. Figure 2.1 reveals the details of how complex the wiring of a quantum computer looks. Coaxial cables have traditionally been used to carry high-frequency electrical signals with low losses in a wide range of applications such as cable television signals, telephone lines, and radars. However, they can not address the wiring challenge of quantum computers since they occupy massive volumes considering the complex cabling system required by quantum computers. The increase in the space that a quantum computer would take can cause a detrimental reduction in the efficiency of quantum computers since the effective volume that can be cooled is limited. Therefore, a feasible and scalable hardware design needs to be developed for quantum applications to tackle this problem. Flexible cables, where a metal layer is deposited onto a flexible polymer substrate, provide a promising solution with their lightweight, relatively small volume, and scalability [9].

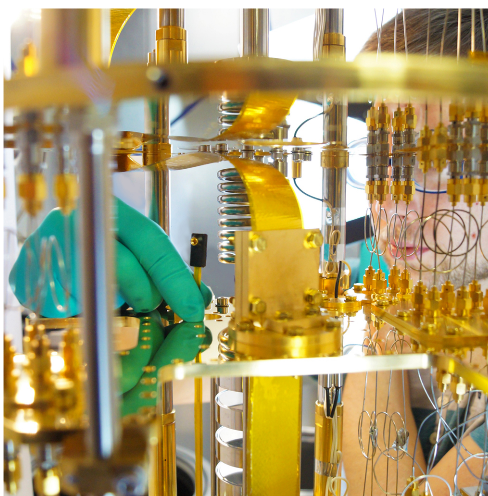

Figure 2.1: The wiring of a quantum computer [10].

2.2. Current state of the Art

In general, a cable should fulfill several requirements to be functional in electronic applications. Firstly, it should contain a good conductor material to carry the current. Secondly, a proper thickness of insulation material is needed for safety at the voltages that the cable is designed for. Lastly, the combination of these two materials should be mechanically and chemically durable, stable, and reliable during the service life of the product. These requirements become even more critical when it comes to quantum applications due to extremely low temperatures. In this case, materials must also be compatible with low temperatures and fulfill their functional requirements. For instance, the conductor material must exhibit sufficient electrical conductivity at low temperatures as well as poor thermal conductivity not to generate a high heat load. Moreover, the insulator material should remain physically and chemically compatible with conductor material once they go down to cryogenic temperatures.

Metalized polymer films have attracted great attention in the rapid development of flexible electronics [11]. In particular, Polyimide (PI) films have been widely known and used due to their outstanding combination of mechanical, thermal, and electrical properties. Especially, its low dielectric constant, low thermal expansion coefficient, high bulk resistance, good flexibility, and high ductility make PI a good candidate for quantum hardware technologies, cryogenic applications, and fabrication of flexible electronics [4]. On the other hand, Silver (Ag) is a good electrical conductor and this characteristic makes it an ideal choice to be used as the conductor in cables [5]. Furthermore, its ductility allows it to be deposited on a PI substrate for flexible electronics applications [6].

2.3. Challenges

The unique combination of polyimide and silver creates a promising solution for a high-performance flexible cable that is relatively light, thin, and scalable for the massive wiring system required by quantum computers. However, it still needs to be engineered to be suitable for cryogenic quantum applications. The most relevant material properties at low temperatures that affect the performance of the cable are electrical and thermal conductance, which are highly dependent on the temperature for the conductive material. For good cable performance, the conductor material should have good electrical conductivity to reduce losses. On the other hand, thermal conductivity should not be very high, because it can increase the heat conductance during cool-down and cause heat load in the wiring system. There is a well-known linear relationship, which is also called the Wiedemann-Franz-Lorenz law, between the electrical and thermal conductivity of metals [12]. Once the electrical conductivity is increased in several possible ways such as purity or microstructure, the thermal conductivity of the material also tends to increase [13]. Therefore, there is a trade-off for obtaining an optimal combination of the electrical and thermal conductivities such that the electrical conductance of the wiring system would be good enough without causing an excessive thermal load.

2.4. Temperature dependence of electrical and thermal properties

The increasing developments of modern technologies have led to an increased need for sophisticated new materials and in-depth knowledge of their properties. In particular, low-temperature applications have recently taken great attention from researchers and industry due to their crucial role in building quantum computers. In order to accelerate the developments in quantum applications, a flexible cabling design is required. Due to the need for cryogenic temperatures in quantum applications, the low-temperature properties of materials used in the Cri/oFlex cable design should be investigated thoroughly. In this way, the performance of flexible cables can be improved and a scalable i/o for cryogenic applications can be achieved. Therefore, this chapter of the literature study aims to provide an understanding of the physics behind the temperature-dependent behaviors of materials.

For this project, the most relevant material properties for cryogenic applications are the electrical and thermal properties of the conductor material used in the cabling design of quantum computers. Therefore, this section of the literature study mainly focuses on metals' electrical and thermal conductance properties.

2.4.1. Electrical properties

The low-temperature electrical resistivity reveals useful information about the impurities and the stress state present in the material. Resistivity measurements can provide insights into the materials regarding the electronic structure as well as into other aspects of the fundamental physics of metals including thermal properties. Knowing the electrical resistivity allows us to calculate and predict the thermal conductivity, which is not straightforward to measure directly at cryogenic temperatures [14]. Electrical resistivity measurements are relatively more convenient and accurate to perform and require less complex measurement setups.

This section explores the physics of charge conduction to understand the temperature-dependent behavior of electrical resistivity. In metals, electrical charge is transported by energetic electrons, which are called "free" electrons in the elementary kinetic theory of transport in metals [15]. This model is known as "the Drude Model" and it defines the electrical conductivity σ_e as:

$$\sigma_e \equiv \frac{1}{\rho} = \frac{Ne^2 l}{m\overline{v}} \tag{2.1}$$

where ρ is the electrical resistivity, N is the number of conduction electrons per unit volume, e is the charge of an electron, l is the average distance (mean free path) between the collisions of electrons, m is the electron mass and $\overline{v}$ is the average velocity of conduction electrons [15].

As can be seen in Equation 2.1, the electrical conductivity is dependent on the average velocity $\overline{v}$, the mean free path l and several constants namely N, e and m. If we disregard the constants, the electrical conductivity is mainly determined by the average velocity $\overline{v}$ and the mean free path l. Free electrons in a solid travel with a very high velocity [16]. Therefore, it is unlikely that it will be influenced by the thermal energy remarkably [14]. This makes the mean free path l the primary component that determines the temperature dependence of electrical conductivity [14]. There are two different mechanisms that dominate the mean free path l separately [14]. The first mechanism that influences the l is the thermal vibrations (phonons) of the crystal lattice which are the dominant factor at high temperatures. Hence, l is highly temperature dependent at high temperatures. This mechanism controls the ideal resistivity of a metal $\rho_i(T)$. Secondly, at low temperatures, l is determined by the crystal lattice imperfections such as impurities, vacancies, and interstitials. Therefore, it mainly reveals the purity level of the material. It determines the residual resistivity ρ_{res} and is independent of temperature.

2.4.1.1. Residual resistivity ρ_{res}

Residual resistivity ρ_{res} is the dominant resistivity component of metals at low temperatures. It is mainly caused by impurities present in the material. In order to obtain good conducting metals at low temperatures, sample purity becomes the most significant factor determining electrical resistivity [14]. Figure 2.2a indicates how the electrical resistivity of aluminum changes with respect to the impurity level present in the material. As can be seen, the electrical resistivity increases with the increasing impurity level at low temperatures. On the other hand, the electrical resistivities of samples with different purity levels become the same at high temperatures. The reason for such an electrical resistivity curve is the fact that the dominant mechanism determining the electrical properties is the chemical composition at low temperatures. However, once the temperature increases to room temperature, the lattice vibrations mechanism takes over. Since all of the samples are aluminum in this case, they have the same crystal lattice which results in the same electrical resistivity value.

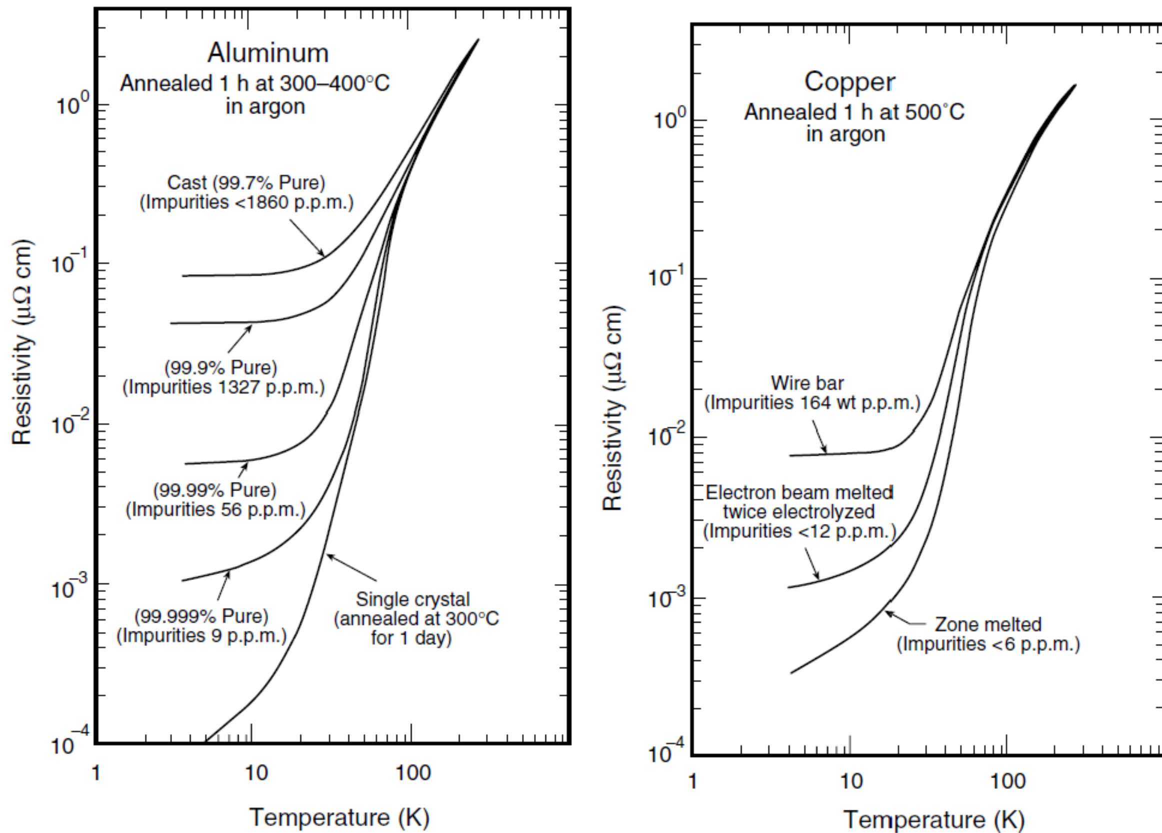

(a) Electrical resistivity of aluminum as a function of impurity content [14].

(b) Electrical resistivity of copper as a function of impurity content and several cold working activities [14].

Figure 2.2: Electrical resistivities for different grades of annealed aluminum and copper

Another factor that has an impact on the residual resistivity ρ_{res} of conducting materials is the atomic lattice defects caused by cold work and heat treatments [14]. These defects are crystalline vacancies or dislocations. Figure 2.2b demonstrates the effect of different processing techniques on the electrical resistivity of copper. As shown in Figure 2.2b, each processing method results in different electrical resistivity values at low temperatures. Although all samples belong to the same parent material, the way that they are fabricated introduces various types of atomic defects in their crystal structure as well as different impurity concentrations. This leads to a variation in their electrical properties at low temperatures. Once the temperature increases, different electrical resistivity values of the samples converge to the same value, which results from the unique phonon scattering mechanism occurring in copper material at high temperatures.

As one can see, there are many elements that influence the residual resistivity ρ_{res} of metals varying from the type and amount of impurities to processing techniques. Furthermore, they are not entirely distinct mechanisms affecting electrical properties. For instance, the type and the number of impurities can also potentially introduce new defects or alter the type and density of defects present in the material [13]. Therefore, considering the complex and interconnected structure of the microstructure of materials, the most convenient way to obtain the residual resistivity of materials is to perform measurements [14]. The easiest way to perform resistivity measurements at low temperatures is to immerse the sample in liquid Helium since the electrical resistivity values reach a plateau around the liquid He temperature (4.2 K) as shown in Figure 2.2.

2.4.1.2. Ideal resistivity $\rho_i(T)$

Ideal resistivity $\rho_i(T)$ is a unique property of each metal's crystal structure and it results from the thermal vibrations (phonons) at high temperatures [13]. Contrary to highly defect-dependent residual resistivity ρ_{res}, ideal resistivity does not primarily depend on the chemical impurities in the material or how the material has been processed. Figure 2.2 shows electrical resistivity values of aluminum and copper for a given temperature range. While electrical resistivity is highly dependent on the impurity level and processing methods at low-temperature regions, electrical resistivity values converge with increasing temperatures. This shows that the dominant factor affecting the electrical resistivity of metals at high temperatures is lattice vibrations, which is a unique crystal configuration property and does not depend on the impurity level. As shown in Figure 2.2, electrical resistivities have a tendency to increase with rising temperature [17]. This can be explained by the enhanced thermal vibration activity which, in turn, leads to increased difficulty in electron movement.

2.4.1.3. Matthiessen's rule

Matthiessen's Rule presents a simple method to estimate the total electrical resistivity of metals [18]. According to Matthiessen's Rule, the total electrical resistivity of metals is the sum of the resistivities from defect scattering ρ_{res} and phonons $\rho_i(T)$ [18]:

$$\rho(T) \cong \rho_{res} + \rho_i(T) \tag{2.2}$$

In practice, there might be differences between the resistivities measured and calculated by using this rule. However, Matthiessen's rule provides a reasonable and useful approximation for the estimation of total resistivity of nearly pure metals [14].

2.4.1.4. Residual Resistance Ratio (RRR)

For the hardware of quantum applications, the challenge is to predict the material properties of the electronic parts when they go to cryogenic temperatures. At low temperatures, the trade-off between good electrical conductance and relatively poorer thermal conductance becomes more critical as it greatly affects the performance of the system due to the heat load. The RRR is an index to estimate the heat load of the system and is defined by the ratio of the electrical resistivity at room temperature $\rho_{(290K)}$ and the one at liquid Helium temperature $\rho_{(4.2K)}$, as shown below:

$$RRR = \frac{R_{(290K)}}{R_{(4.2K)}} = \frac{\rho_{(290K)}}{\rho_{(4.2K)}} \tag{2.3}$$

It provides a tool to evaluate the relationship between the electrical and thermal conductances by linking the electrical resistivities at room temperature and at low temperatures, which is usually liquid Helium temperature (4.2 K) [7].

In order to lower the thermal load in cryogenic applications, thermal resistivity should be increased. One way to achieve this is to increase the electrical resistivity as they are linearly dependent [12]. Therefore, a low RRR value is an indication of high resistivity at 4.2K, and as a result, it can be also correlated with the lower heat load.

RRR provides a useful parameter to extract the material purity since the numerator mainly depends on the thermal vibrations and the denominator depends essentially on the impurities [13]. Thus, the ratio becomes sensitive to the purity level. In Figure 2.3, total electrical resistivities of four silver specimens are presented. Considering the similar trend of the curves of Figure 2.3 compared to Figure 2.2a and Figure 2.2b, different RRR values represent different chemical impurity or crystal defect levels of specimens resulting in different electrical resistivity values at low temperatures. Since high temperature electrical resistivities do not depend on the crytal imperfections, RRR provides a sensitive measure of purity. Furthermore, RRR is independent of the sample shape or dimensions, therefore it is convenient to calculate it through electrical resistance as well as through electrical resistivity.

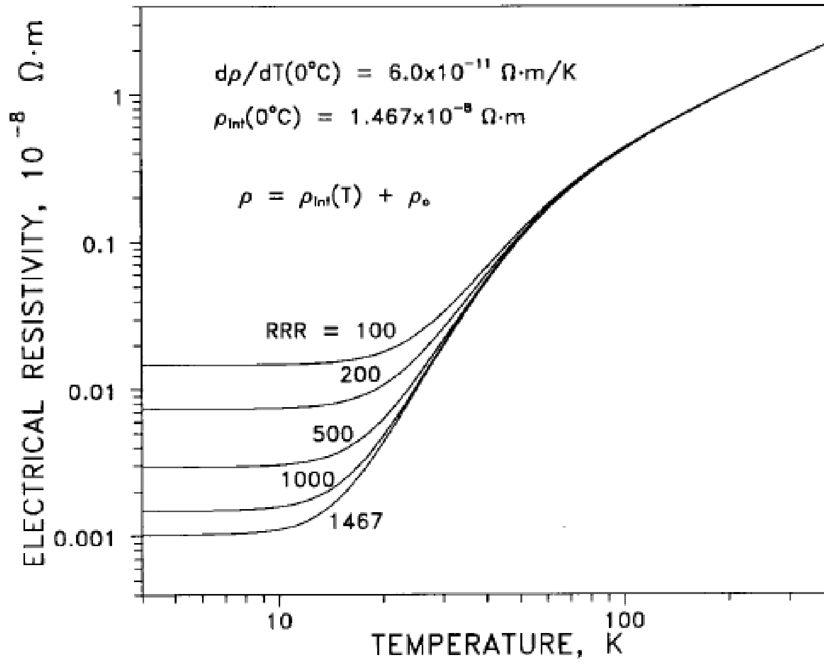

Figure 2.3: Electrical resistivity curves of four different silver specimens with various RRR values as a function of T, where ρ_{int} is ideal (intrinsic) resistivity, ρ_{res} is residual resistivity and RRR is given as $\rho(273K)/\rho(4.2K)$ [8].

2.4.2. Thermal properties

As mentioned before, quantum computers need cryogenic temperatures to function [3]. Therefore, heat transport is one of the key performance parameters for the i/o of quantum computers in order to build an efficient device with a limited thermal budget. When obtaining low-temperature heat transfer data for materials to predict their behavior, one should focus on the material characterization. The thermal conductivity of the materials is the principal material property for thermal transport analysis and calculation of thermal load in the system. This section focuses on the thermal properties of solids and the main emphasis is given to the thermal conductivity behavior of pure metals.

Heat transport in solids occurs by two kinds of carriers: electrons and lattice vibrations (phonons) as shown below:

$$\lambda = \lambda_e + \lambda_p \tag{2.4}$$

where the summation of electron heat conduction λ_e and phonon heat conduction λ_p is the total thermal conductivity λ [14]. At high temperatures, phonons are the main mechanism that contributes to heat transport [19]. On the other hand, phonon contribution to thermal conductivity is very limited at low temperatures due to smaller thermal energy, and electrons become the dominant heat carriers [14].

The kinetic theory provides a method to estimate the thermal conductivity:

$$\lambda_i = (1/3)C_i v_i l_i \tag{2.5}$$

where C_i is volumetric heat capacity, v_i is the velocity and l_i is the mean free path of the carrier, which is either the electrons or the phonons [15]. From Equation 2.5, it can be claimed that the electron scattering mechanism plays an important role in the thermal conductivity of metals due to the presence of l in the equation. Hence, it does not only limit electrical conductivity as we saw from Equation 2.1, but it also limits thermal conductivity. Thus, there can be found a relation between electrical and thermal

conductivities. As explained before, the electron velocity at Fermi level v_e is quite high so it is unlikely to be influenced by temperature changes [14]. The electronic contribution to volumetric heat capacity C_e varies as T:

$$C_e = cT \tag{2.6}$$

where c is the proportionality factor. Furthermore, the mean free path l is proportional to T^{-1}, which makes the thermal conductivity independent of temperature when multiplied by C_e in Equation 2.6 [14]. As a result, the thermal conductivity of nearly pure metals is not affected by the temperature at high temperatures [14]. On the other hand, at low temperatures l_e is determined by defect scattering and it does not depend on T [14]. In this way, C_e term in the Equation 2.5 becomes the only factor determining the thermal conductivity. Accordingly, the thermal conductivity changes linearly by T in nearly pure metals at low temperatures [14].

Figure 2.4 demonstrates the constant thermal conductivity of nearly pure metals at high temperatures and their linearly temperature-dependent thermal conductivity at low temperatures. It should be noted the axis of the graph is presented logarithmically and the y-axis spans about five orders of magnitude. Figure 2.5 illustrates a smoothed version of thermal conductivity curves for pure copper specimens. While the thermal conductivity of the samples tends to remain within a few percent range at room temperature (~ 300 K), at low temperatures (~ 10 K) the heat transport properties of these copper specimens vary over three orders of magnitude. Therefore, more efforts are needed to characterize thoroughly the thermal properties of nearly pure metals at low temperatures. In order to identify the transport properties of metals, one should not only consider the temperature dependence of thermal conductivity but also the chemical and physical state of the metal in terms of chemical composition, impurity level, processing defects, heat treatments, and environmental conditions such as storage.

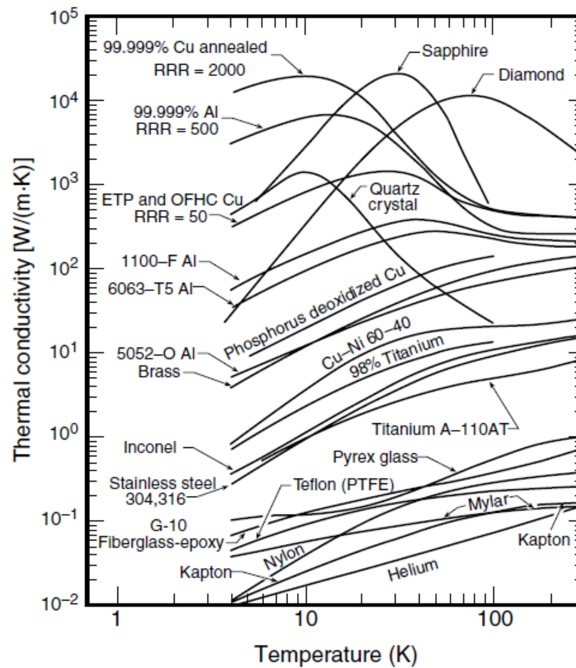

Figure 2.4: Typical thermal conductivities of various materials as a function of T [14].

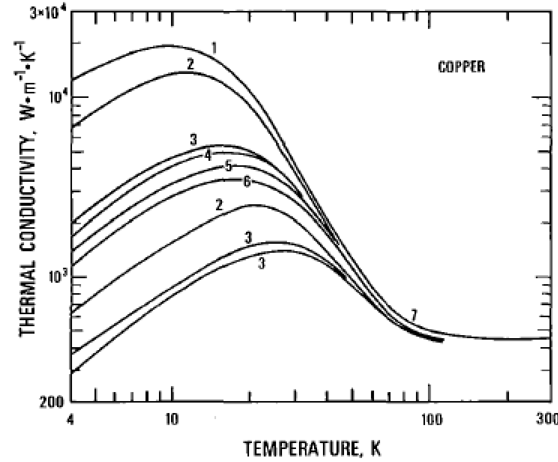

Figure 2.5: Experimentally measured thermal conductivities of various copper samples containing less than 0.1 % impurity (-White and Talnsh (1960); 2 - Powell, Roder, and Hall (1959),3- White (1953); 4 - Berman and McDonald (1952); 5 - Hust and Giarratano (1974); 6Mendelssohn and Rosenberg (1952); 7 Moore, McElroy, and Graves (1967).) [13].

As discussed for the electrical properties before, the phonon contribution of the thermal resistivity is also a generic characteristic of the material since it results from unique lattice vibrations of each element [13]. The phonon contribution to thermal conductivity can vary significantly between low temperatures and high temperatures [20]. At low temperatures, there are only a few phonons excited, therefore, the probability of phonon-phonon scattering is very low [21]. Instead, phonon scattering against the crystallographic defects is the dominant mechanism at low temperatures [21]. On the other hand, at high temperatures, a greater number of phonons are thermally excited. Hence, phonon-phonon scattering becomes significant [20]. If the momentum of colliding phonons is large enough, the resulting phonon can reverse its direction [21]. This process is called the Umklapp process (U-process) and results in an increase in the thermal resistance of the material [21]. The effect of this scattering mechanism on the thermal conductivity behavior of copper can be seen in Figure 2.5. After a certain temperature thermal conductivity starts decreasing. Contrary to phonon contribution, the electronic contribution of the thermal resistance is determined by the impurities and lattice defects and becomes dominant at low temperatures [13]. This theory justifies the large spread of the curves in Figure 2.5 at the low-temperature range. This is the reason that it is not adequate to assign a thermal conductivity value for metal at low temperatures. It is highly influenced by the density and the type of defect mechanism present in the material [14]. The effect of material imperfections should be analyzed and characterized in such a way that the thermal conductivity of materials can be specified. The next section presents a convenient and practical method to obtain thermal conductivity characterization.

2.4.2.1. Wiedemann–Franz–Lorenz law

Wiedemann-Franz-Lorenz law provides a useful relation for estimating the thermal conductivity of metals. According to the law, the electrical and thermal conductivities of metals have a constant ratio at room temperature which is proportional to temperature [13]. It relies on comparing the kinetic theory equations for both electrical and thermal conductivities, Equation 2.1 and Equation 2.5 respectively. It assumes that the value of the mean free path l_e would be similar for both cases, therefore, l_e can be eliminated by taking the ratio:

$$\frac{\lambda_e}{\sigma_e} = \frac{(1/3)C_e v_e l_e}{\frac{Ne^2 l_e}{m v_e}} = \frac{(1/3)C_e v_e^2 m_e}{Ne^2} \tag{2.7}$$

In order to investigate the temperature dependence of λ_e further, one more modification to Equation 2.7 is required. As described before in Equation 2.6, C_e is linearly temperature dependent. Therefore, considering v_e is not influenced by the temperature and every other component in Equation 2.7 is a constant, the temperature dependence of λ_e is determined by C_e. The quantum theory for the electronic specific heat is given by [22]:

$$C_e = \frac{\pi^2}{2}\frac{k_B^2 T}{E_F} \tag{2.8}$$

where k_B is Boltzmann constant, which equals to 1.380649 × 10-23 $m^2 kg s^{-2} K^{-1}$ and E_F is the energy of electrons close to the Fermi level. E_F can be expressed by [22]:

$$E_F = \frac{1}{2} m v_e^2 \tag{2.9}$$

By combining the C_e from Equation 2.8 and the electron theory of gases [23], Wiedemann-Franz-Lorenz can be obtained:

$$\frac{\lambda_e}{\sigma_e T} = \frac{\pi^2}{3}(k_B/e)^2 \equiv L_N = 2.44x10^{-8} V^2/K^2 \tag{2.10}$$

where L_N is the Lorenz number [14]. This law is in quite good agreement with the experimental data at high temperatures, where the electron scattering by the phonons mechanism is the primary factor, as well as at low temperatures, where electron scattering by atomic defects dominates [14].

The Wiedemann-Franz-Lorenz law plays an important role in obtaining the thermal conductivity of nearly pure metals since electrical resistivity measurements are considerably easier to perform than thermal conductivity measurements in practice. This makes the relation Equation 2.10 highly valuable and convenient for thermal analysis and heat transfer calculations. The next section aims to give a grasp on how thermal load calculations can be done to evaluate the performance of conductor materials in terms of efficiency.

2.4.2.2. Heat load

The heat flow through a solid material can be expressed as:

$$\dot{Q} = -\lambda(T) A \frac{dT}{dx} \tag{2.11}$$

where $\dot{Q}$ is the rate of heat flow through an area A with a temperature gradient dT/dx and λ is the thermal conductivity [12]. This relation is known as the Fourier-Biot equation [13]. The minus sign shows that the heat flow occurs in the opposite direction to the temperature gradient.

In a steady state, the temperature profile is time-independent as in dT(x)/dt = 0 so Equation 2.11 becomes [12]:

$$\dot{Q} = \lambda(T) A \frac{dT}{dx} = 0 \tag{2.12}$$

For the simplest case in which the thermal conductivity λ is temperature independent, Equation 2.12 reduces to a simple equation by several mathematical operations. Lastly, the following relation can be obtained by integrating Equation 2.12 over the entire length of the system [12].

$$\dot{Q} = \frac{\lambda A \Delta T}{L} \tag{2.13}$$

For the more realistic case in which the thermal conductivity λ is temperature-dependent, the heat flow in the system can be expressed as:

$$\dot{Q} = \frac{A}{L}\int_{T_1}^{T_2} \lambda(T)\, dT \tag{2.14}$$

As mentioned before, thermal measurements require high accuracy and a massive effort to perform so they are not convenient. Therefore, the heat flow calculations that are presented in this section have the potential to provide a useful way of evaluating the efficiency of the quantum computers' wiring system.

2.5. Metallic thin films

2.5.1. Thin film technology

Thin film technology involves the deposition process to create a layer on different substrate materials by utilizing a variety of techniques and tools [24]. It has been widely used in many industries namely electronic, thermal, and optics due to their excellent technological advantages in creating modern functional material properties. The technology of thin films includes a wide range of thicknesses from fractions of a nanometer to a few microns [24].

Thin films show distinctly different properties than bulk materials due to their high surface-to-volume ratio [24]. The main difference between thin films and bulk materials is that thin films have different electronic configurations due to missing neighbor atoms on one side. This asymmetry results in different energy states at the surface. Therefore, the forces acting upon the surface are different than the bulk [25]. As a result, they display different material properties. The asymmetric stress state makes thin films very dependent on the deposition conditions in terms of the microstructural features such as grain size, texture, grain boundaries, dislocations, and impurities [26]. Hence, thin film deposition allows the precise modification of the material properties to achieve a specific performance by tuning the deposition parameters [26].

2.5.2. Thin film deposition techniques

The deposition technique is considered a key parameter to obtain desired material properties since it can determine the properties of thin films in terms of microstructure, surface morphology, electrical, thermal, and optical [27]. In order to explore the unique design opportunities that thin films offer, different deposition methods should be studied. This section reviews different thin film deposition techniques that can be performed especially for the fabrication of flexible cabling design.

Vapor deposition is one of the main subgroups of thin film deposition techniques [26]. It consists of two prominent subsets which are physical vapor deposition (PVD) and chemical vapor deposition (CVD) [27]. The distinguishing characteristic between those deposition techniques is that the vapor in PVD is formed by atoms while CVD involves a chemical reaction of the vapor on the substrate that leads to the formation of the thin film [27]. As can be predicted, CVD requires more advanced control over the deposition parameters such as flow rate, pressure, temperature, and the concentration of chemical species in order to form specific products [27]. In this literature study, we only focus on the PVD techniques since they can provide sufficiently precise control over the resulting material properties in terms of microstructure and film thickness.

There are several available physical vapor deposition (PVD) techniques to deposit a metallic layer onto a substrate. Evaporation and sputtering are the most commonly used PVD methods. Evaporation can be performed in two ways: one of them is thermal evaporation and the other one is electron-beam evaporation. These methods deposit the metallic layer by evaporating the metal from a crucible by means of heat or e-beam. Figure 2.6a presents a schematic representation of the chamber of an evaporation system [28]. The crucible and the target material are placed into the vacuum chamber. The vapor flux is generated from the target metal. The vapor flux reaches the substrate material and condenses on it. Evaporation occurs in a high vacuum to provide a path for the molecules such that they travel toward the substrate. Therefore, having a contaminant-free environment in the chamber is crucial to prevent collisions and inefficient deposition process [29].

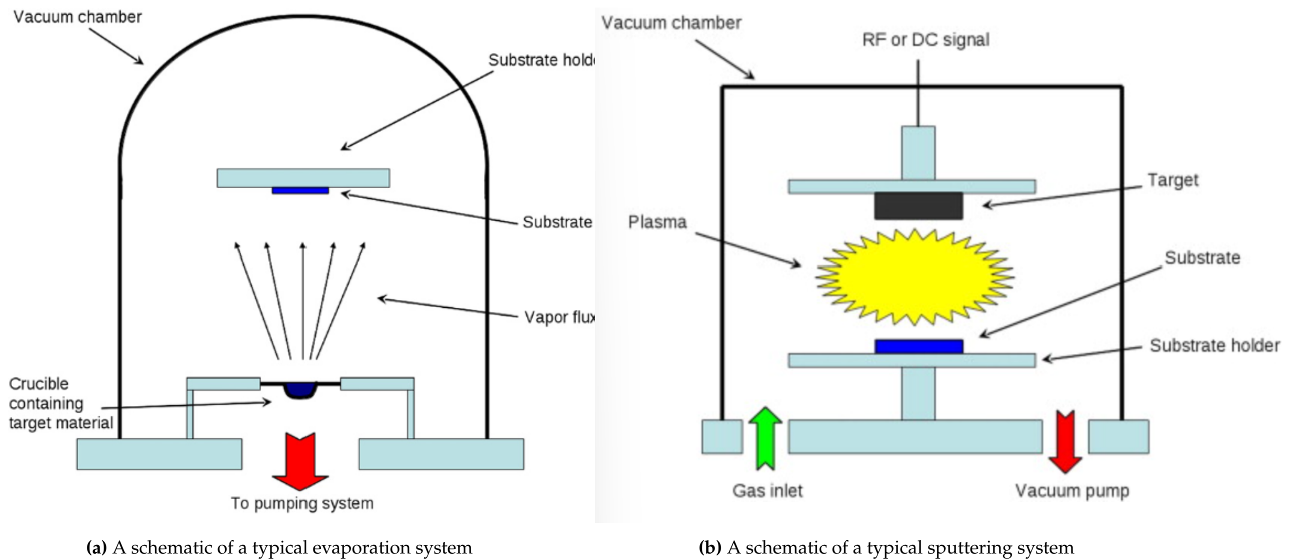

(a) A schematic of a typical evaporation system

(b) A schematic of a typical sputtering system

Figure 2.6: the Schematic representations of different physical vapor deposition methods [28]

The main difference between evaporation and sputtering techniques is how the vapor flux is formed. In contrast to evaporation, sputtering is a deposition technique that is based on the bombardment of a target with energetic ions [30]. In this way, target atoms are removed by the momentum transfer from the bombarding energetic ions. The sputtered atoms create a vapor flux and these atoms condense on the substrate material as a thin film [31]. Figure 2.6b depicts a schematic for the sputtering process [28]. As seen in Figure 2.6b, the plasma medium is involved in the sputtering process. It is created by the secondary electrons emitted from the target surface [32]. The low efficiency of the ionization process in the plasma and the requirement for a cooling system due to the heating of the substrate limit the deposition rate during sputtering. The deposition rate during sputtering is typically 3-15 $Ås^{-}1$ [33]. On the other hand, evaporation techniques can achieve deposition rates as high as 50 $\mu ms^{-}1$ when a high-power electron beam source is used [34, 28].

2.5.3. Microstructural aspects of metallic thin film deposition

Most often, thin film properties are affected by the used deposition technique, film thickness, and deposition parameters [27]. By tuning the deposition parameters, one can obtain different microstructural features in terms of crystallinity level, defect density, stress level, adhesion quality, surface roughness, contamination level, dislocation density, grain size, and composition [24]. In order to discover these selective modifications, this section aims to discuss the microstructural aspects of metallic thin film deposition specifically by evaporation and sputtering.

2.5.3.1. Deposition parameters affecting the microstructure of thin films

There are several deposition parameters to control the resulting microstructure of thin film deposited by evaporation and sputtering. The most important process control parameters are gas pressure, substrate temperature, energy, flux, and the angle of incidence of the depositing particles [24]. The investigation of each parameter on the microstructure and the growth mechanism of thin films would require an excessive amount of effort in terms of experiments, measurements, and characterization. Therefore, during the development of thin film technologies, several models have been developed by scientists and researchers in order to represent the relation between the microstructure of metallic thin films to the deposition conditions [35]. These models are called structure zone models (SZM). In order to make those models as universal as possible, substrate temperature and chamber gas pressure have been chosen as the most important deposition parameters to asses the resulting film structure.

The earliest structure zone model was proposed by Movchan and Demchishin in 1969 for the evaporated metal films with thicknesses ranging from 0.3 to 2 mm at deposition rates changing between 12000 and 18000 Å/min [36]. In this model, film structure was identified with 3 zones (1, 2, and 3) [36]. These zones are formed based on the relationship between the film structure and the ratio of the substrate temperature T to the melting temperature of target material T_m [37]. Later, a similar SZM was introduced by Thornton in 1975, at which the film structure consists of 4 distinct zones (1, 2, T and 3) as shown in Figure 2.7.

- Zone 1 is formed when the adatom energies are not sufficient for surface diffusion. Therefore, the grains remain small in size and they are far apart from each other causing porous morphology and columnar structure as depicted in Figure 2.7 [25].

- In zone 2, higher substrate temperature results in a more uniform surface, and a denser columnar crystalline structure can be observed with the help of larger grain size and a higher degree of binding between the columns [27].

- Zone 3 takes place when the substrate temperature goes even higher which leads to volumetric diffusion processes such as annealing and recrystallization [25]. In this way, an improved crystalline structure can be obtained by the grain growth [27].

- Zone T represents the influence of the gas pressure during the deposition [37]. Figure 2.7 shows that the increasing gas pressure adversely influences the microstructural evolution of thin films by affecting the mean free path of particles [27]. This can result in lower mobility of the adsorbed atoms and a delay in the formation of columnar structure [25]. Zone T consists of densely packed fibrous grains [37].

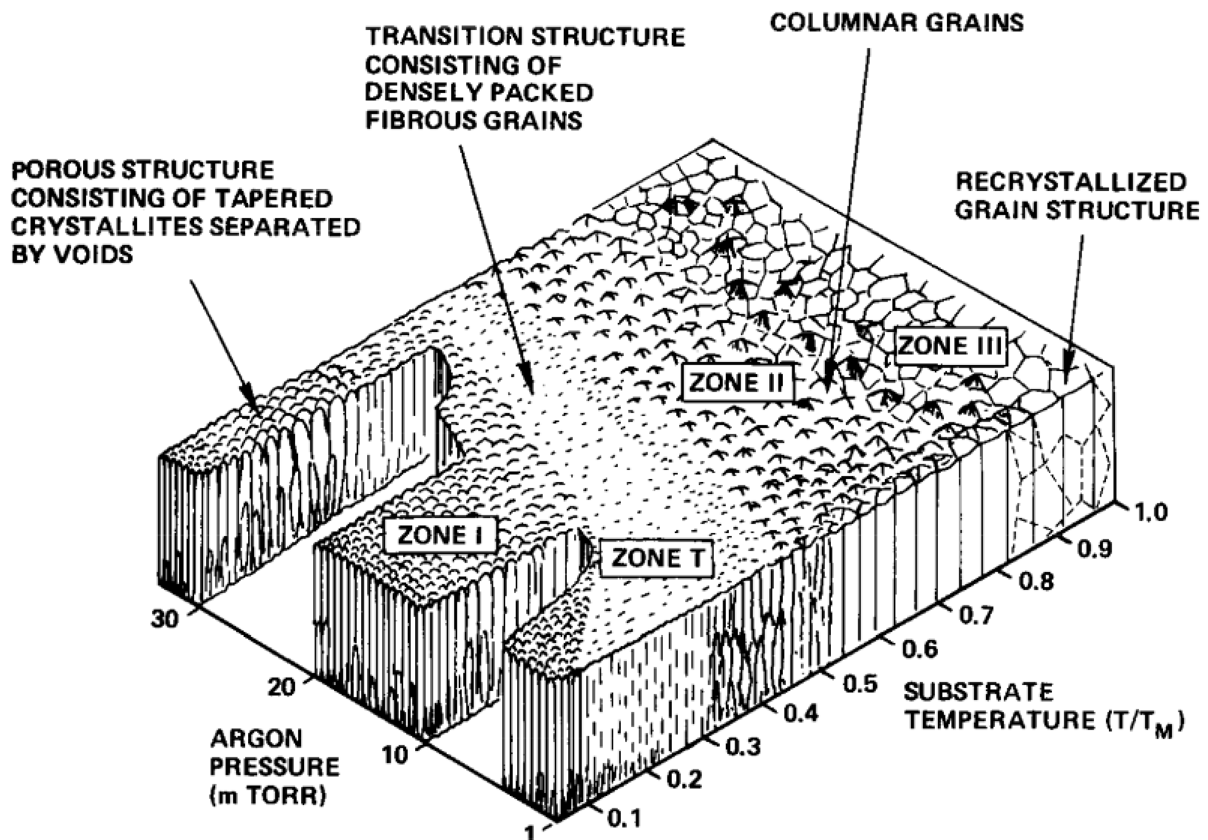

Figure 2.7: Structure zone model diagram [37].

Table 2.1 summarizes the zone structures and properties of evaporated and sputtered metal films. Additional to SZMs, it also shows the resulting film properties. Figure 2.7 and Table 2.1 illustrate how the experimental deposition conditions affect the film structure and result in different material properties. By utilizing these dynamic structure zone models, one can tune the deposition parameters to obtain a specific microstructure for desired material properties. In this way, tailored engineering materials can be designed and fabricated for specific applications.

Table 2.1: The comparison of the zone structures of evaporated and sputtered films [25]

Zone	T/T_M	Structural Characteristic	Film Properties
1 (E)	< 0.3	Tapered crystals, dome tops, voided boundaries	High dislocation density, hard
1 (S)	< 0.1 at 0.15 Pa to < 0.5 at 4 Pa	Voided boundaries, fibrous grains. Zone 1 is promoted by substrate roughness and oblique deposition	Hard
T(S)	0.1 to 0.4 at 0.15 Pa, ~ 0.4 to 0.5 at 4 Pa	Fibrous grains, dense grain boundary arrays	High dislocation density, hard, high strength, low ductility
2 (E)	0.3 to 0.5	Columnar grains, dense grain boundaries	Hard, low ductility
2 (S)	0.4 to 0.7	Columnar grains, dense grain boundaries	Hard, low ductility
3(E)	0.5 - 1.0	Large equiaxed grains, bright surface	Low dislocation density, soft recrystallized grains
3(S)	0.6-1.0	Large equiaxed grains, bright surface	Low dislocation density, soft recrystallized grains

2.6. Factors affecting low-temperature material properties

This chapter presents the factors affecting the electrical and thermal properties of thin films, namely heat treatment, purity level, film thickness, and, aging and storage conditions. These parameters can potentially alter the microstructure of the materials by means of atomic defects as well as by impurities, and internal stress. Consequently, material properties are changed. The emphasis is directed toward the electrical and thermal properties of metallic thin films, particularly copper and silver. The inclusion of copper alongside silver stems from their closely aligned material properties due to their similar electronic configurations [38]. Moreover, the research done on the silver thin films was limited. Therefore, the scope of the literature study has been extended to copper as well as the silver-containing multilayer systems.

2.6.1. Heat treatment

Heat Treatment is a widely used technique to control the microstructure of metals to obtain tailored engineering materials exhibiting desired properties. It can potentially purify the materials by degassing and reducing the lattice defect density present in the samples [39]. This would increase the RRR value by increasing the purity level.

Figure 2.8 demonstrates a comparison of microscopy images of samples consisting of three layers which are 20 μm coated copper layer, intermediate Ni Flash, and stainless steel base material. The copper layer is highlighted with a red arrow in Figure 2.8a and Figure 2.8b. As can be seen in Figure 2.8a, copper material exhibits porous microstructure before the heat treatment. On the other hand, a denser grain structure can be observed in the annealed sample shown in Figure 2.8b. There are two possible

mechanisms altering the microstructure of the copper as a result of a heat treatment process: outgassing the material and grain growth due to recrystallization [39].

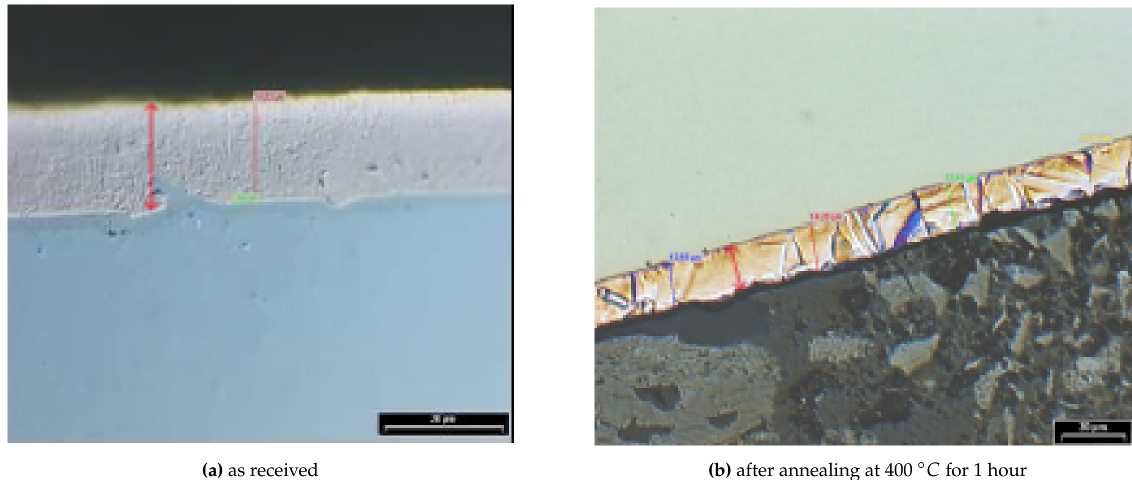

(a) as received

(b) after annealing at 400 °C for 1 hour

Figure 2.8: Microstructural images of copper coated stainless steel samples (a) as received and (b) after annealing at 400 °C for 1 hour [39]

As a consequence of microstructural transformations occurring in the materials, it is expected that the RRR values would also change due to the change in electrical resistivity at low temperatures $\rho_{(4.2K)}$. Fouaidy et al. [40] reported an RRR value of 20 for a 30μm thick copper coating without any heat treatment, while the RRR value of the sample is increased to 113 as a result of vacuum annealing at 400 °C for 1 hour. Hence, the heat treatment process improved the RRR of the sample by a factor of ~ 6 [40].

2.6.1.1. Heat treatment parameters

In order to optimize the properties of materials for good performance in a specific application, the influence of heat treatment parameters should be also investigated. These parameters include annealing temperature, annealing duration, and the ambiance in which the heat treatment is performed.

Annealing temperature

The annealing temperature is one of the most influential factors determining the effect of thermal treatment on the electrical properties of materials. Different annealing temperatures can result in different RRR values. Singer et al. [39] observed that RRR values of copper samples are prominently improved by annealing at temperatures of 350-400 °C while annealing at 820 °C reduced the RRR. However, they did not provide a microstructural analysis for those copper samples to give the reasoning behind such an RRR behavior.

Figure 2.9 presents how the electrical resistance of the ZnO/Ag/ZnO multilayer coating consisting of 0.64 cm thick Ag film with 99.999% purity changes depending on the heat treatment temperature. The annealing process is performed under different conditions, but the effect of annealing ambiance is discussed in one of the following sections of this report. In Figure 2.9 we observe a decrease in the sheet resistance with an increasing temperature up to 300 °C, however, the resistance is radically increasing after 400 °C.

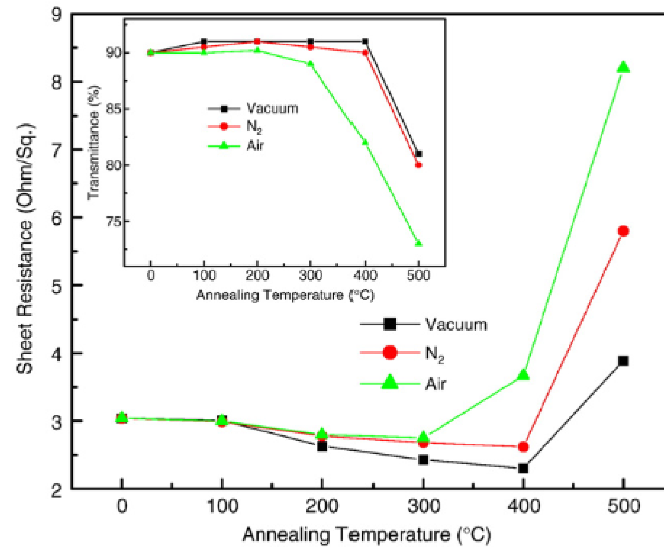

Figure 2.9: Dependence of Ag sheet resistance on the annealing temperature for different annealing ambiances [41].

A similar trend for the resistance with changing temperature is also observed by Jung et al. [42] and Kloppel et al. [43], although they studied a thinner Ag film with a thickness of 30 nm. In order to investigate the resistance behavior, Sahu et al. [41] performed X-Ray diffraction analysis for the multilayer coatings annealed at different temperatures, as shown in Figure 2.10. It can be seen that the thermal treatment led to higher intensities of Ag (111) peaks until 300 °C [41]. The same increasing trend of Ag (111) peak intensities with thermal treatment was also obtained by Jung et al. [42]. In addition to XRD analysis, Jung et al. [42] also performed a grain size analysis as demonstrated in Figure 2.11. Their grain size calculation reveals that the grain size of Ag film is positively influenced by the heat treatment, particularly until 300 °C. Similarly, Dannenberg et al. [44] also investigated the effect of annealing on the grain coarsening mechanism of 80 nm thick Ag films and reported that thermal treatment favors grain growth by providing the required activation energy for grain boundary mobility.

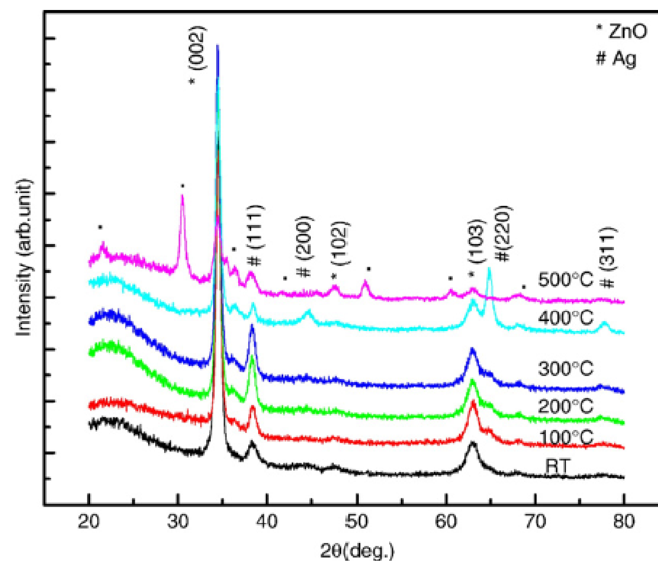

Figure 2.10: X-Ray diffraction patterns of the ZnO/Ag/ZnO multilayer material system at room temperature (before annealing) and at various annealing temperatures [41].

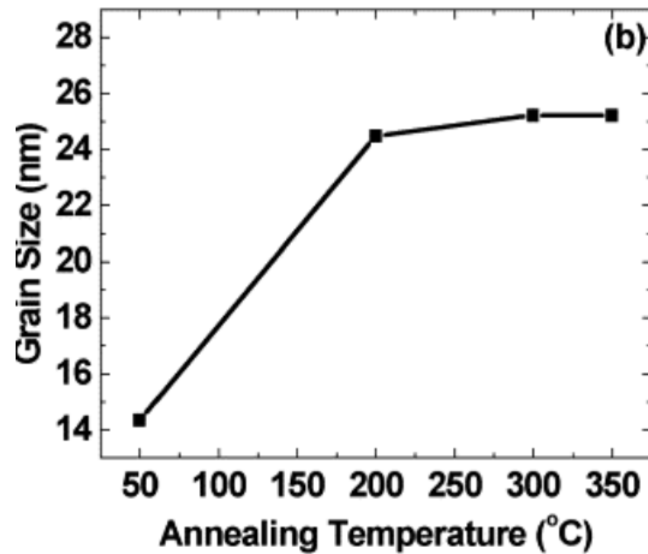

Figure 2.11: Calculated grain size of Ag in a multilayer film [42].

By combining the knowledge obtained from XRD patterns in Figure 2.10 and grain size analysis in Figure 2.11, the decreasing resistance shown in Figure 2.9 before the temperature reaches 300 °*C* can be attributed to the promotion of the Ag crystallization which leads to grain growth and subsequently decrease in the grain boundary density in Ag microstructure [45, 46]. As discussed earlier, reducing grain boundary scattering can ease electron conductance and improve electrical conductivity [13]. On the other hand, with an increase in the annealing temperature above 400 °*C*, there can be seen different peaks appear in the XRD patterns in Figure 2.10. The formation of these peaks is associated with the atom interdiffusion between the Ag/Zn layers and the oxidation of the Ag layer [43]. Hence, the increased oxygen content in the Ag layer resulted in higher resistance [41].

Hajakbari et al. studied the effect of thermal treatment temperature namely 300, 400, 500, and 600 °*C* on the crystal structure and surface morphology of 40 nm Ag films deposited on quartz substrates [47]. Different from previous studies which reported an increase in the Ag film crystallinity until annealing temperature 300 °*C* [39, 41, 42, 43], they observed that the intensity of Ag (111) curves increase up to 500 °*C* [47]. This difference in the impact of annealing temperature on the Ag film can potentially result from the difference in Ag film thickness.

Hajakbari et al. also examined the surface morphology of the Ag films annealed at different temperatures by utilizing SEM and the micrographs are shown in Figure 2.12. It can be observed that the Ag films exhibit a smooth surface without any heat treatment process, while the roughness of the surface increases due to the formation of holes (300 °*C*) and segregation of particles (400 °*C*) followed by enlarged gaps between the particles (600 °*C*) [47]. Santbergen et al. [48] and Hsieh et al. [49] also reported similar surface properties obtained by annealing.

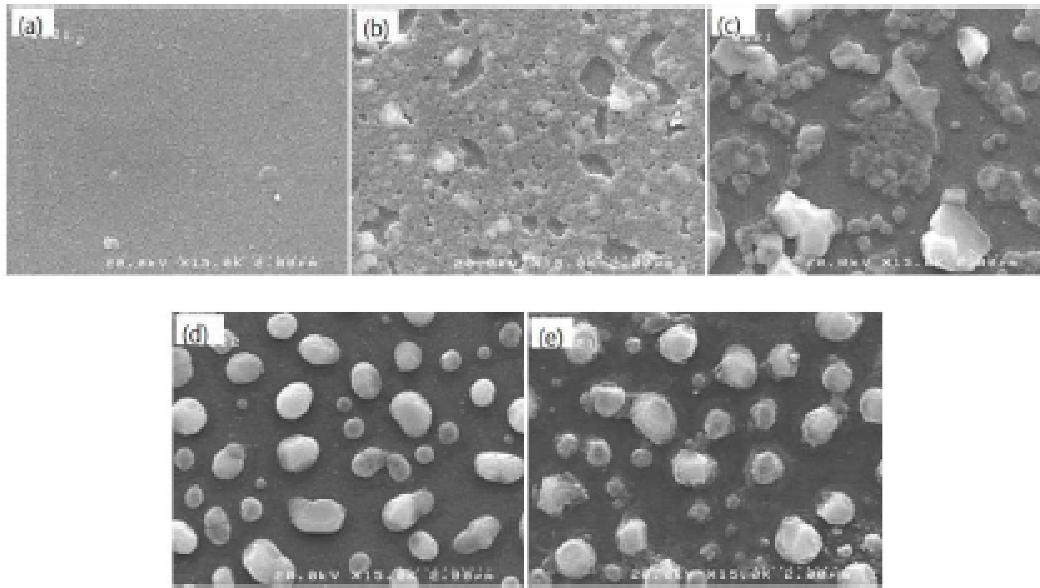

Figure 2.12: SEM images of Ag films on quartz substrate heat treated at different temperatures (a) without annealing, (b) 300 °C, (c) 400 °C, (d) 500 °C and (e) 600 °C. [47].

Annealing time

Another factor that influences the microstructure and resulting properties of the metallic thin films is the duration of thermal treatment. In particular, it is closely related to the annealing temperature since their dynamic combination actually forms the heat treatment characteristic and subsequently the microstructural evolution. The relation between the annealing temperature and the annealing time is given in Figure 2.13 for the grain size evolution of 80 nm thick Ag films. As can be seen, high annealing temperatures can provide faster grain growth [44]. Therefore, one can design and optimize the heat treatment process in terms of temperature and duration in order to obtain a specific grain size for a desired material property.

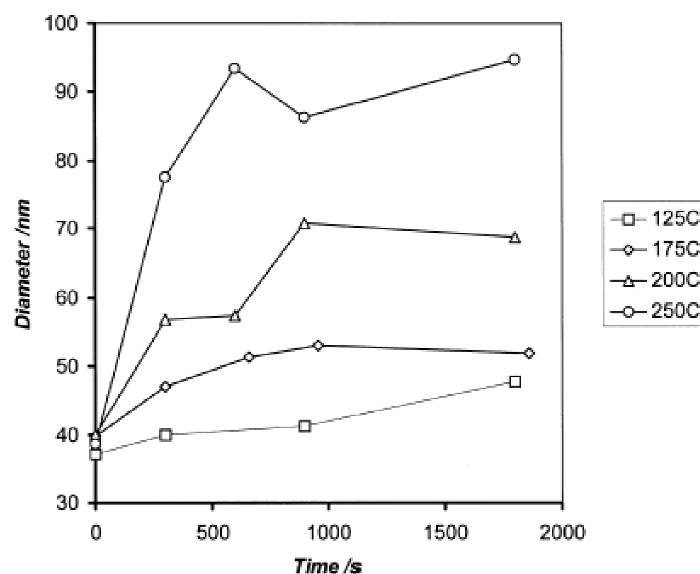

Figure 2.13: The evolution of the grain size of Ag films as a function of annealing temperatures and the duration of annealing [44].

Singer et al. [39] measured the RRR of copper layers with different thicknesses in the range of 5-20 μm with changing annealing time. Figure 2.14 illustrates how the RRR values of copper coatings change as a function of annealing time in the case of 550 $°C$ annealing temperature. It shows that the annealing time plays an important role in modifying the RRR value. Depending on the application of the material, one can tune the duration of the annealing and obtain the desired material properties. In this study, they also state that RRR is significantly improved at the annealing temperature range of 350-400 $°C$ [39]. However, they do not provide information regarding the effect of annealing time on this RRR behavior of copper samples at that annealing temperature range. This knowledge could have been useful in understanding the relationship between the annealing temperature and annealing duration in order to optimize the heat treatment process. We would expect that there is a threshold value that the RRR starts being negatively affected by annealing time after this limit similar to the RRR behavior at an annealing temperature of 550 $°C$ shown in Figure 2.14.

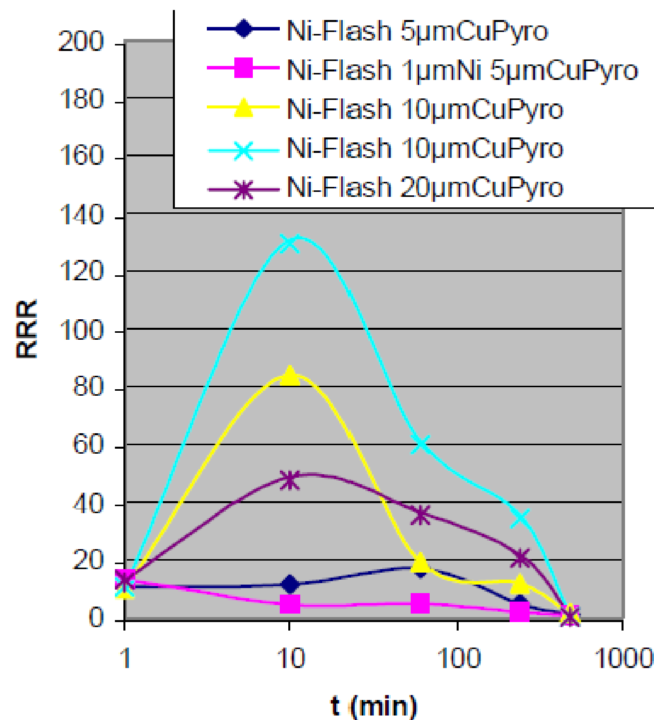

Figure 2.14: The effect of annealing time on the RRR of copper coatings with thicknesses varying from 5 to 20 μm [39].

Annealing ambience

The heat treatment atmosphere plays a crucial role in determining metals' electrical and thermal properties by affecting the impurity or oxygen content introduced into the material during annealing. Figure 2.9 presents the evolution of the resistance of a multilayer material system containing a 0.64 cm thick Ag layer with changing annealing temperature under different conditions namely vacuum, N_2, and air. It can be seen in Figure 2.9 that vacuum annealing gives the highest conductivity while the heat treatment under air atmosphere results in higher resistance than other annealing conditions. This is due to the high partial pressure of the oxygen in the air causing the oxidation of the Ag layer [41]. Jung et al. [42] also obtained a similar resistance trend with varying annealing ambiances where the resistance of the material system is linearly changing with respect to the partial pressure of the oxygen present in the atmosphere.

2.6.2. Purity level

Section 2.4 discusses the fundamental physics behind the low-temperature electrical and thermal behavior of metals, focusing mainly on the nearly pure metals. However, it is very challenging to obtain nearly pure materials in real life so impurities exist in the microstructure of the materials. Thus, this section aims to investigate further the effect of impurities on the electrical and thermal properties of metal by particularly focusing on the influence of the impurity concentration.

The free electron model states that the resistivity of a metal tends to increase proportionally with the impurity level due to electron scattering [50]. We also know from Section 2.4 that in low temperatures impurity scattering becomes the dominant factor determining the resistivity of the metals as shown in Figure 2.2a. Figure 2.2a shows that the resistivity at high temperatures is independent of the impurity content while the low-temperature resistivity is determined by the purity level. Therefore, the RRR value of the materials provides a good indication of the metals' impurity level since it is described as the ratio of resistivities at room temperature (290K) and liquid He temperature (4.2K) as shown in Equation 2.3 [51].

Muimura et al. [52] investigated the potential of the RRR value as a precise purity evaluation tool for the copper specimens with purities of 5N (> 99.999%) and 6N (> 99.9999%). They found that the measured RRR values are affected by the purity level of the copper samples as illustrated in Figure 2.15. It can be observed in Figure 2.15 that different purity levels result in different RRR values independent of the specimen diameter.

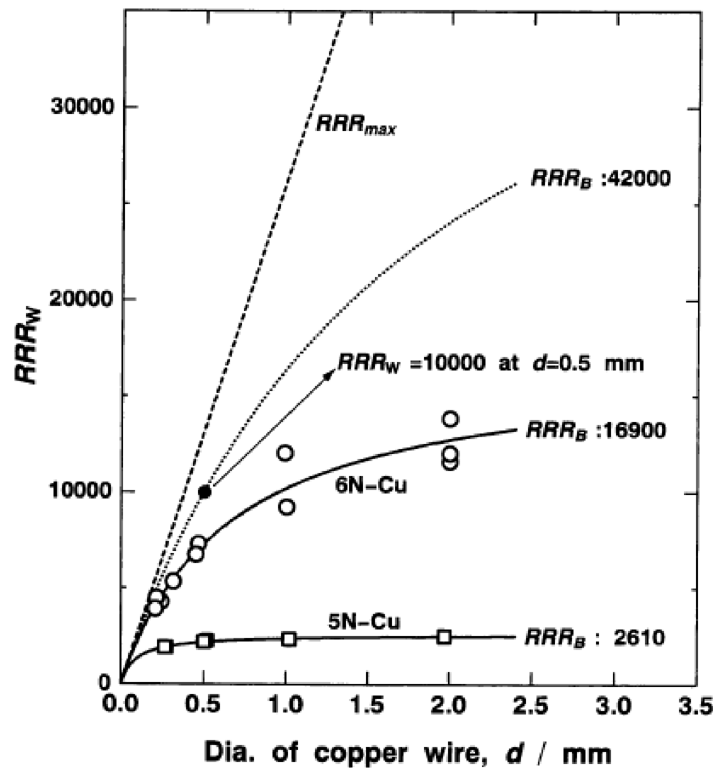

Figure 2.15: RRR values of 5N and 6N copper wire specimens as a function of wire diameter d (The dashed and dotted curves represent the calculated RRR values while the solid curves indicate the measured RRR of copper specimens). [52].

2.6.3. Film thickness

The thickness of a coating is considered one of the most effective parameters to achieve desired electrical and thermal performance [40]. Fuchs's theory presents the general relationship between resistivity and film thickness and states that the effect of thickness is caused by the contribution of diffuse and specular scattering of the conduction electron on the film surface [25]. Luo et al. supported this theory by reporting that the rough surfaces exhibit more diffuse scattering and result in an increased resistivity [53].

Arbab [46] studied the effect of Ag thin film thickness on the final electrical properties of a multilayer material system. Figure 2.16 shows how the electrical resistivity of Ag thin film changes with the thickness. The electrical conductivity of Ag film is significantly low below 30 Å, however, it improves drastically with increasing thickness until around 100 Å [46]. In the thickness range of 100-500 Å, no significant effect on the electrical conductivity was observed by increasing the thickness [46]. Their findings revealed that the contribution of the surface properties to the resistivity decreases as the film thickness increases [46]. It was attributed to the fact that the film thickness approaches the mean free path (l) of the conduction electrons [46]. The mean free path (l) of silver was reported as 42 Å > l_e > 20 Å for energies between 5.5 and 8 eV. It can be clearly observed in Figure 2.16 that the contribution of the surface properties to the resistivity decreases once the thickness reaches the reported mean free path l values in the literature [46].

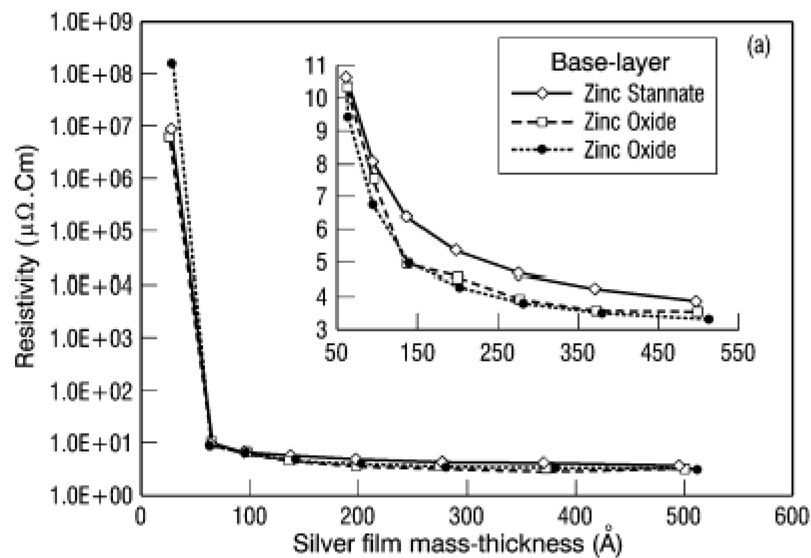

Figure 2.16: Electrical resistivity of Ag films deposited on various substrates as a function of mass-thickness [46]

Similar to Arbab [46], Singer et al. [39] also investigated the dependence of electrical properties on the film thickness and additionally, they presented their work by relating their resistivity to low-temperature properties with the help of RRR. RRR vs layer thickness plot of copper films is illustrated in Figure 2.17. It reveals that RRR can be improved by increasing the thickness of the film [39]. However, it should be noted that, unlike the previous work, their samples are heat-treated. Therefore, for non-heat treated samples the relation between the RRR and thickness might not be exactly the same as one shown in Figure 2.17 since the effect of annealing on RRR can be also altered by the thickness of the film.

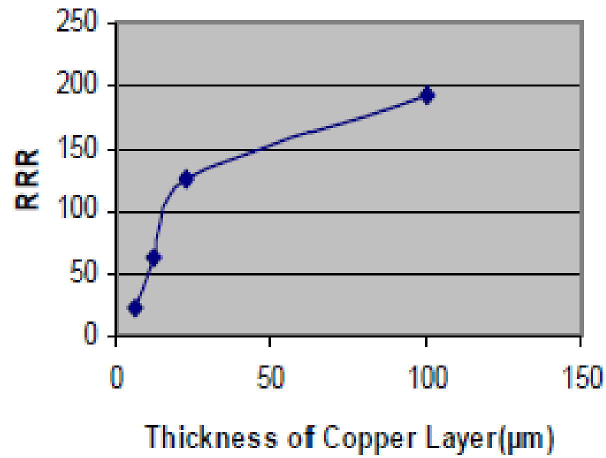

Figure 2.17: Dependence of copper RRR (annealed at 550 °C for 10 min) on the layer thickness [39]

Pal et al. [54] discovered that film thickness plays an important role in the properties of Ag thin films. They performed XRD analysis to characterize the microstructure of Ag film to be able to justify the resulting material properties. Figure 2.18 shows that with increasing film thickness the intensity of crystal planes is enhanced. This phenomenon can be attributed to the greater volume that X-rays can diffract, resulting in a higher number of detected crystallographic planes. As mentioned earlier, improved crystallinity lowers the electron scattering at the grain boundaries, consequently enhancing the electrical conductivity of the material [45, 46].

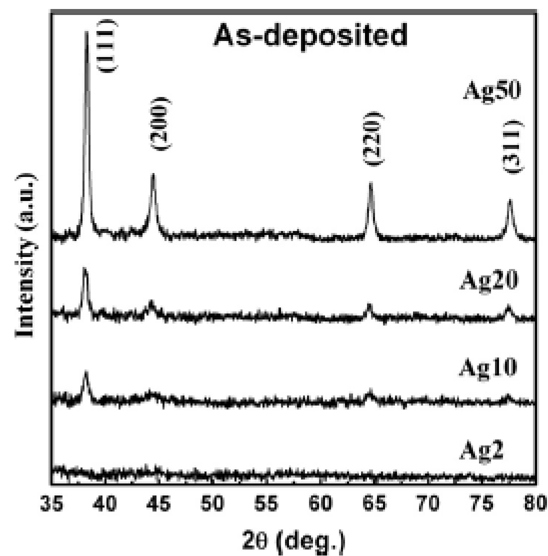

Figure 2.18: XRD of as-deposited Ag films with film thicknesses of 7 nm (Ag2), 15 nm (Ag10), 31 nm (Ag20) and 60 nm (Ag50) [54]

2.6.4. Aging and storage

Material properties are susceptible to change in time by storage conditions such as temperature and humidity [38]. Thus this section focuses on the potential impact of aging and storage conditions on the low-temperature electrical and thermal properties of metals. As discussed in Section 2.4, the microstructural evolution of the metals can have great importance for low temperatures, although their effect at room temperatures can be considered minor [14].

Jung et al. [42] reported that the microstructure of the Ag coating of a multilayer material system underwent a change in 3 months of time frame. Figure 2.19 displays the optical microscopy images of Ag coating right after the fabrication (a) and after 3 months (b). It can be observed that more white spots appeared as time passed [42]. Figure 2.19 (c) also provides a closer look at one of the white spots that grew large with time. It is attributed to the generation of more defects due to the corrosion of Ag [42]. Therefore, depending on the storage conditions namely oxygen and humidity levels, and the time frame the material is exposed to these environmental conditions, the concentration of the microstructural imperfections can increase. As a consequence, the low-temperature electrical and thermal resistivity of metals can change.

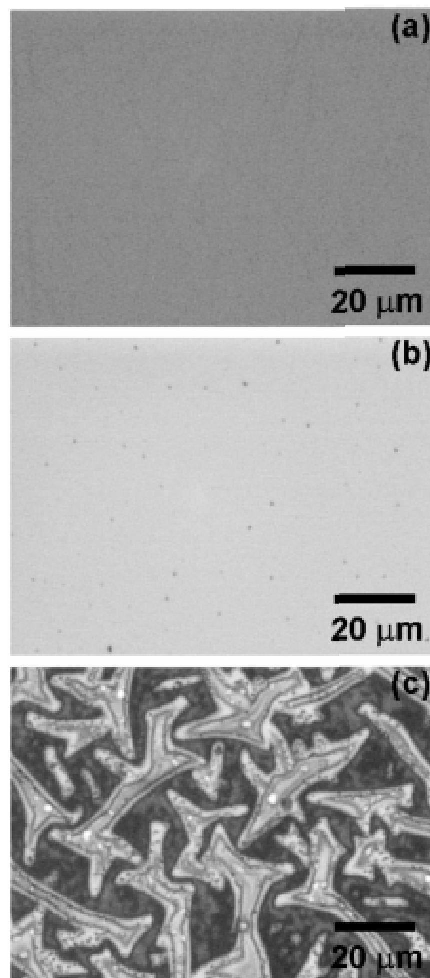

Figure 2.19: Optical microscopy images of Ag layer of multilayer films taken (a) immediately after the fabrication, (b) three months after the fabrication and (c) closer image of a grown spot [42].

2.7. Concluding remarks

In quantum computers where a highly complex wiring system is required and operation temperatures drop down to liquid He temperatures, the i/o system of these devices faces new challenges. The metalized polymeric design of cables provides a promising solution in terms of flexibility and scalability, although their material properties should be tailored to be functional under cryogenic temperatures. The relevant material properties were found to be electrical and thermal conductance. The main challenge of the i/o system of quantum computers was introduced as controlling and optimizing the material properties such that the metal has sufficiently good electrical conductivity and relatively poorer thermal conductivity. Since these two requirements are controversial, it was presented as a materials science challenge to discover more in this literature study.

The main findings of this literature study are the following:

- RRR is a good method to show the relationship between the room temperature and low-temperature resistivities of metals.
- RRR is highly dependent on the atomic imperfections present in the microstructure.
- The deposition parameters of metallic thin films during the evaporation and sputtering play a crucial role in the resulting film structure.
- Electrical and thermal behaviors of metals can be modified by the microstructural evolution obtained by heat treatment, different film thicknesses, impurity content, and aging and storage conditions.
- Current literature lacks deep information and discussion about the RRR of silver and how it depends on the microstructure modified by external factors

As a result of the findings of this literature study, it can be argued that the current literature mainly consists of information about the electrical and thermal properties of silver when it is used in multilayer material systems. Resistivity measurements of these multilayer material systems usually fail to represent the pure resistivity of silver, which is desired for the design of cabling systems for quantum computers. Furthermore, data on the resistivity measurements at cryogenic temperatures was also limited and not sufficient to explore the low-temperature behavior of silver films. Therefore, systematic research on the silver RRR and the dependence of its behavior on external factors can enormously contribute to the current literature.

2.8. Research question

The research question of this graduation project following this literature study is formulated as:

"What is the RRR of the silver film of a finished Cri/oFlex and how does it depend on the fabrication process?".

The fabrication process involves variables such as the heat treatment process and its parameters, lamination steps, silver purity level, film thickness, and aging and storage conditions.

3

Materials and Methods

3.1. Materials

The material system of this study consists of two main components: Polyimide (PI) as the substrate and Silver (Ag) as the metallic thin film. Figure 3.1 demonstrates two example images of these materials. The cross-section of the material system is also shown in Figure 3.2. The substrate material PI is 1 mil (~ 25 μm) thick and has an additional adhesive layer on one side with a thickness of 0.5 mil (~ 12.5 μm). As can be seen in Figure 3.2, the silver film is deposited on the side of PI which does not contain the adhesive layer. Silver film thickness on the PI substrate can be adjusted by deposition parameters. In this study, we used 0.25 μm, 1 μm and 2 μm silver thicknesses. The purity of the silver varied between 99.95 % (3N5) to 99.995 % (4N5) depending on the deposition run.

(a) Silver granules before the deposition [55]

(b) A roll of PI film [56]

Figure 3.1: Example pictures of the materials

Figure 3.2: A schematic of the material system

3.2. Methods

3.2.1. Sample preparation

Samples were prepared by following particular steps to imitate the actual fabrication process of cryogenic flexible cables. Figure 3.3 shows four main sample preparation steps: deposition, heat treatment, laser patterning, and lamination runs. It is important to note that lithography is being used for patterning in the real fabrication process instead of a laser. In this project., we used laser patterning instead to ease the sample-making process in terms of time and effort.

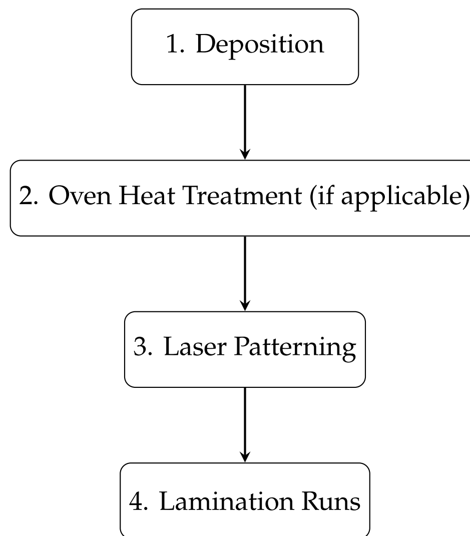

Figure 3.3: Fabrication steps

3.2.1.1. Deposition

The electron beam (e-beam) evaporation technique was used to deposit silver on the PI substrate. It is a physical vapor deposition method and its working principle is based on using focused electrons to heat up the silver by using a magnetic field. Vaporized silver travels out of the crucible and coats the PI. The e-beam evaporator utilizes the roll-to-roll system, which allowed us to coat approximately 3 m long PI in a single deposition run. Figure 3.4 shows a schematic of how the roll-to-roll system looks. A PI roll is shown in Figure 3.1b can be attached to it conveniently and once the deposition run is over, metalized PI film can be taken out from the second roll. For 2 μm thick silver film, the rate of the deposition is 90 Å/s with a roll-to-roll speed of 0.612 mm/s. In order to obtain different thicknesses, roll-to-roll speed can be adjusted. For instance, the roll-to-roll speed would be doubled to 1.224 mm/s for 1 μm thick silver film.

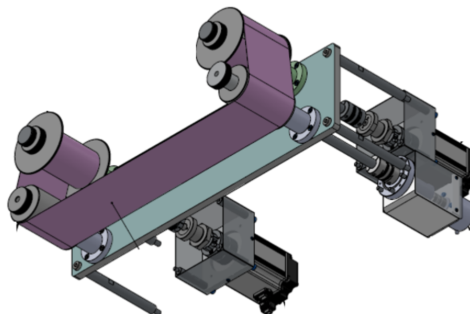

Figure 3.4: A schematic for roll-to-roll setup
[57]

3.2.1.2. Heat treatment

For the second step of the sample preparation, samples were divided into two groups. Half of the samples were kept pristine and the other half were heat treated. A laboratory oven was used for the heat treatment and the atmosphere of the furnace was air. Silver-deposited PI rolls were subjected to 180 °C temperature for 5 hours. Samples were loaded into the oven only after reaching the final temperature of 180 °C and unloaded immediately after 5 hours. They were left to cool down to room temperature in still air. Therefore, the cooling rate was not controlled.

3.2.1.3. Laser patterning

A laser machine was used to make resistivity patterns by selectively removing silver from the PI. Figure 3.5 illustrates the pattern for resistivity measurements. White areas represent the silver film, while the black lines indicate the ablated areas of the silver film that reveal the PI sheet underneath. As can be seen in Figure 3.5, the pattern was particularly designed with four contact points for four-probe resistance measurements.

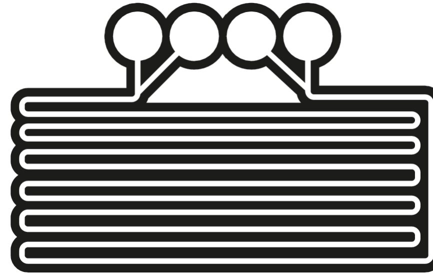

Figure 3.5: The resistivity pattern of the samples

3.2.1.4. Lamination runs

After the silver film was patterned by laser, samples were subjected to different lamination runs namely non, one, three, and four times since cryogenic flexible cables typically undergo three or four times lamination runs during the actual fabrication process. Each lamination run involved subjecting the samples to a temperature of 295 °C temperature for a duration of one hour and 20 minutes, excluding the time required for both heating and cooling processes. It's worth noting that the samples were loaded into the laminator at ambient room temperature before initiating the heating phase. Similarly, the collection of samples occurred only after the laminator chamber temperature cooled down to 80 °C. This controlled lamination process was executed under a vacuum pressure of 80 mbar, and in addition to the vacuum pressure, physical pressure was also applied through pistons.

Table 3.1 summarizes the essential elements of sample naming in this project depending on the fabrication processes, especially heat treatment and lamination runs. Although we investigated different parameters in sample fabrication such as the film thickness and purity of silver, the heat treatment procedure and lamination runs were kept constant throughout the thesis.

Processes	Heat Treatment?	Lamination Runs?	Sample ID
Samples	NHT	0	NHT_L0
		1	NHT_L1
		3	NHT_L3
		4	NHT_L4
	HT	0	HT_L0
		1	HT_L1
		3	HT_L3
		4	HT_L4

Table 3.1: Sample naming depending on the fabrication process

Figure 3.6 shows a picture of the full set of samples which include unlaminated, one-time laminated, three-times laminated and four-times laminated samples for both heat-treated (HT) and non-heat treated (NHT) cases. The samples that were prepared by three and four lamination runs (NHT L3, NHT L4, HT L3 and HT L4) had an additional encapsulation layer of 0.5 mil PI, as can be seen in Figure 3.6. PI contains an additional adhesive layer on one side and once it is heated up above the melting temperature (260 °C), this adhesive layer acts as a glue and sticks the PI to the surface of the patterned silver film. As shown in Figure 3.6, four contact points of the pattern were kept open to allow resistivity measurements. The reason for encapsulation at the third and the fourth run is to imitate the actual fabrication procedure since cables are encapsulated at their last lamination runs during standard production. Depending on how well they meet the requirements to pass to the next fabrication steps, they go through either three or four lamination runs. The sample size for each lamination run was six to improve the reliability of the measurement data.

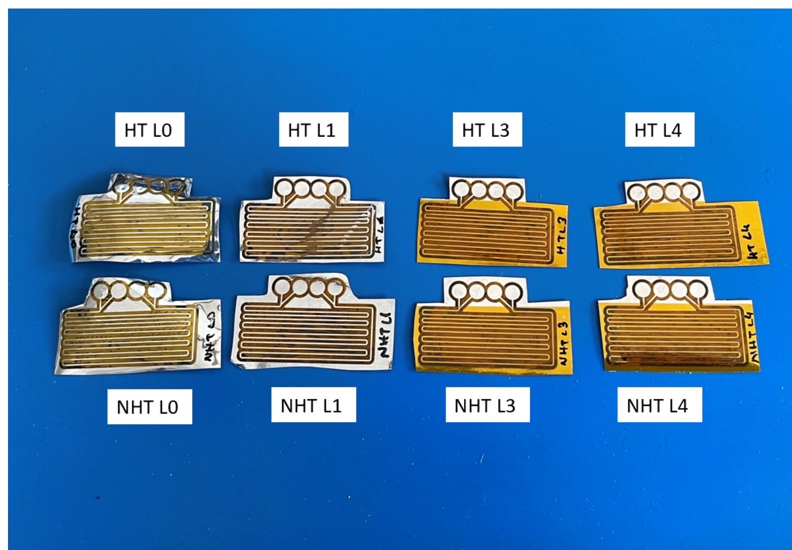

Figure 3.6: Full set of samples after designated lamination runs

3.2.2. Cryogenic measurements

Cryogenic measurements were done by using a dipper probe. It is one of the classical techniques that involves directly immersing the sample in cryogenic liquid [14]. Figure 3.7a shows a scheme of the basic dipper cryostat design. It consists of liquid cryogen at the bottom, in which the sample holder is immersed. The sample holder is linked to the connector head with the support tube. A similar design of a dipper cryostat was used for the cryogenic measurements of this study. Figure 3.7b shows the picture of the dipper used for this thesis. The storage dewar contains Helium (He) as a cryogenic liquid and the temperature range for electrical resistivity measurements was 293 K-4.2 K, which corresponds to the room temperature and liquid He temperature, respectively. As can be seen in Figure 3.7b, a pulley system was utilized to lower the dipper probe into the cryogenic liquid containing dewar. Figure 3.7b demonstrates how the dipper probe was hooked up. This pulley system provided relatively easy operation and reasonable control over the temperature gradient of the sample by adjusting the height of the probe above the liquid surface.

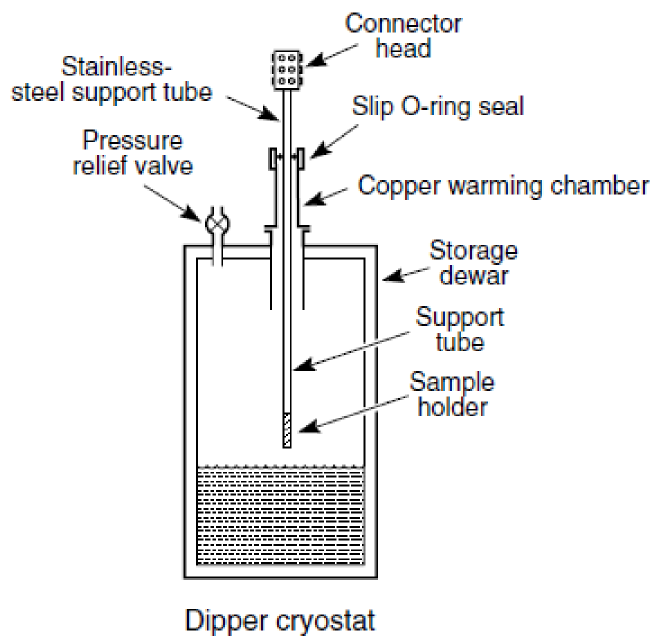

(a) Schematic of an immersion measurement probe in a high-pressure storage dewar containing the cryogenic liquid [14]

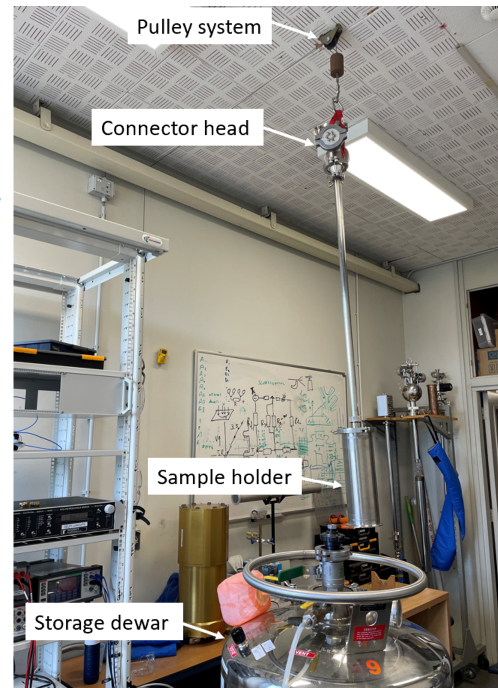

(b) The cryogenic measurement setup with the dipper probe and He storage dewar

Figure 3.7: Cryogenic measurement setup

In order to increase the efficiency of the measurements in terms of time, effort, and He consumption, a two-sample measurement setup was developed for this project. Figure 3.8 shows the configuration of this sample holder arrangement. The sample holder was attached to the end of the dipper probe in such a way that its two faces could be used for the test samples. This double-sided measurement setup allowed us to measure the resistivities of two samples simultaneously. The sample holder was made out of Aluminium (Al). Silver paint was used to stick the test sample to the Al block. The purpose of using the silver paint was not only to attach the test sample to the holder but also to ensure thermal contact between the sample and the sample holder.

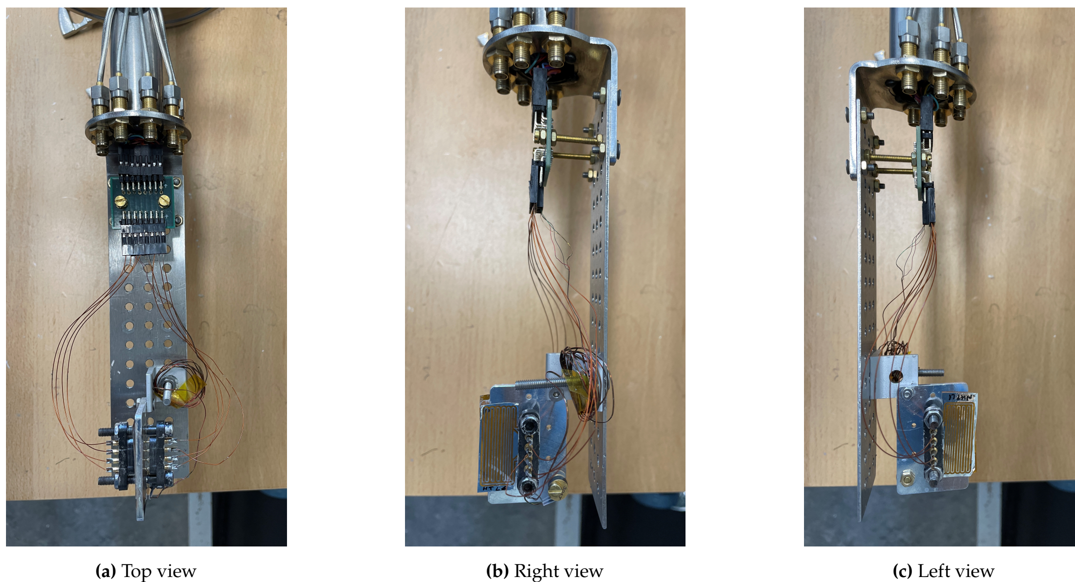

(a) Top view **(b)** Right view **(c)** Left view

Figure 3.8: Sample holder configuration of the dipper probe used for cryogenic measurements

Figure 3.9 illustrates the four-lead measurement arrangement which consists of two pairs of leads: one pair for the voltmeter and one pair for the current source. Since they are independent of each other, it is possible to avoid the artificially enhanced voltages resulting from the current flowing through the contact resistances and wires of the circuit. The four-lead arrangement provides more accurate data by ensuring the true sample voltage reading at the voltmeter.

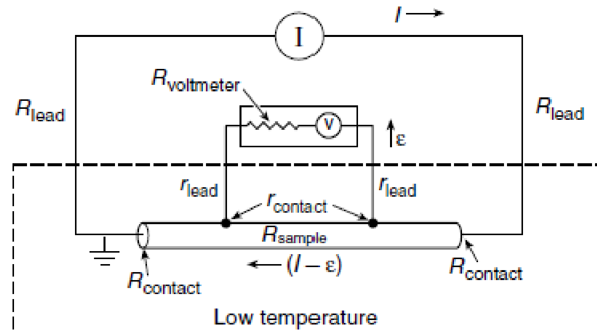

Figure 3.9: Four-lead arrangement for measuring electrical resistance. Figure taken from [14].

Figure 3.10 demonstrates how four wires were connected to the sample by using spring-loaded pogo pins. The black pogo pin holder was screwed into the sample holder in such a way that there is just enough space between the pogo pin holder and the sample to compress pogo pins halfway through their length. This way, sufficient contact between the pogo pins and the patterned four contact points of the silver film was obtained. The standardized pattern of the silver film samples provided a convenient way to contact pogo pins with the matching four-point silver pattern.

A silicon diode was chosen as the cryogenic thermometer in order to track the temperature of the samples during immersion. It is a diode voltage sensor and it operates with reasonably good accuracy over the temperature range of 1.5 K and 300 K, which was sufficient for the temperature scope of this study [14]. Figure 3.10 shows how the silicon diode was attached to the Al block as the temperature sensor.

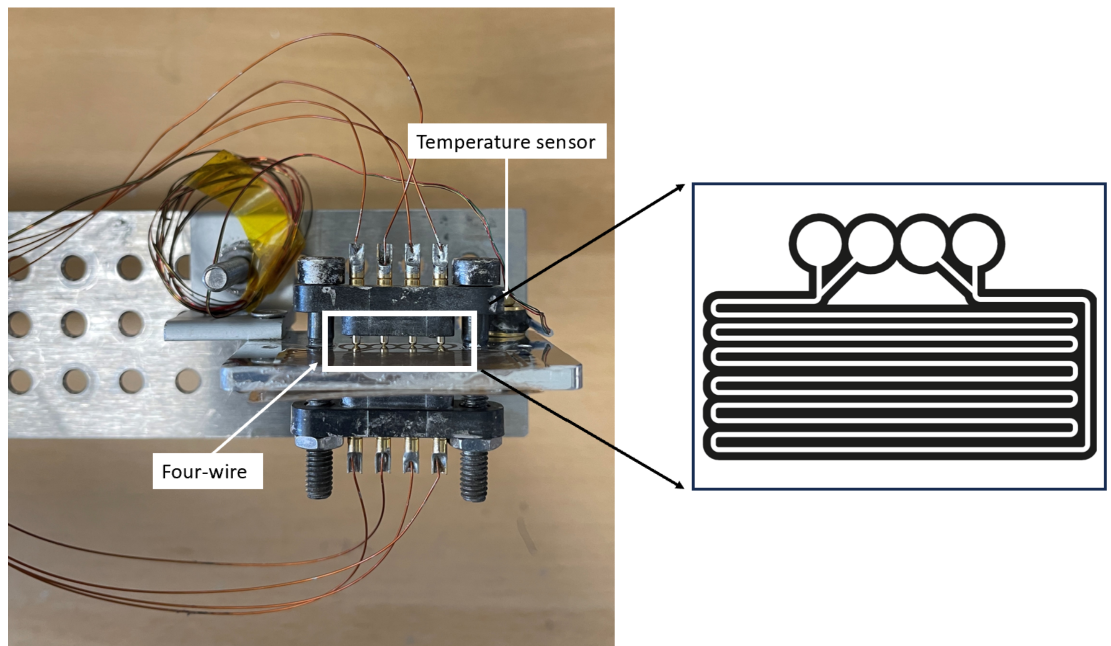

Figure 3.10: Four-wire resistance measurement setup

For the measurements, three Keithley DMM6500 6 1/2 model digital multimeters were used. While two of them were connected to two samples for resistance measurements, one of them was used for diode measurements to determine the sample temperature. The digital multimeters were operated remotely by using a measurement script.

3.2.3. Data analysis

Figure 3.11 displays an example of a result obtained from a four-wire resistance measurement. While Figure 3.11a plots the resistance vs time, the resistance changes with respect to the temperature are shown in Figure 3.11b. As can be observed in Figure 3.11a, the amount of time required for warming up and cooling down the sample was quite different. Cool down was a considerably faster pace process compared to warm up. This is because the cooldown is quite sensitive to handling in terms of temperature changes once the dipper probe is already in the dewar. Moreover, the dipper probe was kept attached to the top part of the dewar which was protected with a metal shield until the sample temperatures get closer to the room temperature at the final stage of the measurement. On the other side, Figure 3.11b shows an example graph of how the sample resistance is changing with the temperature once the dipstick is lowered in the dewar. As can be seen in Figure 3.11b, cool-down and warp-up curves overlap reasonably well throughout the measurement. It provides a checkpoint for the cool down whether the measured sample resistance value corresponds to the actual temperature of the sample. Since the cooldown might be unstable and difficult to control during immersion and on the other hand, warmup is quite stable with the help of the protective shield, this plot in Figure 3.11b was treated as a pass/fail criterion for the measurements since it reveals the accuracy of the data by comparing the cooldown to the warmup.

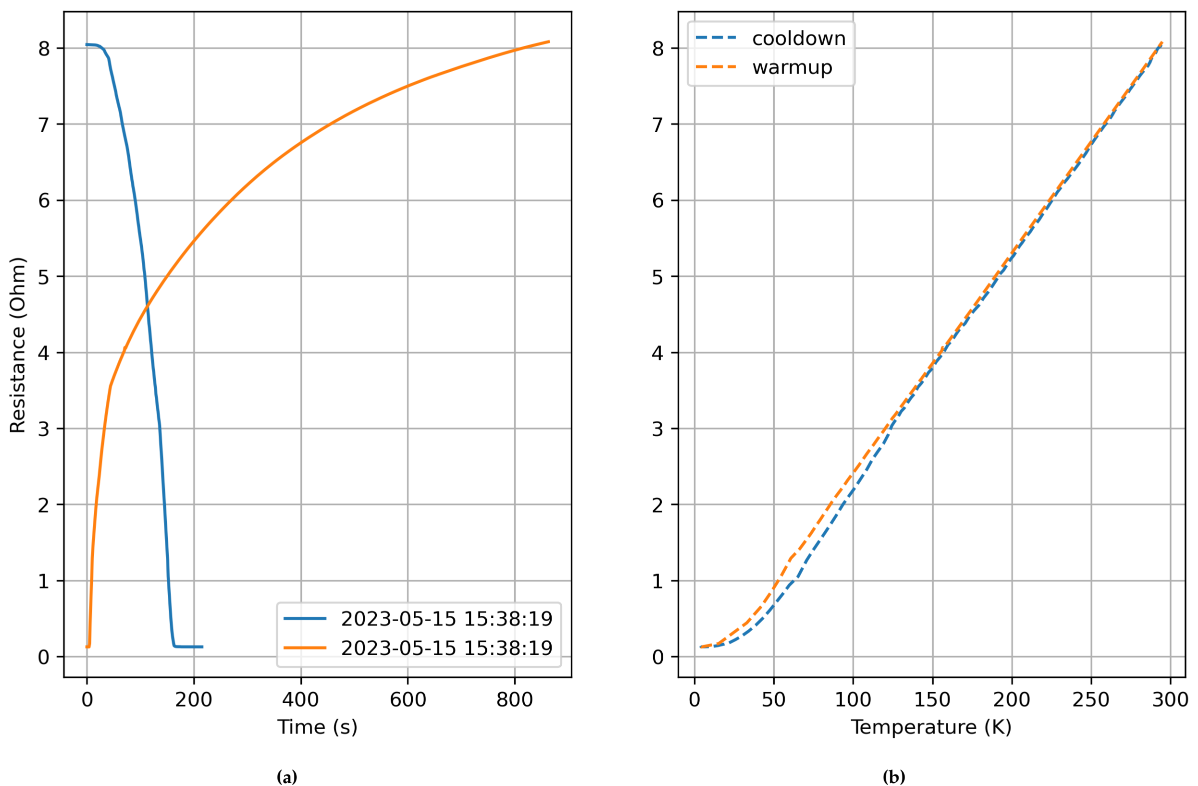

Figure 3.11: Example of: (a) Resistance vs Time plot and (b) Resistance vs Temperature plot

Figure 3.12 demonstrates changing sample resistance and thermal conductivity with respect to the temperature in a logarithmic scale. Using the logarithmic scale in Figure 3.12a helped reveal discontinuous characteristics of the data points at low temperatures as opposed to its look in Figure 3.11a. With this plot, we realized the importance of performing the cryogenic measurement at a relatively slow and controlled pace in terms of the quality and accuracy of the data. In Figure 3.12b, the thermal conductivity of the silver was plotted with respect to the temperature during warmup. Thermal conductivity was calculated by the Wiedemann-Franz-Lorenz law given in Equation 2.10. The trend of the thermal conductivity curve given in Figure 3.12b corresponds to the experimentally measured thermal conductivity curves presented in the literature and shown in Figure 2.5.

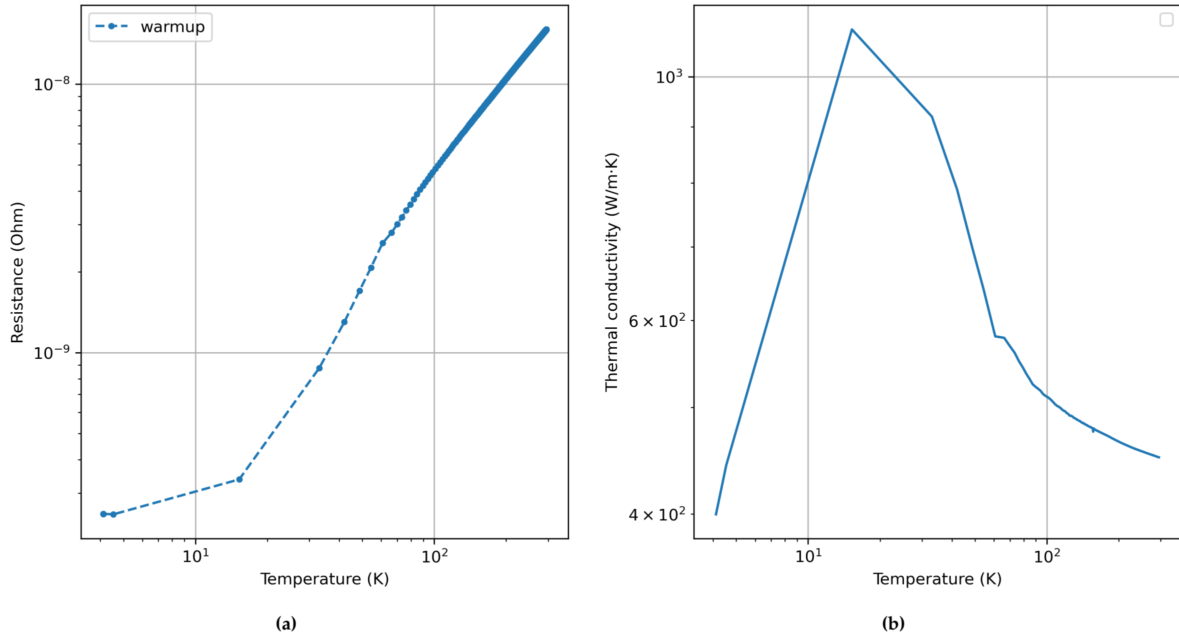

Figure 3.12: Example of: (a) Resistance vs Temperature plot and (b) Thermal Conductivity vs Temperature plot

The RRR was used as a tool to interpret the measurement data in terms of the relation between the electrical and thermal properties of silver and their temperature dependence. RRR value for each specimen was calculated by a Python script. The function of the code was to go through the data file containing time, voltage, temperature and resistance information and take the ratio of two resistances at cryogenic and room temperatures as given in Equation 2.3. The cryogenic temperature was the liquid He temperature (4.2 K) and the room temperature was taken as the value of the close to 293 K within the range of 292 K and 294 K. In this way, RRR calculations were standardized and performed the same way for every measurement sample.

3.2.4. Material characterization

For the material characterization, X-ray diffraction (XRD) and Scanning Electron Microscopy (SEM) were used. XRD was utilized to detect new phases formed in the material as a result of the heat treatment. Texture analysis was also performed to investigate the effect of heat treatment. SEM (Jeol JSM IT-100) was used to analyze the microstructure of the silver as a result of oven heat treatment and thermal cycles due to the lamination runs. Energy Dispersive X-ray spectroscopy (EDS) analysis was also utilized to detect contamination and oxidation.

4

Results and Discussion

The dependence of RRR on several fabrication, design and post-process parameters is presented in this chapter. These parameters are heat effects (lamination and oven heat treatments), silver purity, film thickness, and, aging and storage. The results are presented in graphs which are plotted with an error bar of one standard deviation (one sigma).

4.1. Heat effects

In this thesis, we investigated the effect of heat on the silver RRR by using two different treatment techniques: lamination treatment and oven heat treatment. The reason for investigating two different heat treatment techniques is that both are included in the fabrication steps of cryogenic flexible cables and they have distinct roles. The lamination process serves to merge the layers of the cables, while the oven heat treatment is applied to silver-deposited PI films to enhance the adhesion strength between the silver film and PI surface. Therefore, it is crucial to study their influence on the silver RRR individually as well as their combined effect, given that the end product undergoes both processes. It should be noted that NHT and HT labels stand for non-heat-treated and oven heat-treated regardless of the lamination runs that they underwent. Depending on the applied number of lamination runs, they are named L0 (unlaminated), one time (L1), three times (L3) and four times (L4). Table 3.1 provides a concise summary of the sample naming convention for reference. This section is structured into five subsections: lamination, oven heat treatment, the comparison of these two heat treatment methods, spread investigation, and white surface finish observed as a result of oven heat treatment.

4.1.1. Lamination

This section explores the influence of the lamination heat treatment on the thin film silver RRR. The lamination process involves heating up to 295 °C while maintaining a vacuum pressure of 80 mbar as well as a physical pressure applied on top of the samples by the pistons. Lamination is a crucial step in making cryogenic flexible cables and during the fabrication cryogenic flexible cables are typically subjected to three or four times lamination. Our goal in this section is to see how the RRR behavior of silver thin film changes as we increase the number of lamination runs. By doing so, the findings of this section will provide a foundational dataset, serving as a benchmark for examining the effects of other critical parameters including oven heat treatment, silver purity, film thickness, aging effects, and storage conditions.

Figure 4.1 shows changing silver RRR with respect to different lamination runs for non-heat-treated (NHT) samples. While the average RRR of NHT samples was found to be 16 ±1 before the lamination, after the first lamination run, the average RRR value of NHT samples was calculated as 52 ±19 as shown in Figure 4.1. The first lamination run led to an increase of ~ 3.3 factors in the RRR mean of NHT samples. When it comes to the third and the fourth laminations, it can be observed in Figure 4.1 that they did not result in a major change in the RRR of NHT samples, especially compared to the effect

of the first lamination run, which approximately quadrupled the RRR. While the RRR mean of NHT samples after the first lamination was 52 ±19, NHT samples showed an average RRR of 63 ±2 and 62 ±3 after the third and the fourth lamination runs, respectively. A slight decrease in the RRR mean of NHT samples was found as a result of the fourth lamination run compared to three times laminated samples.

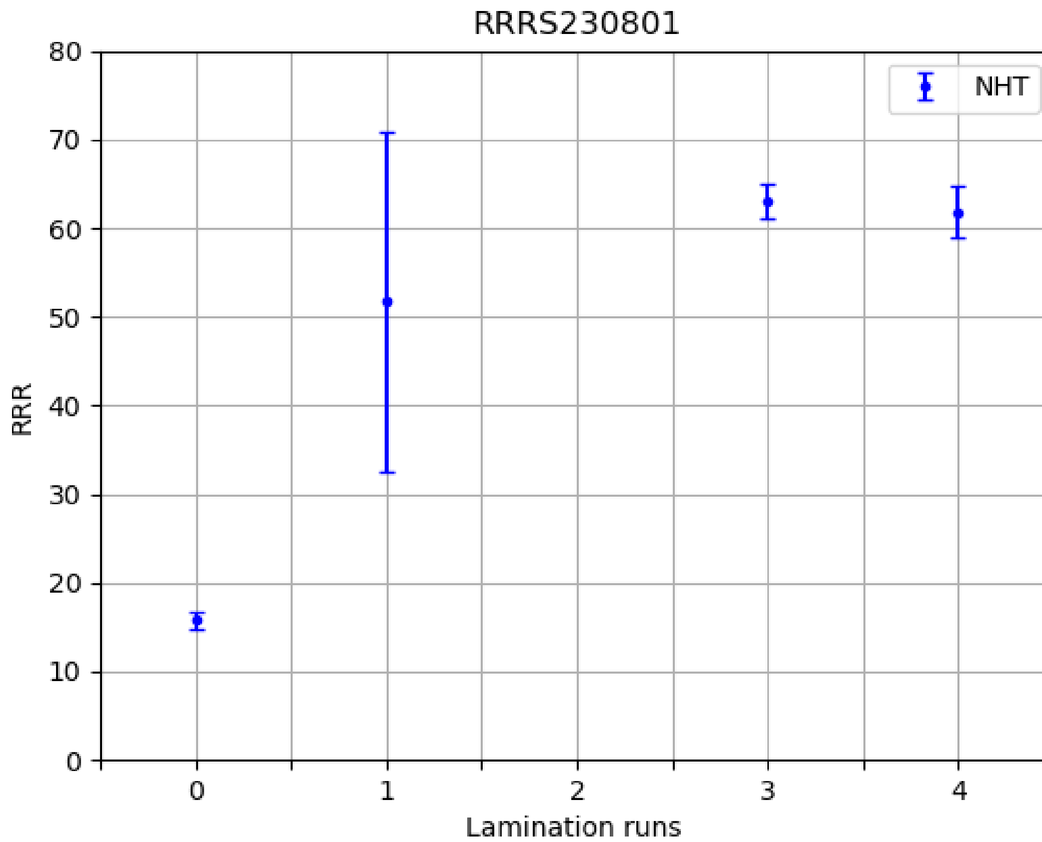

Figure 4.1: The effect of several lamination runs on the RRR value of non-heat-treated (NHT) samples with silver purity = 4N and film thickness = 2 μm. All sets had six samples. Solid circles represent the mean value of the set.

Overall, RRR values were found to be saturated after the first lamination run. Figure 4.1 illustrates a concave downward behavior in the RRR results, indicating that the rate of increase in the RRR mean decelerated overtime before the slope gets eventually negative with an increasing number of lamination runs. The number of lamination runs can be considered as the annealing duration since each lamination run applies heat treatment. Therefore, this concave downward RRR behavior in Figure 4.1 can be associated with the data shown in Figure 2.14 for Ni-Flash 10 and 20 μm CuPyro in terms of the curve trend of the RRR results with respect to annealing time. Our study's outcomes showed similarities with the trends documented in prior research by Singer et al. [39]. However, it is important to emphasize that the film material, purities and thicknesses in the two studies are not identical. Hence, analyzing the two findings beyond the overall curve does not lend itself to drawing conclusive deductions.

4.1.1.1. RRR behavior with further increasing the lamination runs

In order to improve the predictions of RRR and consequently the heat load calculations, the RRR dependence of the silver on the lamination runs was examined further by increasing the number of laminations up to six. Figure 4.2 displays the RRR behavior of NHT samples with varying numbers of lamination runs from three to five. Samples were prepared separately from the samples presented in Figure 4.3. Therefore, the results of these samples were analyzed among themselves to see the RRR trend

with the increasing number of laminations independently from sample-to-sample variations due to the fabrication. Figure 4.2 reveals that RRR of NHT samples increased regularly with increasing lamination runs from three to six. While the mean of RRR was found to be 52 for the three-times laminated samples, the four-times and five-times laminated samples showed RRR of 69 and 72 on average, respectively.

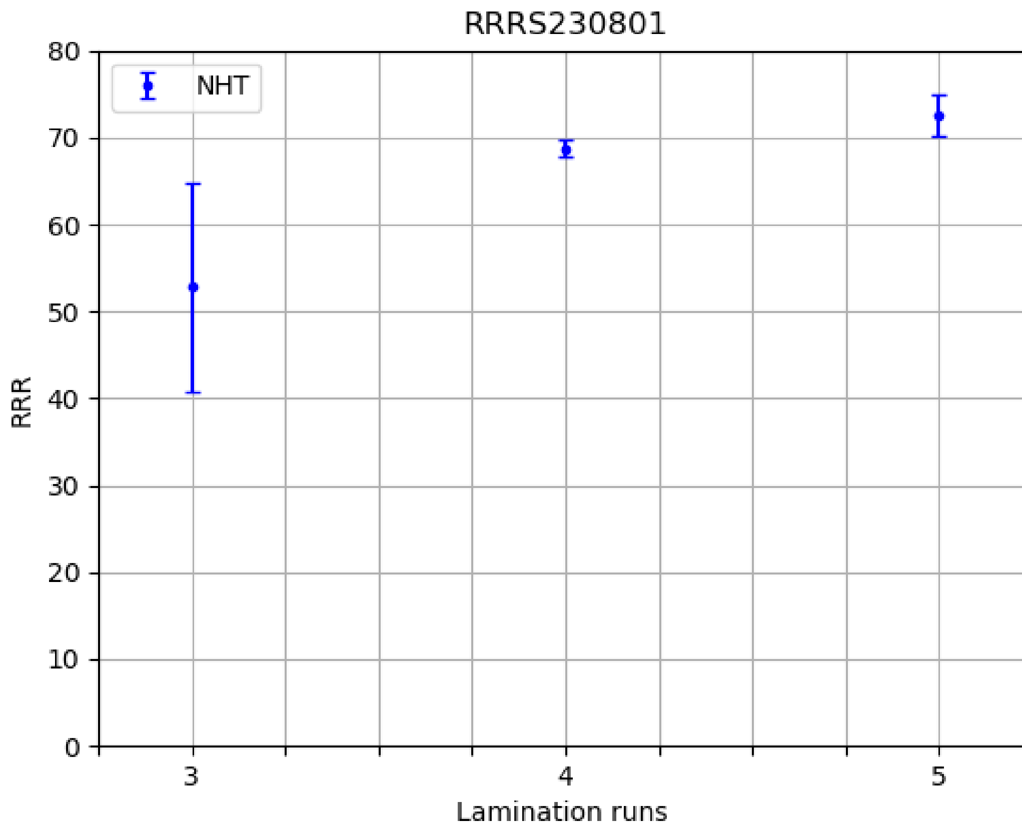

Figure 4.2: RRR behavior with an increased number of laminations up to five. The thickness is 2 μm and silver purity is 4N. All sets had six samples. Solid circles represent the mean value of the set.

4.1.2. Oven heat treatment

This section focuses on the effect of oven heat treatment (HT) on the silver RRR with changing lamination runs, namely none, one, three and four times. It does not only give an overview of the results but also provides a reference for the next sections to compare the parameters such as the film thickness and purity. It should be noted that the silver film thickness was 2 μm and the purity was 99.99 % (4N) for the deposition run called RRRS230801. Resistance measurement results are documented for each sample from the deposition run RRRS230801 in Table A.1.

Figure 4.3 shows changing silver RRR with respect to different lamination runs for non-heat-treated (NHT) and heat-treated (HT) samples. While the average RRR of NHT samples was found to be 16 ±1 before the lamination, the HT samples showed a remarkably higher RRR mean of 38 ±9 as a result of the oven heat treatment. After the first lamination run, the average RRR value of NHT samples was calculated as 52 ±19 as shown in Figure 4.3. When we compare it to the unlaminated samples, it can be said that the first lamination run led to an increase of $\sim$ 3.3 factors in the RRR mean of NHT samples. On the other hand, the average RRR of HT samples was calculated as 55 ±3 as a result of the first lamination run. By that, it was found that the first lamination run increased the average RRR values of HT samples by a factor of $\sim$ 1.5, while its effect was more prominent with the $\sim$ 3.3 factor for NHT samples.

When it comes to the third and the fourth laminations, it can be observed in Figure 4.3 that they did not result in a major change in the RRR of NHT samples, especially compared to the effect of the first lamination run, which approximately quadrupled the RRR. While the RRR mean of NHT samples after the first lamination was 52 ±19, NHT samples showed an average RRR of 63 ±2 and 62 ±3 after the third and the fourth lamination runs, respectively. It can be argued that the fourth lamination run led to a slight decrease in the RRR of NHT samples on average. For HT samples, the average of RRR values decreased from 55 ±3 to 54 ±4 as a result of the third lamination run. This can also be considered as a minor drop in the average of RRR values. The decrease in the RRR values of HT samples from 54 ±4 to 44 ±10 as a result of the fourth lamination was more clear as can be seen in Figure 4.3.

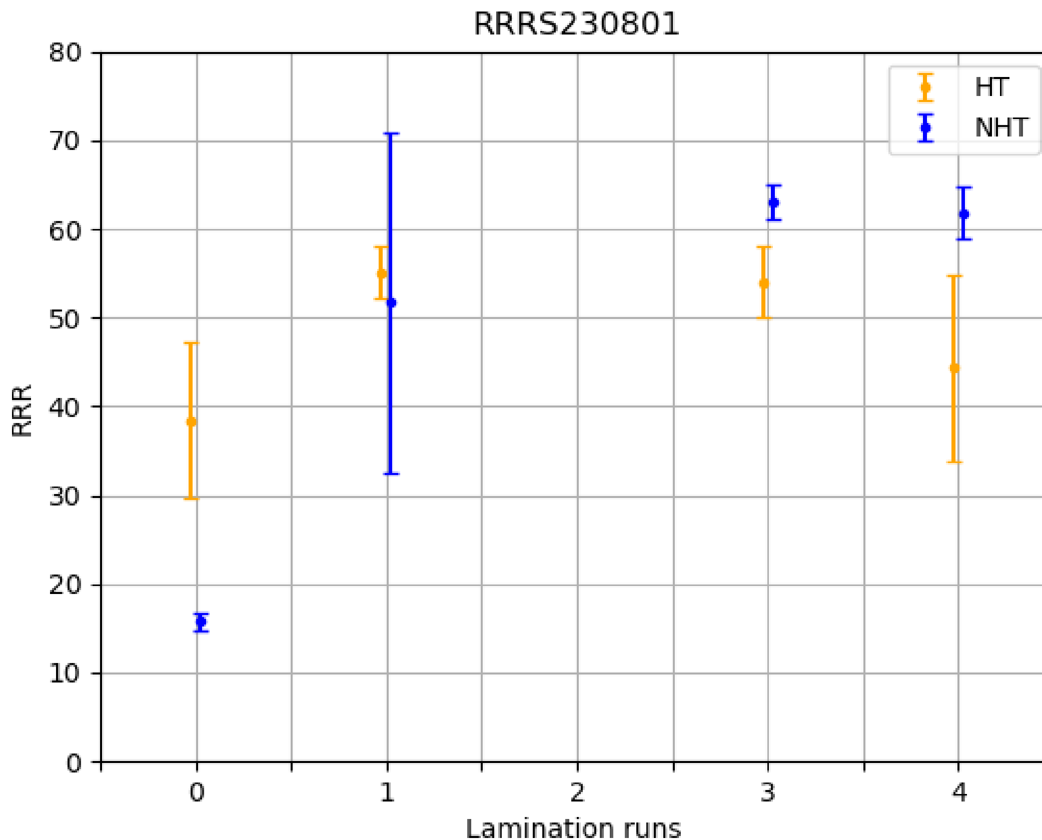

Figure 4.3: The effect of several lamination runs on the RRR value of heat-treated (HT) and non-heat-treated (NHT) samples with silver purity = 4N and film thickness = 2 μm. All sets had six samples. Solid circles represent the mean value of the set.

RRR measurements of the 2 μm silver film with 99.99 % purity revealed that the heat treatment process leads to an increase in the RRR for no lamination case as shown in Figure 4.3. Figure 4.4 presents a comparison of the SEM micrographs of unlaminated NHT and HT samples from the deposition run RRRS230801. While Figure 4.4a and Figure 4.4b show the microstructure of an NHT sample by using secondary electron imaging and backscattered electron imaging respectively, the micrographs of an HT sample are given in Figure 4.4c and Figure 4.4d. SEM pictures revealed that the heat treatment processes resulted in the growth of larger grains within a crystalline structure, leading to a reduction in grain boundary density. Consequently, the RRR was found to be higher for HT samples. This phenomenon is rooted in the fundamental principles of thermally activated grain boundary migration and coarsening [38]. During heat treatment, the energy provided to the material facilitates the diffusion of atoms across grain boundaries, causing grains to coalesce and grow in size [38]. As grain boundaries play a key role in hindering the flow of electrons, fewer grain boundaries result in reduced electron scattering at low temperatures, contributing to a high RRR.

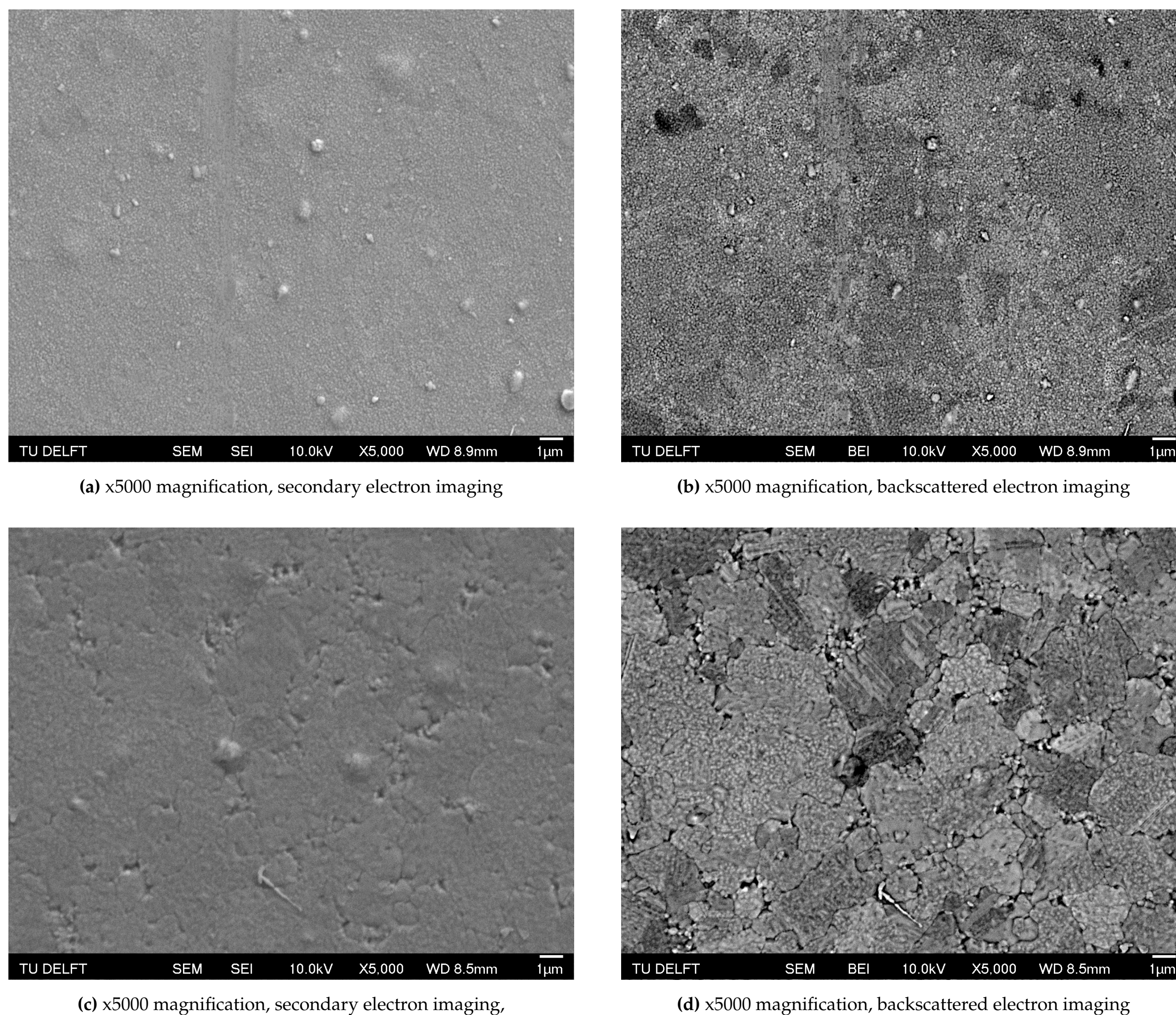

(a) x5000 magnification, secondary electron imaging

(b) x5000 magnification, backscattered electron imaging

(c) x5000 magnification, secondary electron imaging,

(d) x5000 magnification, backscattered electron imaging

Figure 4.4: SEM micrographs of: (a), (b) 2 μm thick NHT unlaminated film ; (c), (d) 2 μm thick HT unlaminated film (oven treatment)

Figure 4.3 also shows that NHT samples exhibited higher RRR when compared to HT samples after undergoing three, and four lamination runs, unlike the unlaminated samples. This difference can be attributed to the dewetting phenomenon, which is explained in more detail in Section 4.1.5 regarding the white surface finish observed after the oven heat treatment. Although the eye inspection did not reveal a white surface finish on the samples from the deposition run RRRS230801, it is likely that the oven heat treatment process induced the same phenomenon, given that the process was identical. As shown in Figure 4.16, the samples with white residuals exhibit open and porous microstructure with some visible detachments within the film. These structural anomalies are likely to hinder grain growth and contribute to high electrical resistivity at low temperatures. The lower RRR values of HT samples compared to NHT samples for three and four-times lamination cases can be attributed to these irregularities in the microstructure.

4.1.3. Comparison of oven heat treatment and lamination

In this section, we investigated the influence of different thermal treatments on the microstructural properties of thin silver films, subsequently impacting RRR. Both the oven and lamination processes, due to their inherent use of heat, induce the annealing phenomenon within the thin film silver substrate. To see the divergent effects of oven treatment and lamination, we conducted a comparative analysis

involving two distinct specimens: the heat-treated, unlaminated sample denominated as HT-L0, and their counterpart, the non-heat-treated, one-time laminated specimen identified as NHT-L1. Figure 4.3 shows that oven treatment increased the RRR mean from 16 to 38, which corresponds to an increase by a factor of ~ 2.5. On the other hand, the lamination process caused an even more remarkable increase in the RRR by a factor of ~ 3.3. This difference can be attributed to the different characteristics of thermal treatments in terms of the temperature, duration, pressure, cooling/heating rates, and ambient conditions of the processes. Table 4.1 summarizes the details of these two heat treatment methods.

	Lamination	**Oven**
Temperature	295 °C	180 °C
Duration	1h 20 min	5 h
Cooling/heating rate	slow	fast
Pressure	80 mbar	-
Ambiance	vacuum	air

Table 4.1: Details of lamination and oven heat teratments

A comparative examination of SEM images shown in Figure 4.5 reveals distinctions between two silver thin films, each processed through different heat treatment techniques. Figure 4.5a and Figure 4.5b, illustrating the laminator-treated film, exhibit a microstructure with low pore density. This observation is consistent with the film's high RRR value, indicative of low electrical resistivity at low temperatures and minimal electron scattering within the lattice. In contrast, Figure 4.5c and Figure 4.5d show a silver thin film subjected to oven heat treatment, characterized by a significantly porous surface. Notably, the film exhibits visible detachments within the microstructure. These structural anomalies correlate with a diminished RRR value. These microstructural differences are attributed to the variations in temperature, duration, pressure, cooling/heating rates, and ambient conditions during lamination and oven heat treatments (see chapter 3 and Table 4.1 for more details on the processes). In particular, the lamination process involves gradual heating and cooling, ensuring more controlled thermal transitions. On the other hand, the oven treatment subjects samples to abrupt temperature changes since samples were loaded only after reaching the final temperature and taken immediately after the designated time. This can induce microstructural stress in the thin film silver and hinder the complete grain growth, consequently leading to delaminations and pores in the microstructure. This comparative analysis emphasizes the important role of heat treatment methods in altering the microstructure of silver thin films. These findings align with existing literature that highlights the critical influence of annealing ambiance and temperature on the microstructure and, consequently, on the electrical properties of thin films [41, 42, 43].

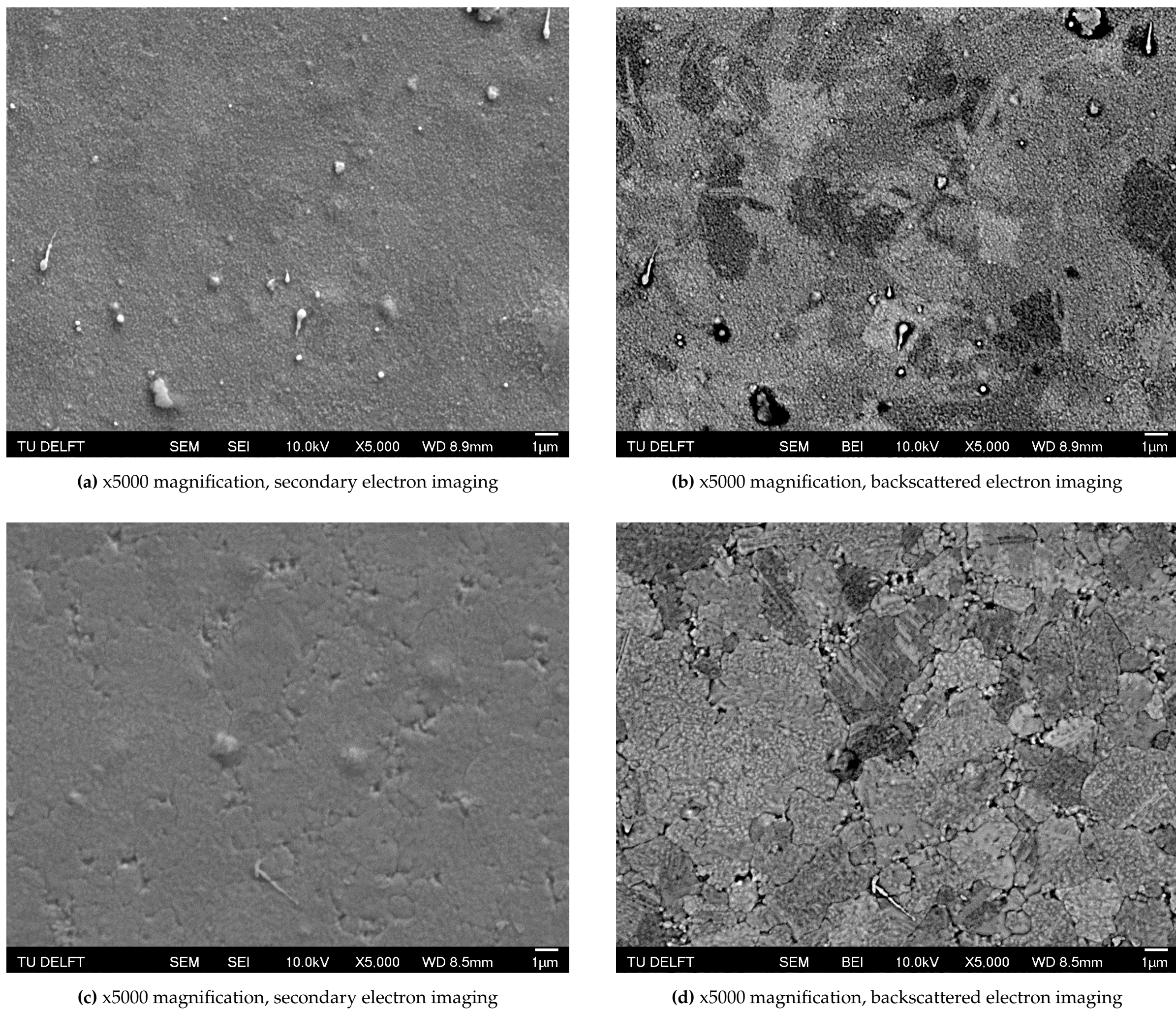

(a) x5000 magnification, secondary electron imaging

(b) x5000 magnification, backscattered electron imaging

(c) x5000 magnification, secondary electron imaging

(d) x5000 magnification, backscattered electron imaging

Figure 4.5: SEM micrographs of: (a), (b) 2 μm thick NHT one-time laminated film (lamination treatment) ; (c), (d) 2 μm thick HT unlaminated film (oven treatment)

4.1.4. Spread investigation

As can be seen in Figure 4.3 the error range for NHT-L1 and HT-L0 appears to be considerably large. When the RRR values were checked from Table A.1, it was observed that one of the HT-L0 and one of the NHT-L1 samples showed outlier RRR values compared to the other samples in their batches. In order to verify whether these outlier RRR values actually exist or were a result of an error during the cryogenic measurement, resistivity measurements and RRR calculations were repeated. The results of the second measurement were found nearly the same as the outlier RRR values from the first measurements. In this way, it was confirmed that outlier RRR values did not result from an error during the measurement. Following that, XRD analysis was performed in order to investigate the crystallographic structure and phase composition of the silver film that can possibly result in different electrical properties. Figure 4.6 presents a comparison of the XRD patterns of two HT unlaminated samples, which are called HT_L0_2 and HT_L0_5. The silver peaks were labeled on the figure and they were found to be rather sharp for both samples. However, no clear difference between the samples could be observed. XRD analysis showed that the crystallite size was found to be in the order of 50 nm for both samples.

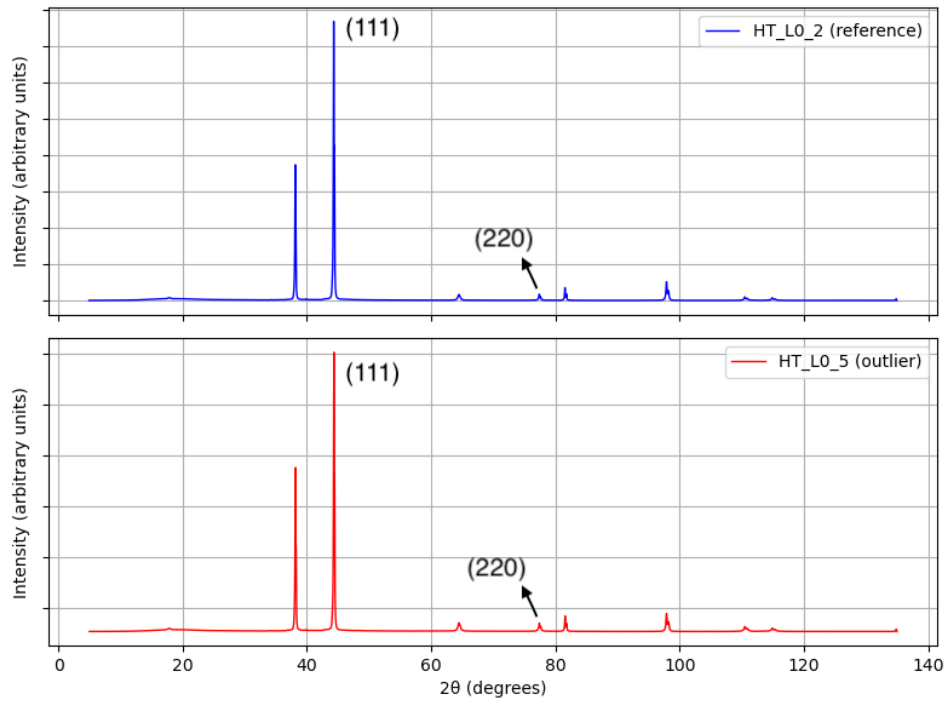

Figure 4.6: XRD patterns of two HT unlaminated samples

Similarly, the comparison of the outlier sample NHT_L1_5 to a reference from the batch of NHT one-time laminated samples is shown in Figure 4.7. Despite the efforts to observe a difference in the phase composition or the crystal structure of the samples, silver peaks were found to be the most dominant and sharp constituent for both samples. Hence, XRD results did not reveal any insights about the film that could potentially explain the difference in the RRR values.

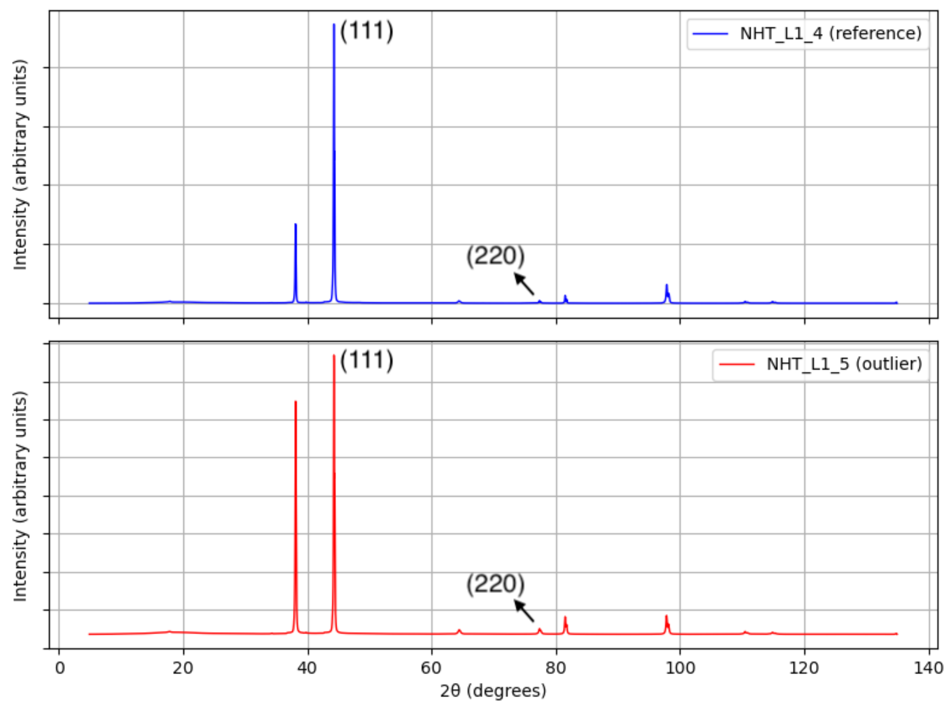

Figure 4.7: XRD patterns of two NHT one-time laminated samples

In addition to the outlier samples, NHT-L1 and HT-L0, which introduced significant variability into the dataset presented in Figure 4.3, a notable spread was also observed in the results obtained from three-times and four-times laminated HT samples. Table A.1 shows that the room temperature resistances of HT four-times laminated samples exhibited a variance of no more than 6% within the sample set. However, resistance values measured at the liquid helium temperature (4.2 K) displayed variations of up to 92% among samples within the same set. This disparity indicates that the primary source of data spread stemmed from the 4.2 K resistances. The subsequent section delves into an exploration of three theories that could potentially account for the fluctuations observed in the data from HT three and four-times laminated samples.

In order to explore the reason behind the sample-to-sample variation of the 4.2 K resistances, three different theories were investigated. Firstly, the time between the last lamination run and the resistance measurements was tracked to find whether the spread was caused by the aging effect. Secondly, the effect of encapsulation was examined since the encapsulation layer was added additionally to the surface of the silver film for the third and fourth lamination runs. Lastly, the encapsulation layer was baked to remove the dirt from the PI to find out whether uneven contamination of the encapsulation layer was the reason for the inconsistency in the data.

The effect of aging

The first approach to explain the fluctuations in the 4.2 K resistances was to explore the influence of the time passed after the last fabrication step (the last lamination run) until the measurement. A new set of samples was fabricated to be measured as soon as possible after their last lamination run. Figure 4.8 demonstrates a comparison of RRR values of three and four-times laminated samples which were measured within 15-20 days and 1-8 days after their fabrication. It should be noted that the samples labeled as 1-8 days represent the second set of samples specifically fabricated for this experiment set, while samples labeled as 15-20 days are taken from the fluctuating sample data of three and four-times laminated samples shown in Figure 4.3. RRR results of NHT and HT samples are displayed separately in Figure 4.8a and Figure 4.8b respectively.

In general, reducing the time after the fabrication until the measurement did not result in a conclusive positive effect in the spread of the data as can be seen in Figure 4.8. Figure 4.8a shows that sampling variation decreased for NHT four-times laminated samples when the time between the last lamination and measurement was lowered to 1-8 days from 15-20 days. On the other hand, it was found that reducing the time caused more spread for the NHT three-times laminated samples as observed in Figure 4.8a. Figure 4.8b reveals that the 1-8 days case had comparable fluctuation as the 15-20 days case showed earlier for three and four- times laminated samples. In light of the information obtained from this experiment, it can be said that the time passed after the fabrication until the measurement did not have a direct influence on the standard deviation of the data for HT samples. On the contrary, keeping the time between the fabrication and the measurement as short as possible reduced the spread in the data for NHT four-times laminated samples while it caused a larger standard deviation in the data for NHT three-times laminated samples.

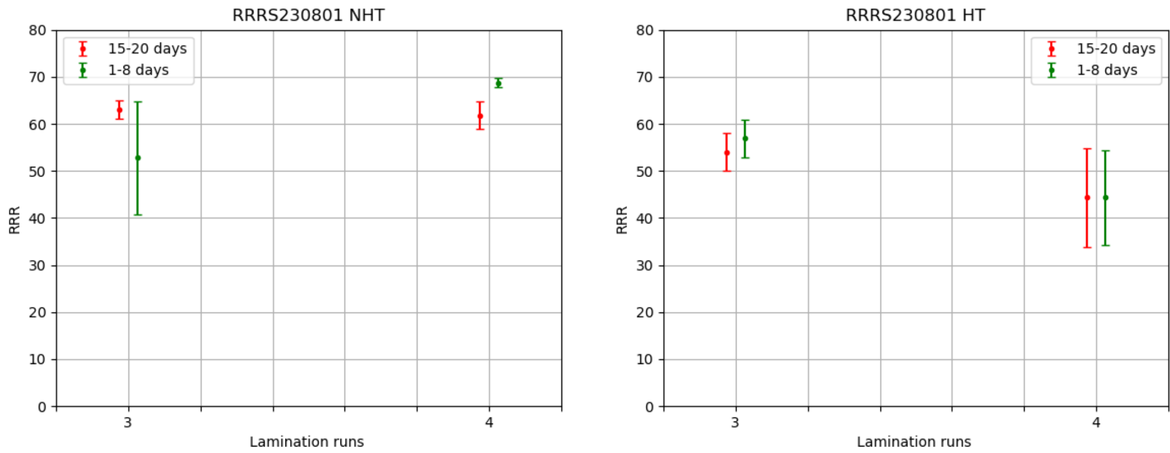

(a) RRR values of three and four-times laminated 2 μm NHT samples with 4N purity measured within 1-8 days and 15-20 days

(b) RRR values of three and four-times laminated 2 μm HT samples with purity 4N measured within 1-8 days and 15-20 days

Figure 4.8: A comparison of NHT and HT sample sets for the effect of time passed between the fabrication and measurement. All sets had six samples. Solid circles represent the mean value of the set.

The effect of encapsulation

Secondly, the effect of encapsulation was investigated by preparing and measuring unencapsulated samples. Figure 4.9 compares the RRR values of encapsulated and unencapsulated samples which were three and four times laminated. While NHT samples are shown in Figure 4.9a, Figure 4.9b displays the influence of encapsulation for HT samples. It is important to note that the sample data for encapsulated samples shown in Figure 4.9 were taken from Table A.1, while the unencapsulated samples were prepared later for the purpose of spread investigation. As can be seen in Figure 4.9a and Figure 4.9b, RRR values of the encapsulated and unencapsulated samples are very close to each other for the three-times lamination case. No encapsulation did not result in lower sample-to-sample variation necessarily for NHT samples. However, a notably lower spread was observed for HT four-times laminated samples shown in Figure 4.9b. The effect of encapsulation on the spread is not very clear for three-times laminated samples.

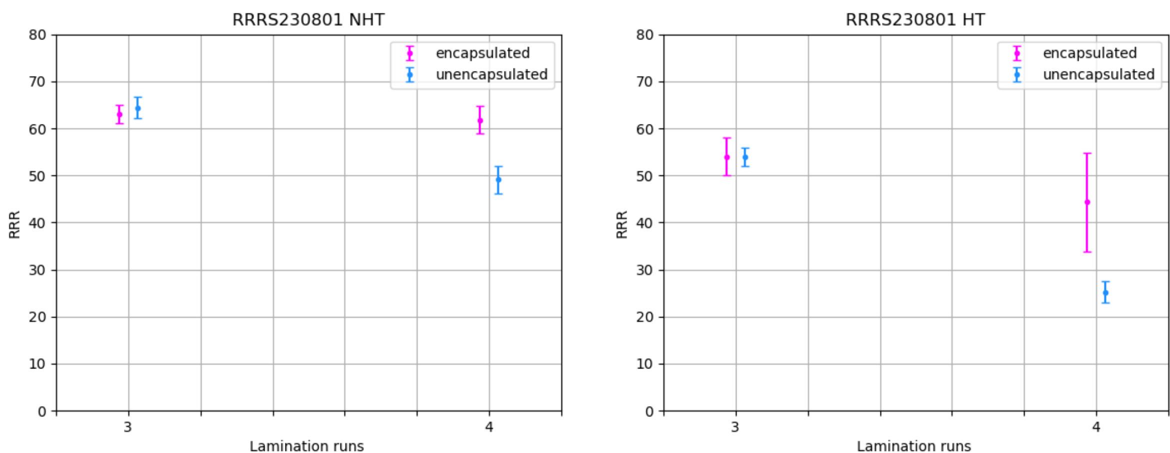

(a) RRR values of three and four-times laminated 2 μm NHT samples with 4N purity

(b) RRR values of three and four-times laminated 2 μm HT samples with 4N purity

Figure 4.9: A comparison of NHT and HT sample sets for the effect of encapsulation on the fluctuation in the data. Encapsulated sample sets had six samples, while the sample size of the unencapsulated samples was three. Solid circles represent the mean value of the set.

Before diving into conclusive statements for the effect of encapsulation, it should be pointed out that the sample size for unencapsulated samples was three, whereas encapsulated samples had a sample size of six for each lamination case. From the results obtained in Figure 4.9, it can be observed that in general RRR values of unencapsulated samples have a smaller variation. It looks like encapsulation helped reduce the fluctuation in the data. However, it should be borne in mind that this is a preliminary conclusion since sample sizes are not the same for both sets. To be more certain about the conclusion, this test should be repeated.

The effect of baking the encapsulation layer

Despite the fact that sample sizes were different, unencapsulated samples helped reduce the uncertainty of the data by lowering the sampling fluctuations for HT samples. As mentioned earlier, one of the explanations for the variation in the RRR results of the encapsulated samples can be uneven contamination of the encapsulation layer. Therefore, this experiment set was designed to explore whether removing the contaminants from the PI encapsulation layer by baking it out can provide consistency in the data.

Figure 4.10 compares the influence of the baking out process on the RRR values of NHT and HT sample sets which were both four-times laminated. It should be mentioned that the data of unbaked samples were taken from Table A.1 and the sample size was six. On the other hand, baked samples were fabricated later and contained 3 samples per each condition. It was observed in Figure 4.10 that baking the encapsulation layer did not help reduce the spread of the data for NHT samples, in fact, it caused a wider sample-to-sample variation. However, HT samples prepared by using the baked-out encapsulation layer resulted in a lower spread in their RRR data. These findings support the notion that the standard deviation of the NHT and HT samples was directly influenced by baking the encapsulation layer. However, the effect was not consistent between the two data sets. It still remains unclear why there was a sampling variation in the data.

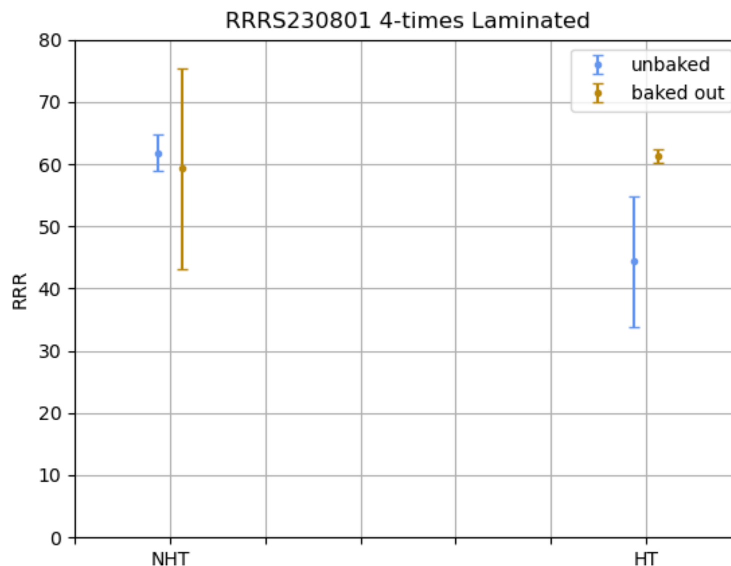

Figure 4.10: The effect of baked-out encapsulation layer on the RRR values of 2 μm thick four-times laminated HT and NHT samples with 4N purity. Unbaked sample sets had six samples, while the sample size of the baked samples was three. Solid circles represent the mean value of the set.

Other causes

Additional factors contributing to the fluctuation in the dataset encompass the measurement setup itself and the emergence of a white surface finish attributed to the oven heat treatment. The following section provides a more comprehensive examination of this white surface phenomenon, offering insights into its formation mechanisms and its consequential impact on the RRR of thin film silver.

4.1.5. White surface finish

Figure 4.11 shows two sets of unlaminated samples from different deposition runs. It aims to compare the variation among the samples that are expected to have the same characteristics. Silver film thickness was $2\mu m$ and the purity was 3N5 for both deposition runs. Therefore, Figure 4.11 provides a useful comparison to find out whether there is a variation between the deposition run that can affect the RRR results. Both deposition run consists of six NHT and six HT samples. The data for RRRS231907 samples were taken from Figure C.1, while RRRS231805 samples were prepared separately. As can be seen in Figure 4.11, identically fabricated NHT samples from two different depositions showed very similar RRR. Sample-to-sample variability was also found negligible for NHT samples. On the other hand, the average RRR of HT samples was found significantly different than each other. While the mean RRR of RRRS231805 samples was $\sim 21 \pm 7$, samples from the deposition run RRRS231907 showed RRR of $\sim 12.38 \pm 0.16$ on average. The fluctuation in the data of RRRS231805 HT samples was remarkably high compared to other sets.

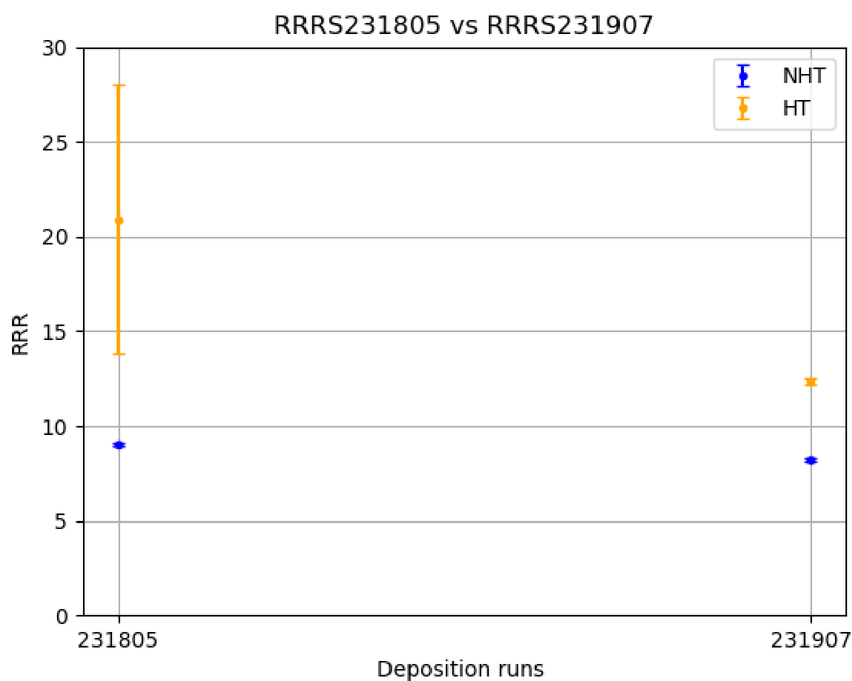

Figure 4.11: A comparison of two sample sets from different deposition runs with silver purity = 3N5 and film thickness = 2 μm. All sets had six samples. Solid circles represent the mean value of the set.

In order to explore further the reason for the spread of the data, Figure 4.11 was plotted as a scatter graph instead of an error graph. In this way, we can observe RRR results for every single sample. Figure 4.12 shows the RRR results of RRRS231805 and RRRS231907 samples. It can be observed that three HT samples were populated around RRR of ~ 27. However, RRR of the rest of the HT samples spread from 12 to 19. After the heat treatment process in the oven, white residuals were observed on half of the film as shown on the left side of Figure 4.12. Since this was an extraordinary finding, RRR

results of those samples were tracked to find out whether this white appearance on the surface can affect the RRR. Indeed, RRR of the samples taken from the white side (right) of the film was found lower compared to the RRR of the samples from the shiny side (left). The relation between the RRR results and the location of the samples was shown in Figure 4.12 with the arrows.

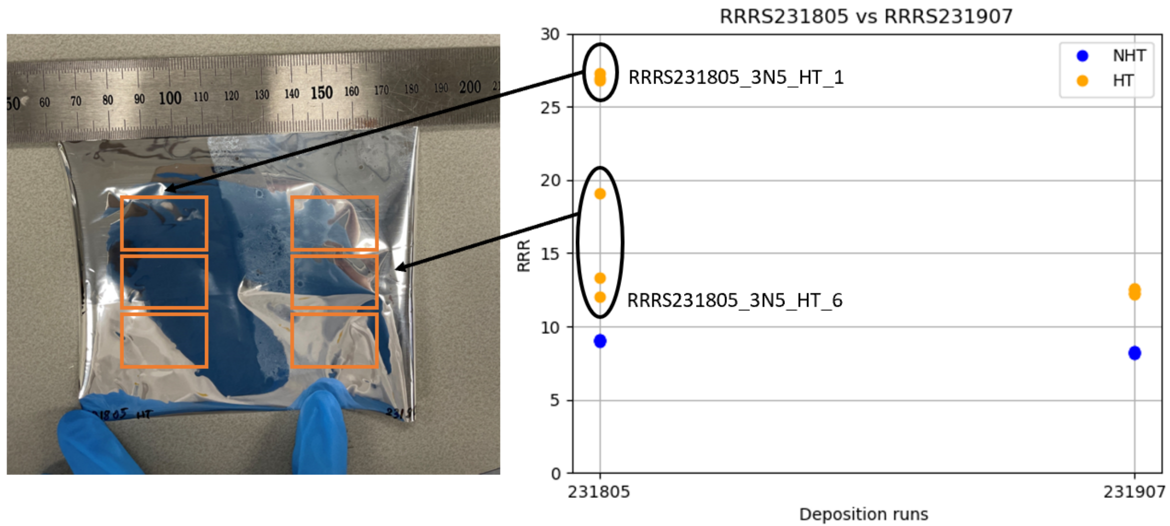

Figure 4.12: The illustration of sample locations on the silver film to investigate the spread in the data for two sample sets from different deposition runs with silver purity = 3N5 and film thickness = 2 μm. All sets had six samples. Solid circles represent the mean value of the set.

In the context of this study, silver nitrate ($AgNO_3$) was considered a likely chemical compound to form on silver thin films due to its white appearance [58]. To confirm this theory, a silver thin film sample with a white surface finish was immersed in water and left for 24 hours since it is soluble in water at room temperature [59]. However, no observable change was detected in the white residue. Therefore, it can be concluded that the chemical compound responsible for the white surface finish does not appear to be $AgNO_3$.

Further investigation was done with XRD analysis to detect additional phases of the silver that can potentially result in a white surface finish and different electrical properties. Hence, two samples each from different regions of the silver film were analyzed and their diffractographs are shown in Figure 4.13. Figure 4.13 revealed that there was no additional composition or phase encountered in the samples that have different surface looks. Therefore, SEM was used for further investigation to see if the microstructures of those samples can be distinguished from each other.

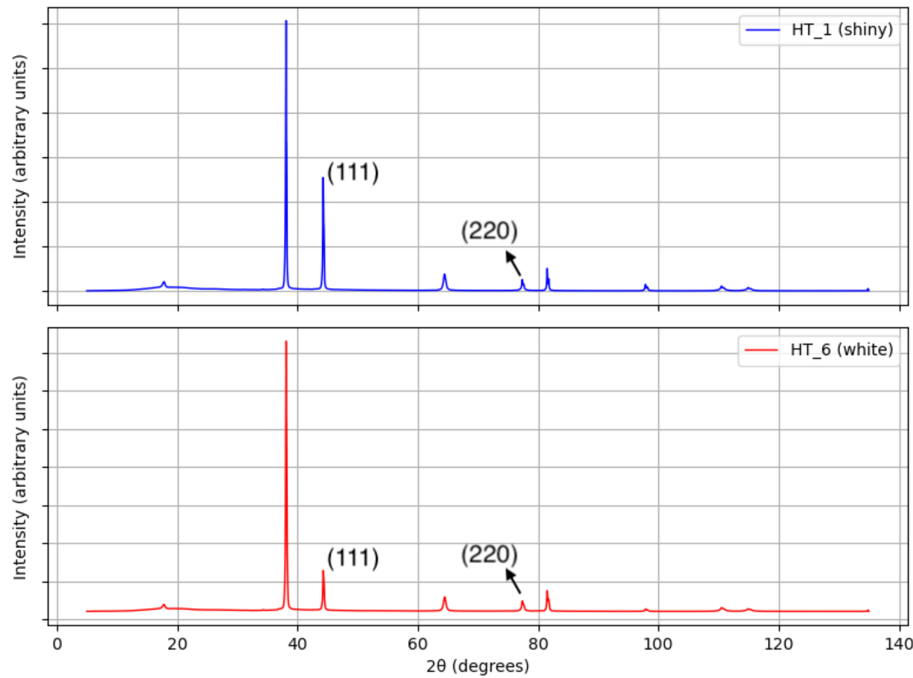

Figure 4.13: XRD patterns of two HT unlaminated samples; one is from the shiny region of the film with high RRR (HT_1) and the other one is from the white surface finished with low RRR (HT_6)

SEM images of two samples from the deposition run RRRS231805 are displayed in Figure 4.14. Figure 4.14a shows the microstructure of the sample called HT_1 (high RRR) from the shiny part of the film and Figure 4.14b shows the SEM picture of the sample called HT_6 (low RRR) from the stained part. The main difference observed between these two micrographs was the grain structure. The sample from the shiny part of the film revealed a denser microstructure while the silver film with the white residual showed a more open and porous microstructure. This porous structure can cause an increased amount of electron scattering and lead to poor conductance at 4.2 K. Therefore, low RRR values of the samples can be attributed to the microstructural modifications done on the silver film by these white residuals after the oven heat treatment.

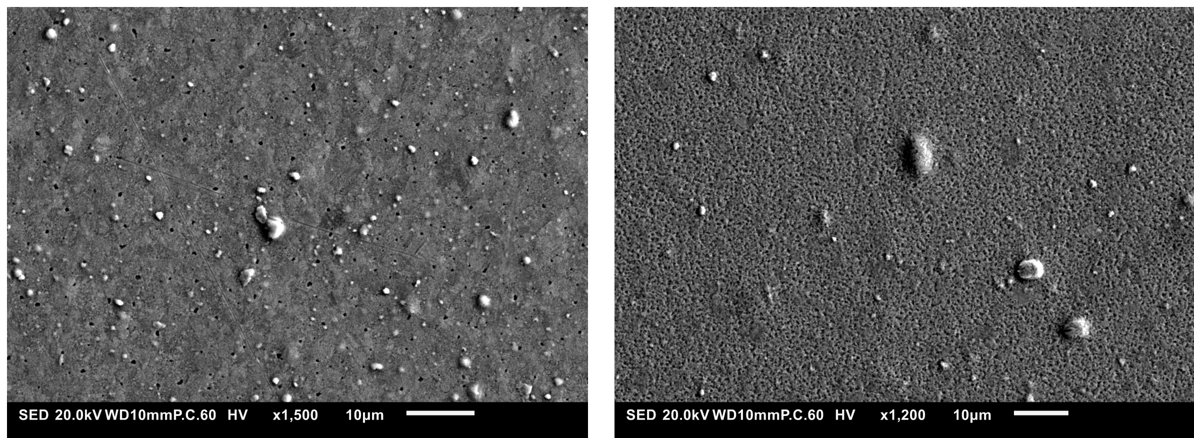

(a) SEM micrograph of the sample HT_1 with shiny surface finish (x1500 magnification, secondary electron imaging)

(b) SEM micrograph of the sample HT_6 with white surface finish (x1200 magnification, secondary electron imaging)

Figure 4.14: A comparison of SEM micrographs of RRRS231805 samples with silver purity = 3N5 and film thickness = 2 μm

Furthermore, Energy Dispersive Spectroscopy (EDS) analysis was performed to examine whether there is a difference in the chemical elemental compositions of the samples HT_1 (high RRR) and HT_6 (low RRR). Figure 4.15a and Figure 4.15b display the elemental spectra for the samples HT_1 and HT_6,

respectively. Numerical elemental identifications in terms of mass and atom were also given in Table 4.2. It was found that both samples consisted of mainly silver and they contained a trace amount of carbon (C) and aluminum (Al). In general, there was no significant difference observed in the EDS analysis of these samples in terms of different chemical compositions. However, EDS analysis provided insights into the contamination of the silver thin film during the fabrication process. As given in Table 4.2, the silver mass percentage was measured at 98.71 % and 99.07 % on the samples previously reported to have a purity of 99.95% (3N5). Even though the accuracy of the two measurements may not have been identical, the fabrication steps of the cable cable-making process are likely to introduce contaminants to the silver thin film.

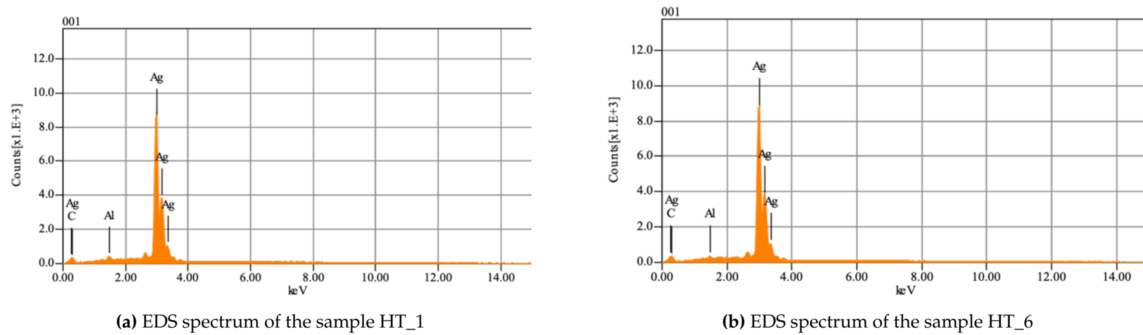

(a) EDS spectrum of the sample HT_1

(b) EDS spectrum of the sample HT_6

Figure 4.15: A comparison of EDS spectra of RRRS231805 samples with silver purity = 3N5 and film thickness = 2 μm

	HT_1					HT_6				
Formula	**Mass %**	**Atom %**	**Sigma**	**K ratio**	**Line**	**Mass %**	**Atom %**	**Sigma**	**K ratio**	**Line**
C	0.57	4.82	0.00	0.0009237	K	0.47	3.99	0.00	0.0007641	K
Al	0.72	2.70	0.03	0.0026472	K	0.46	1.74	0.03	0.0016720	K
Ag	98.71	92.48	0.21	0.4622742	L	99.07	94.27	0.21	0.4623417	L
Total	100.00	100.00				100.00	100.00			

Table 4.2: A comparison of elemental analysis of RRRS231805 samples with silver purity = 3N5 and film thickness = 2 μm

Overall, XRD and SEM/EDS analysis revealed that the white appearance on the surface of the silver film did not result from the formation of new phases. In fact, the modifications in the grain structure towards a more porous and open microstructure led to a white look on the surface. In order to investigate whether this porous structure can be explained by dewetting, a cross-sectional analysis was planned. Despite the efforts to make a sharp cut on the sample, it was not possible to obtain a clean cut to be able to observe the cross-section due to the lack of lab equipment such as a focused ion beam machine. Moreover, liquid nitrogen (N) was also used to obtain a brittle cut. However, it was challenging to have a clean breaking line since PI is an extremely flexible material. The liquid N temperature (77 K) was not low enough to bring PI to its brittle state.

In addition to 2 μm thick film, a white surface finish was also observed in 0.25 μm film whose RRR results were given in Table A.4. The spread in the data of NHT samples was found negligible. However, HT samples showed a large spread in the data. It can be seen that 0.25 μm thick HT samples consist of two sets: one set of shiny silver and one set with white residual. Table A.4 reveals that the samples with white residuals resulted in lower RRR compared to shiny samples in accordance with the previous findings.

Figure 4.16 shows the microstructures of two silver thin films: one with a shiny surface finish showing a high RRR value and the other with a white surface finish showing a lower RRR. Figure 4.16a and Figure 4.16b, characterized by a high RRR value, unveils a remarkably smooth surface with grains of nearly identical size distributed uniformly. On the contrary, Figure 4.16c and Figure 4.16d, representing a silver thin film with a lower RRR value, present a textured morphology caused by detachments within the film. It can be observed that this results in a considerably rougher and porous surface. These detachments suggest potential defects or impurities in the material, impacting its electrical

conductivity negatively. This comparison highlights the critical role of RRR giving insights from the microstructural properties of silver thin films, with higher values yielding more refined and uniform grain structures, while lower values can lead to structural imperfections with consequential effects on material performance.

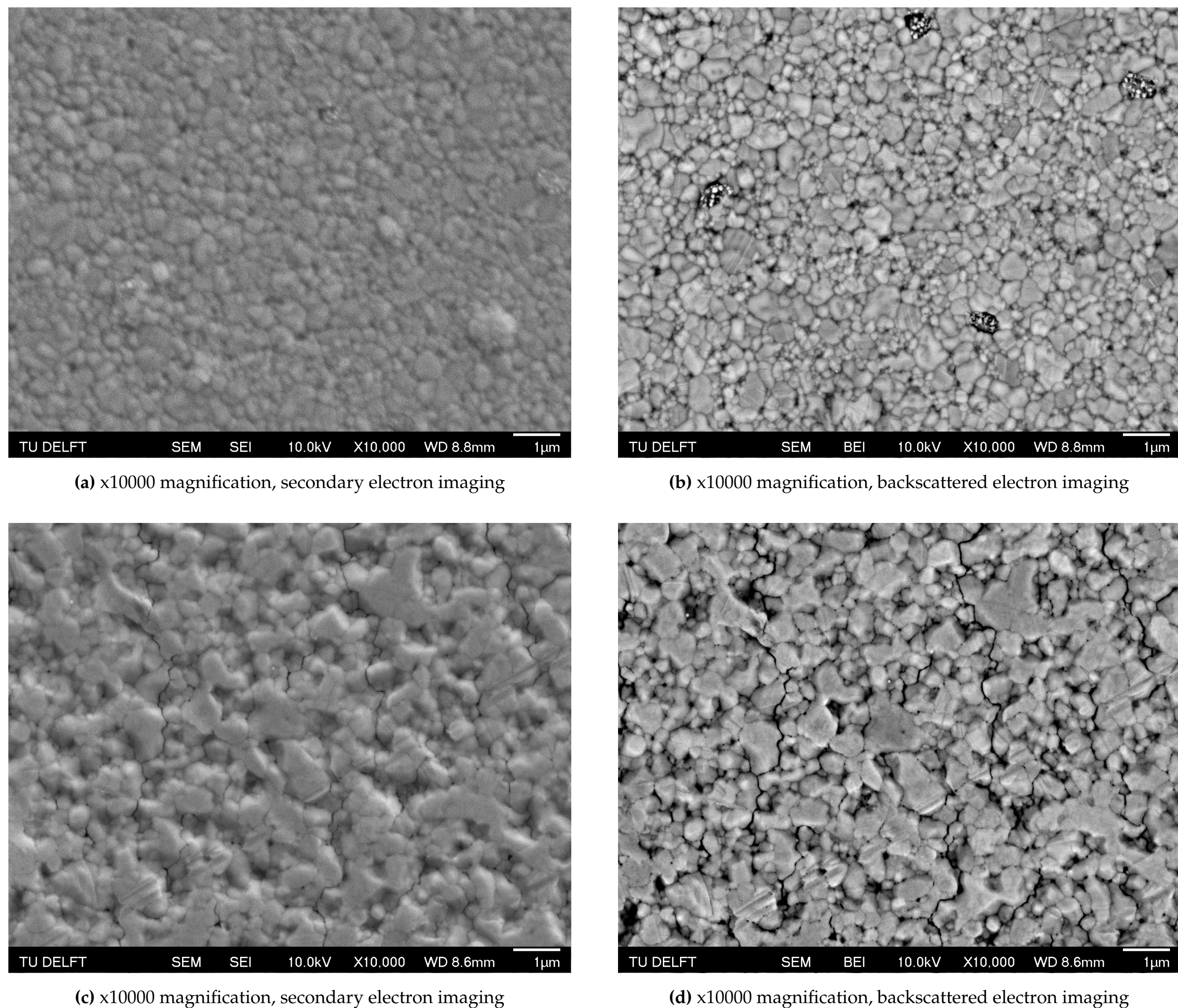

(a) x10000 magnification, secondary electron imaging

(b) x10000 magnification, backscattered electron imaging

(c) x10000 magnification, secondary electron imaging

(d) x10000 magnification, backscattered electron imaging

Figure 4.16: SEM micrographs of: (a), (b) 0.25 μm thick HT unlaminated film with shiny surface finish; (c), (d) 0.25 μm thick HT unlaminated film with white surface finish

The presence of rough and porous microstructures, as shown in Figure 4.16c and Figure 4.16d, can be attributed to the dewetting phenomenon. Dewetting is characterized by the agglomeration and formation of distinct islands on the surface of thin films when subjected to elevated temperatures [60]. The driving force of this process is surface energy minimization [61]. It is observed in Figure 4.16c and Figure 4.16d that the film surface morphology consists of these agglomerates rather than a continuous structure as a result of the oven heat treatment process. This phenomenon on the thin film silver was studied by Jacquet et al. and their findings revealed that 40 nm thick silver film on silica experienced dewetting with sufficiently high temperature (330 °C) and the extent of agglomeration increases with longer heat treatment durations [62]. It is important to note a significant difference in the silver film thicknesses between our study (0.25 μm) and the study by Jacquet et al. (40 nm) [62], which can lead to variations in the degree of agglomeration in terms of the particle size and the spacing between the adjacent particles. The characteristics of dewetting can be tailored through the control of the temperature, duration and as-deposited metal film thickness [63]. In our study, this phenomenon was beneficial since it led to a decrease in the mean RRR of thin film silver. However, it can still be further improved by optimizing the parameters mentioned above to obtain desired thin film properties, in particular electrical and thermal conductance at low temperatures.

4.2. Silver Purity

The effect of purity on the thin-film silver RRR was investigated by comparing different silver batches. The same fabrication procedure was followed as shown in Figure 3.3.

Figure 4.17 presents a comparison of RRR results of samples prepared with different purities namely 4N and 3N5 by combining Figure 4.3 and Figure C.1. The thickness of the silver film is 2 μm for both sample sets. The RRR mean of HT unlaminated samples with low purity (3N5) was found around 12. The first lamination led to an increase in the average RRR of low purity (3N5) samples from 12 to 22 by a factor of $\sim$ 2. As can be observed in Figure 4.17, the three-time and four-time laminated samples showed very similar RRR values to the one-time lamination case with a slightly higher RRR average. Overall, RRR values of samples with low purity (3N5) were found to be saturated after the first lamination run. The general RRR trend of 3N5 was similar to higher-purity silver (4N) thin-film samples as shown in Figure 4.17 (also presented earlier in Figure 4.3) in terms of the saturation achieved after the first lamination run.

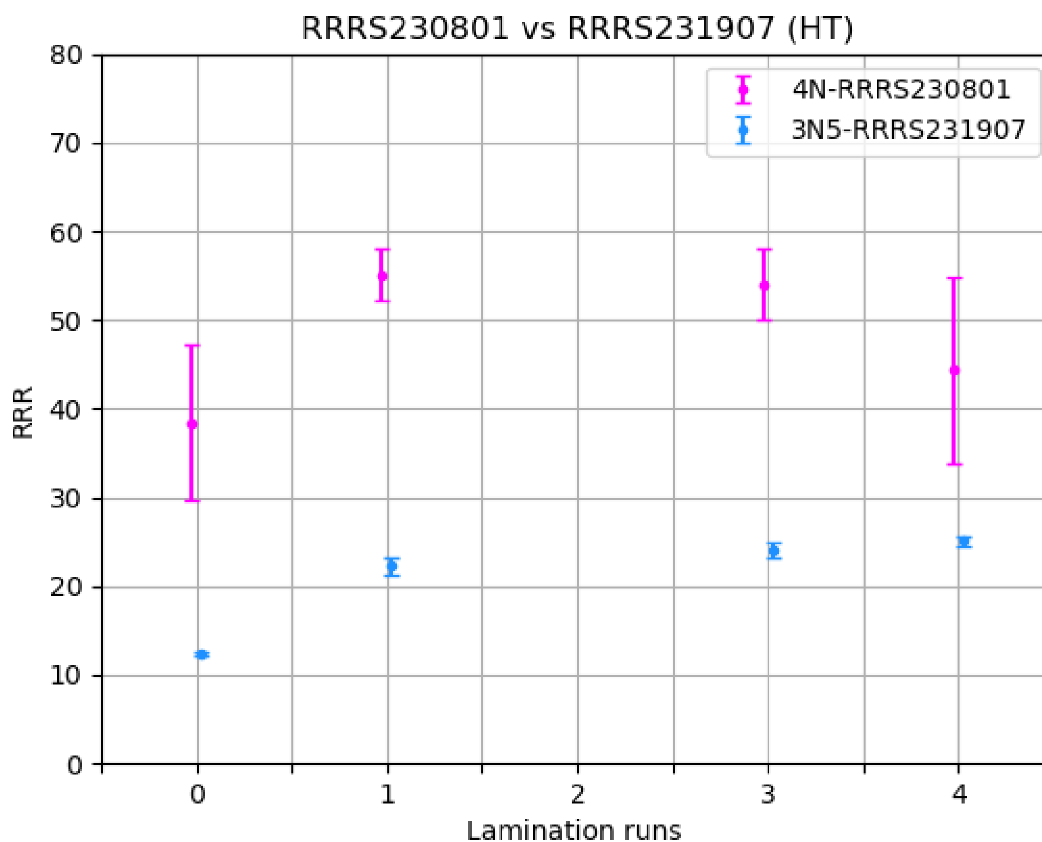

Figure 4.17: The influence of different silver purities on the RRR behavior of 2 μm thick HT samples with purities 4N and 3N5. All sets had six samples. Solid circles represent the mean value of the set.

It can be seen in Figure 4.17 that the standard deviation of the data is remarkably less for RRRS231907 compared to RRRS230801. Two theories were developed to explain this difference. Firstly, higher-purity silver is potentially more open to contamination since it is energetically more favorable to accommodate impurity atoms [38]. The contamination can not be controlled, therefore it is highly possible that it occurred heterogeneously either before the evaporation due to the storage conditions of the silver batch or after due to the handling of samples during measurements. This uncontrolled and heterogeneous contamination might increase sample-to-sample variability. Secondly, sample set RRRS231907 was prepared and measured later than RRRS230801 timewise throughout the project. Although there was

not any major change in the sample fabrication or measurement setup, there might have been some improvements that could potentially reduce the spread of the data.

Figure 4.17 also revealed that samples prepared with lower-purity silver resulted in significantly lower RRR values compared to the higher-purity sample set. In order to observe whether the difference comes from the low-temperature resistances or room-temperature resistances, resistance values at these temperatures were analyzed for both sample sets with different purity levels. Table A.1 and Table A.2 show the critical details of the samples and measurements that led to RRR values of samples with purities 4N and 3N5, respectively. It can be observed that room temperature resistances were measured within the range of 7.5-9.5 Ω for both sample sets. Furthermore, there was not any characteristic resistance trend discovered as a result of the changing heat treatment processes or lamination runs. In other words, resistances measured at room temperature were found to be independent of the purity, heat treatment, or number of lamination runs. This finding is in good alignment with the theory that was elaborated in Section 2.4. As demonstrated in Figure 3.11, the electrical resistivities of samples with different purity levels become the same at high temperatures. The reason for such an electrical resistivity curve is the fact that the lattice vibrations mechanism takes over once the temperature increases to room temperature [14]. Since all of the samples are silver, they have the same crystal lattice which results in similar electrical resistance values.

Room temperature resistances were found to be the negligible factor to cause the difference in RRR values, therefore liquid He temperature resistances were analyzed as the second step. Table A.1 and Table A.2 show that the resistances of 4N and 3N5 purity samples measured 4.2 K were dramatically different from each other for the same lamination case. HT one-time laminated samples can be given as an example. While the average of liquid He resistances of 4N purity samples were found to be ~ 0.14 Ω, the low-temperature resistance of 3N5 purity samples was measured ~ 0.36 Ω (see Table A.1 and Table A.2). Overall, 4.2 K resistances of low-purity samples were found to be consistently higher than high-purity samples. As shown in Equation 2.3, RRR is inversely proportional to 4.2 K resistance. Therefore, lower RRR values shown in Figure 4.17 for 3N5 purity samples compared to 4N purity samples can be attributed to the higher resistances measured at 4.2 K for low-purity sample. These findings of Figure 4.17 correspond to the theory presented in Section 2.4 such that low-temperature resistivity is determined by the crystal lattice imperfections [14].

Overall, lowering the purity level of the material led to a decrease in the RRR values due to an abrupt increase in the resistances measured at liquid He temperature. As mentioned in Section 2.4, impurities act like scattering spots against electrical conductance and impurity scattering becomes the dominant factor determining the resistivity of metals once the lattice vibrations diminish at low temperatures [50]. Mimura et al. [52] also observed that RRR of higher-purity copper (Cu) samples was higher compared to lower-purity copper samples. It is important to note that copper and silver are similar in terms of physical, electrical and chemical properties as they both are listed in group 11 of the periodic table. Therefore, they were assumed to be comparable.

Figure 4.18 summarizes the overall RRR trend of 2 μm thick HT unlaminated samples with changing silver purity. RRR values constantly increase with increasing silver purity. The findings of this study revealed that RRR of silver can be controlled and modified by changing the impurity level present in the material. This offers a great potential to tune the RRR of silver thin film used in cryogenic flexible cabling. Given the fact that thermal load is one of the biggest challenges of quantum computer wiring, the impurity level can be increased to achieve lower RRR and consequently lower heat load.

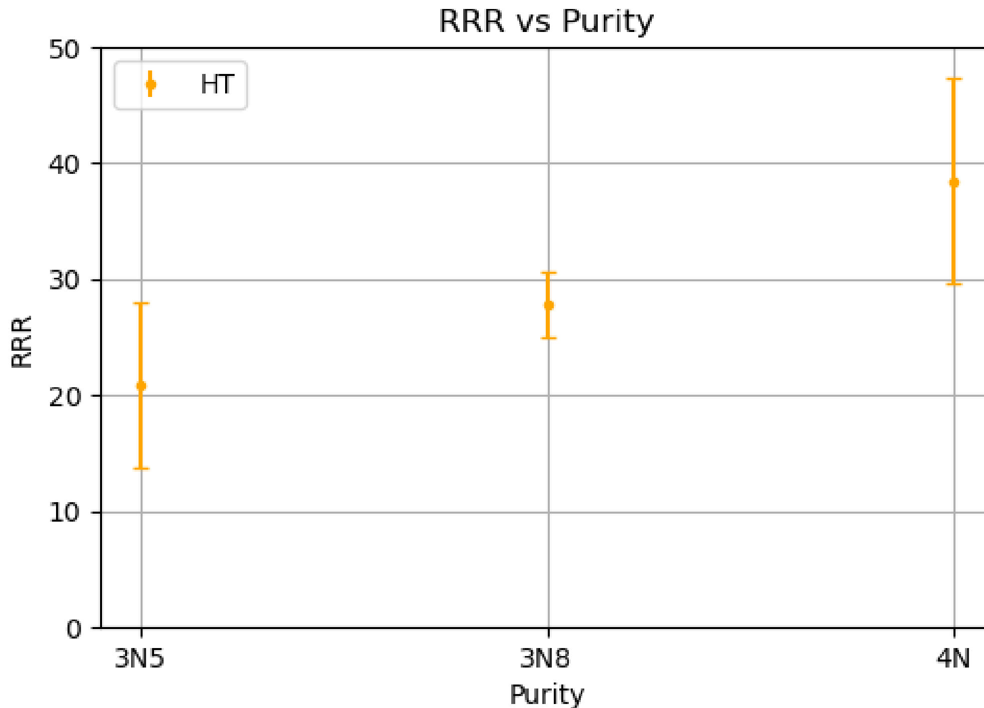

Figure 4.18: The behavior of RRR of the unlaminated and 2 μm samples with respect to silver purity. The corresponding deposition runs for the samples with 3N5, 3N8 and 4N purities are as follows: RRRS231805, RRRS232202, and RRRS230801, respectively. All sets had six samples. Solid circles represent the mean value of the set.

4.3. Film Thickness

This section examines the influence of film thickness on the silver RRR. In the previous sections, the film thickness was chosen 2 μm as in the real fabrication process. In order to compare the effect of film thickness on the RRR, 0.25 μm and 1 μm thick samples were prepared in addition to 2 μm samples. It should be borne in mind that it was not possible to use the same silver batch as used for the 2 μm thick samples from the deposition runs 230801 and 231907 presented in the previous sections. Therefore, the effect of the silver batch as well as the variation due to different deposition runs should be also considered for the comparison of RRR values. The sample size for each lamination case was six. Due to the low thickness of the silver films, laser patterning failed for some samples. Therefore, some of the sample groups contain a fewer number of samples. One can refer to Appendix A in order to see the sample size for each case as well as the details of the samples and measurements on the sample level.

Figure 4.19 presents a comparison of RRR results of HT samples with different film thicknesses: the sample set RRRS232301 has 0.25 μm thickness and the sample set RRRS232702 consists of 1 μm thick silver film samples. RRR values of unlaminated 0.25 μm thick HT samples were found $\sim$ 5.5. After the first lamination run, a minor increase was observed in the RRR of HT samples from $\sim$ 5.5 to $\sim$ 6.5. The third and fourth lamination runs did not result in a major change in the RRR of 0.25 μm thick HT samples. As can be seen in Figure 4.19, the RRR trend was found rather stable after the first lamination run.

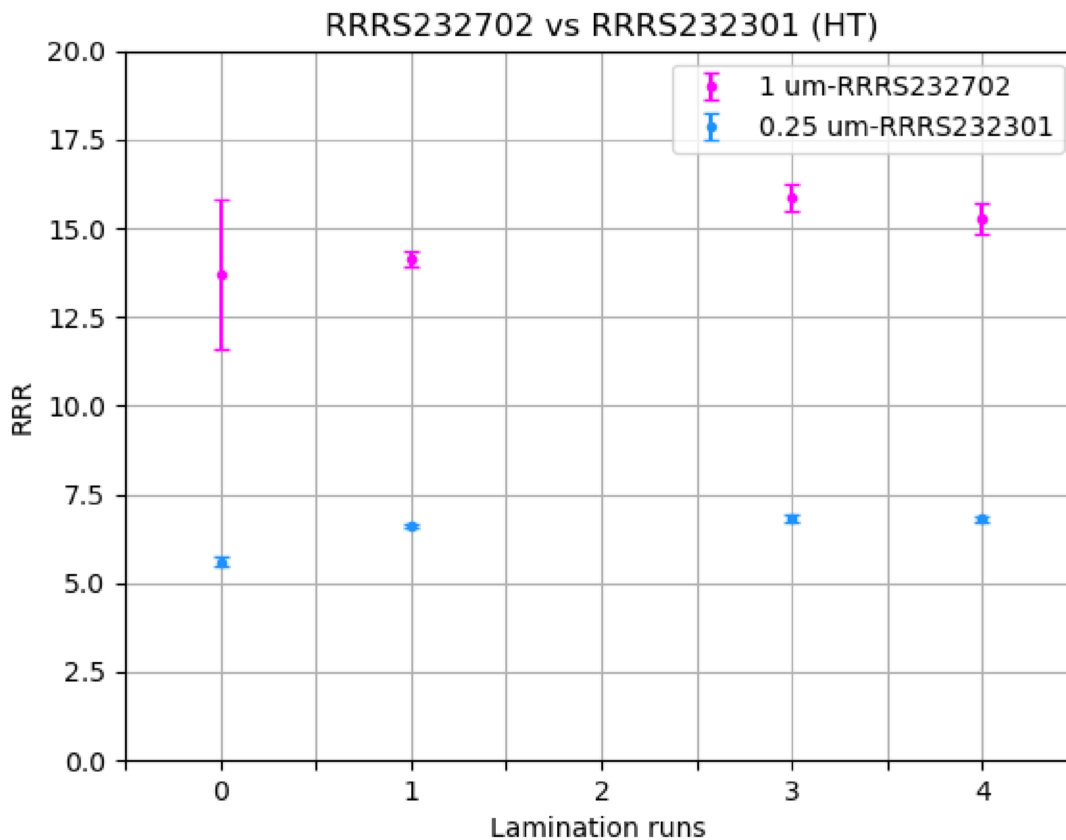

Figure 4.19: The influence of silver film thickness on the RRR behavior HT samples with 3N8 purity. All sets had six samples. Solid circles represent the mean value of the set.

RRR mean of unlaminated HT samples with 1 μm thickness was found to be 14 ±2. As a result of the first lamination run, the average RRR of HT 1 μm thick samples slightly increased. There was not any remarkable change observed in the RRR trend after the third and fourth lamination runs of HT samples. As can be seen in Figure 4.19, the RRR trend was found saturated after the first lamination run. Additionally, the fluctuation within the sample set RRRS232702 was unimportant except for the unlaminated HT samples with 1 μm thickness. The fluctuation observed in the unlaminated sample set was caused by the samples that contained white stains (see Table A.6).

Figure 4.20 shows the RRR behavior of unlaminated HT samples with respect to film thicknesses of 0.25 μm, 1 μm and 2 μm. The deposition run of 0.25 μm and 2 μm thick samples is called RRRS232202, while 1 μm samples are from the deposition run RRRS232702. It should be noted that even though they are from different deposition runs, the silver batch was the same for all sets. The silver purity was 99.98 % (3N8). The average RRR values of 0.25 μm, 1 μm and 2 μm thick HT samples were found to be 5.6 ±0.1), 13.7 ±2.1 and 27.8 ±2.8 respectively. As can be seen in Figure 4.20, RRR results can fit into a linear relation. A similar relationship was found for one-time, three-times and four-times laminated samples and presented in Appendix B.

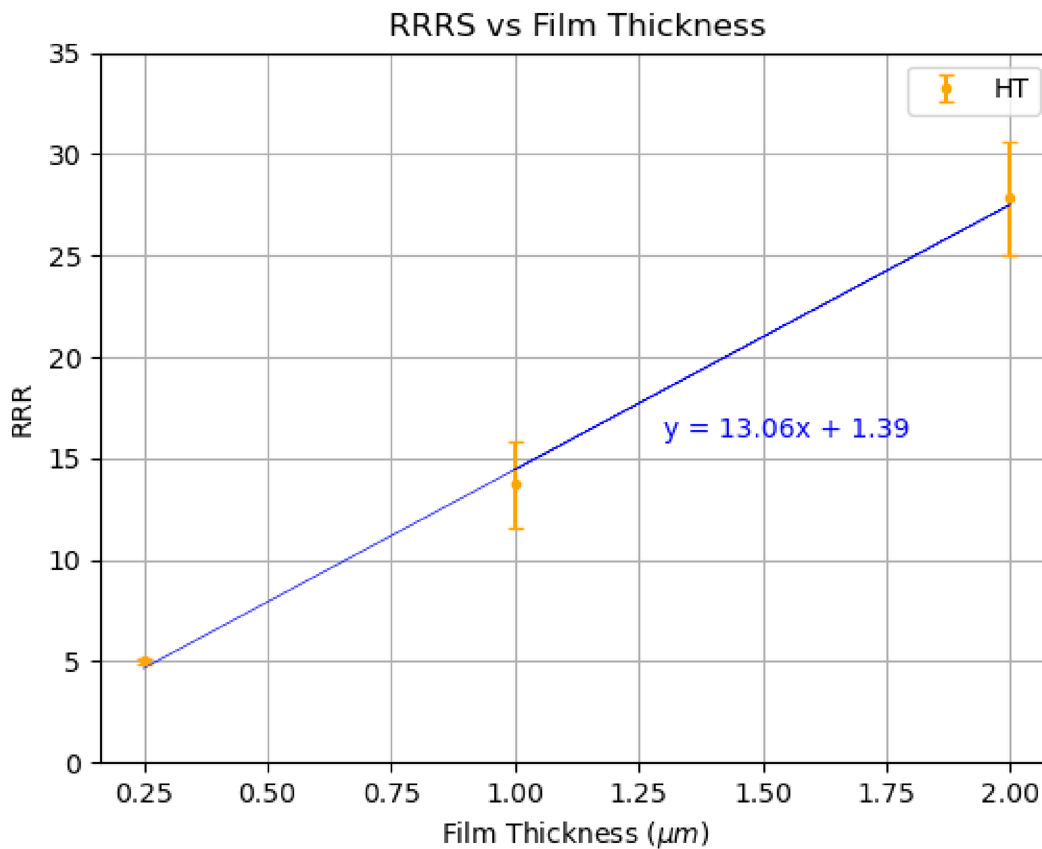

Figure 4.20: The behavior of RRR of the unlaminated HT samples with respect to film thickness. The purity of the silver is 3N8 . All sets had six samples. Solid circles represent the mean value of the set.

Overall, Figure 4.20 revealed that thinner silver films led to lower RRR values. Similar findings were also presented by Singer et al. [39] for a copper film. They observed that RRR of the copper film increased dramatically with increasing film thickness [39]. This can be attributed to the different properties of interfaces compared to the interior of the materials [25]. They can introduce additional scattering sites for conduction electrons and consequently, result in higher electrical resistivity at low temperatures.

As shown in Figure 4.20, the sample-to-sample variation of 0.25 μm thick HT samples was found negligibly small. On the other hand, a remarkably wide error was observed for 1 μm and 2 μm thick HT samples. This can be attributed to the white stains on some regions of the film surface. Table A.6 and Table A.4 give the details of samples that were found to have a white appearance in the eye inspection. It can be seen that the white stain-containing samples resulted in lower RRR values which caused a relatively wider error bar in Figure 4.20. These findings are in alignment with the previous results of the stained samples showing lower RRR as explained earlier.

4.4. Aging and Storage

In this section, the impact of aging and storage conditions on the RRR of silver thin film was studied. Figure 4.21 presents the results of RRR measurements done on the samples from the deposition run RRRS231907. The data labeled as reference represents the samples that are tabulated in Table A.2 and were measured within 12 days after the fabrication. Following the first cryogenic measurements, we

divided the samples into two groups. One group was stored in a controlled dry environment at 33 °C with a humidity level of 7.6 % for a duration of 77 days, while the other group remained under ambient room conditions for a span of 75 days. As shown in Figure 4.21, our findings reveal that neither the passage of time nor the difference in storage conditions yielded a significant change in the RRR values of the HT thin film silver samples.

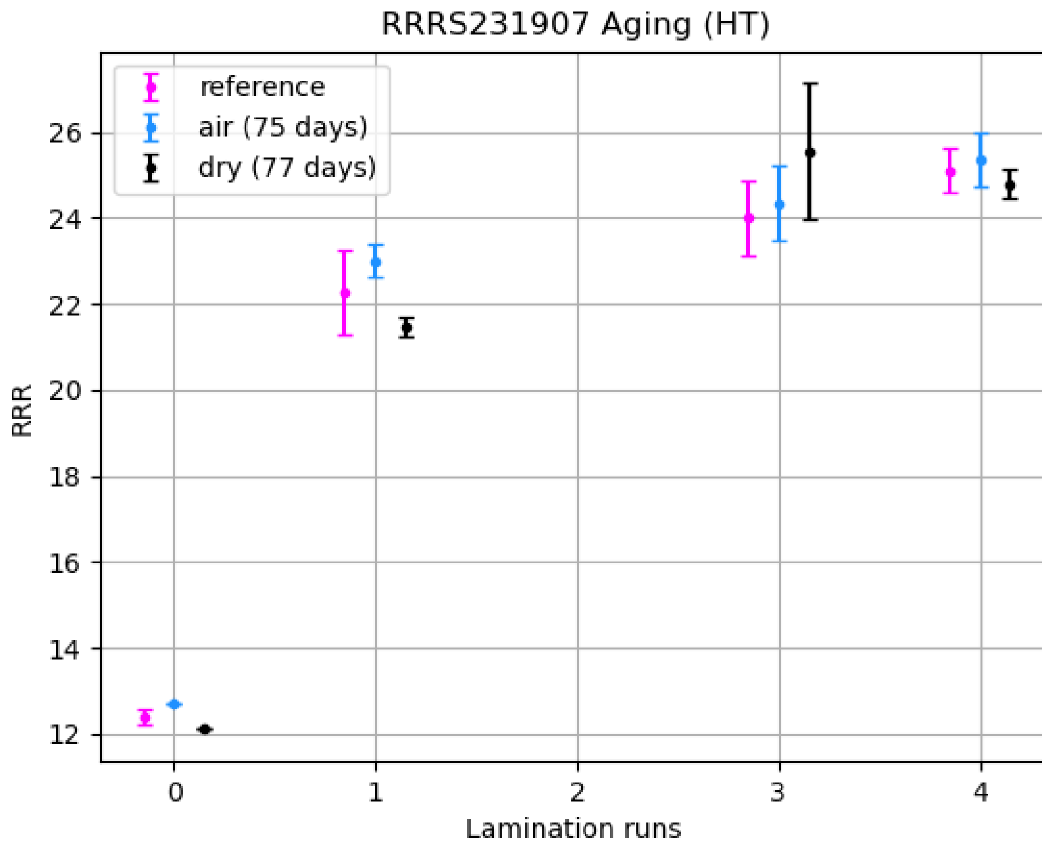

Figure 4.21: The effect of aging and storage conditions on the RRR behavior of HT samples with respect to the increasing lamination run from none to four. The silver purity is 3N5 and the film thickness is 2 μm. Reference samples are measured no more than 12 days after the fabrication (see Table A.2) and had six samples for each set, while sample sets of air and dry storage were measured after 75 days and 77 days, respectively and had three samples unless there was an error during the measurements. Solid circles represent the mean value of the set.

5 Conclusions and Recommendations

5.1. Conclusions

This thesis explored how fabrication conditions affect the electrical and thermal properties of low-temperature silver thin films, using the Residual Resistivity Ratio (RRR) to evaluate thermal load in cryogenic flexible cables with silver-deposited Polyimide films. We investigated various fabrication parameters, including heat treatment methods (oven and lamination), silver purity, film thickness, aging, and storage. Samples replicated Delft Circuits' cable design and production process and underwent RRR measurements alongside microstructural, crystallographic, and compositional analyses through SEM and XRD.

The findings revealed that both heat treatment techniques resulted in increased RRR values for the samples. This was attributed to the grain enlargement by the heat treatment, leading to lower grain boundary density, and consequently, reduced electrical resistivity at low temperatures. Notably, the samples subjected only to oven heat treatment showed significantly lower RRR values compared to those subjected only to lamination heat treatment. This difference was attributed to the distinct nature of these heat treatment techniques in terms of temperature, duration, pressure, ambiance, heating, and cooling rates. Some of the oven heat-treated samples displayed a distinctive white surface finish which is likely explained by the dewetting phenomenon. This phenomenon resulted in a porous microstructure with random grain size, and consequently, lower RRR compared to the shiny region of the silver film. The lower RRR values of heat-treated samples when compared to non-heat-treated samples for three and four times lamination cases were highly likely to result from this phenomenon.

Furthermore, the results of this study clearly indicated that the purity level directly influenced the RRR behavior of silver thin films. RRR tended to decrease with lower purity levels due to increased electron scattering at low temperatures caused by impurities within the lattice. Moreover, a linear relationship between the film thickness and RRR values was obtained. As film thickness decreased, RRR also tended to decrease. This was attributed to increased electron scattering at material interfaces, resulting in higher low-temperature electrical resistivity, and consequently lower RRR. The experimental assessment of the aging and storage conditions showed that 75 and 77 days of aging in air and dry conditions, respectively, did not have a significant effect on the RRR behavior of silver thin films.

This thesis provides a deeper understanding of the temperature dependence of electrical and thermal properties of silver thin films on the fabrication process, purity, thickness, and aging and storage. The results highlight that there is a relationship between the microstructure and electrical properties. This research offers insights into the potential of controlling microstructure and product design to achieve the desired electrical conductivity performance without generating excessive heat load for cryogenic quantum cabling.

5.2. Future Recommendations

In order to further extend the understanding of the RRR behavior with changing processing and design parameters, the following recommendations are made for future work:

- To ensure qualitative results, it is advisable to conduct a systematic investigation of heat treatment parameters namely time, duration and ambient gas, as well as heating and cooling rates. The distinct microstructures resulting from the oven and lamination heat treatments showed the significant influence of these heat treatment parameters, leading to different RRR values. Therefore, for future research, it is recommended to optimize these heat treatment parameters to achieve the desired electrical and thermal properties through microstructural evolution. Additionally, SEM pictures of the laminator-treated samples revealed the potential effects of a vacuum environment during heat treatment in obtaining finer microstructure. Further exploration of vacuum annealing's capacity to optimize RRR through control of the microstructure is recommended.
- To exclude the possibility of the white surface finish being a different chemical composition, it is recommended to conduct an X-ray Fluorescence (XRF) analysis. This analytical technique can reveal the elemental composition of the silver film. This provides insights on the chemical composition beyond what XRD could offer in terms of the phase composition and crystal structure, which were not sufficient to detect any difference between the sample with a white surface finish and the one with a shiny look.
- To validate the dewetting theory proposed for the white surface finish, a cross-section analysis is recommended. This analysis can potentially reveal the detachments of the silver film from the PI substrate. Despite efforts made in this thesis, it was not possible to achieve a brittle cut on the sample to investigate the cross-section. Therefore, it is suggested to utilize the focused ion beam machine to obtain a clean cross-sectional cut.
- To address specific requirements for electrical and thermal properties of silver thin films, it is recommended to develop a dynamic model. This model should provide an estimated performance assessment in terms of thermal load by processing the RRR data of the samples with varying fabrication and design characteristics.

References

(1) Alexeev, Y., Bacon, D., Brown, K. R., Calderbank, R., Carr, L. D., Chong, F. T., DeMarco, B., Englund, D., Farhi, E., Fefferman, B., et al. (2021). Quantum computer systems for scientific discovery. *PRX Quantum 2*, 017001.

(2) Tennie, F., and Palmer, T. (2023). Quantum Computers for Weather and Climate Prediction: The Good, the Bad, and the Noisy. *Bulletin of the American Meteorological Society 104*, E488–E500.

(3) Almudever, C. G., Lao, L., Fu, X., Khammassi, N., Ashraf, I., Iorga, D., Varsamopoulos, S., Eichler, C., Wallraff, A., Geck, L., et al. In *Design, Automation & Test in Europe Conference & Exhibition (DATE), 2017*, 2017, pp 836–845.

(4) Chen, J.-J., An, Q., Rodriguez, R. D., Sheremet, E., Wang, Y., Sowade, E., Baumann, R. R., and Feng, Z.-S. (2019). Surface modification with special morphology for the metallization of polyimide film. *Applied Surface Science 487*, 503–509.

(5) Naghdi, S., Rhee, K., Hui, D., and Park, S. (2018). A Review of Conductive Metal Nanomaterials as Conductive, Transparent, and Flexible Coatings, Thin Films, and Conductive Fillers: Different Deposition Methods and Applications. *Coatings 8*, 278.

(6) Wang, T., Wang, X., Yang, B., Chen, X., and Liu, J. (2017). Selective Patterning of Conductive Silver on Polyimide Film by Localized Microplasma Reduction and Electroless Deposition. *Journal of The Electrochemical Society 164*, D282–D288.

(7) Yin, C., Wang, S. H., and Liu, D. L. In 2016.

(8) Smith, D. R., and Fickett, F. (1995). Low-temperature properties of silver. *Journal of research of the National Institute of Standards and Technology 100*, 119.

(9) Bishop, C. A. In *Vacuum Deposition Onto Webs, Films and Foils*; Elsevier: 2015, pp 13–55.

(10) Delft Circuits Quantum Computing hardware `https://delft-circuits.com/applications/quantum-computation/` (accessed Apr. 9, 2023).

(11) Gates, B. D. (2009). Flexible Electronics. *Science 323*, 1566–1567.

(12) Ventura, G., and Perfetti, M., *Thermal Properties of Solids at Room and Cryogenic Temperatures*; Springer Netherlands: 2014.

(13) Reed, R. P., Clark, A. F., and Rubin, L. G. (1984). Materials at Low Temperatures. *Physics Today 37*, 97–97.

(14) Ekin, J., *Experimental Techniques for Low-Temperature Measurements*; Oxford University PressOxford: 2006.

(15) Ziman, J., *Electrons and Phonons: The Theory of Transport Phenomena in Solids*; International series of monographs on physics; Clarendon Press: 1960.

(16) Ashcroft, N. W., *Solid state physics*; Holt, Rinehart and Winston: 1976, p 826.

(17) Morris, R. B., Franta, D. J., and White, H. S. (1987). Electrochemistry at platinum bane electrodes of width approaching molecular dimensions: breakdown of transport equations at very small electrodes. *The Journal of Physical Chemistry 91*, 3559–3564.

(18) Matthiessen, A., and Foster, G. C. (1863). XLII.—Researches into the chemical constitution of narcotine, and of its products of decomposition.—Part I. *J. Chem. Soc. 16*, 342–364.

(19) Naumann, R. J., *Introduction to the Physics and Chemistry of Materials*; CRC Press: 2008.

(20) Böer, K. W., and Pohl, U. W., *Semiconductor Physics*; Springer International Publishing: 2018.

(21) GRIMVALL, G. In *Thermophysical Properties of Materials*; Elsevier: 1999, pp 255–285.

(22) Devanathan, V. (2021). The Wiedemann-Franz Law for Electrical and Thermal Conduction in Metals. *4*, 1–26.

(23) Rosenberg, H. (1988). The Solid State: An Introduction to the Physics of Crystals for Students of Physics. *Materials Science, and Engineering, 3rd ed.(Oxford University Press, Oxford, New York, 1988)*, 326.

(24) Harsha, P. K. S. S., *Principles of Vapor Deposition of Thin Films*; Elsevier Science: 2006, p 1176.

(25) Ohring, M., *Materials Science of Thin Films*; Elsevier Science & Technology Books: 2001.

(26) Mavukkandy, M. O., McBride, S. A., Warsinger, D. M., Dizge, N., Hasan, S. W., and Arafat, H. A. (2020). Thin film deposition techniques for polymeric membranes– A review. *Journal of Membrane Science 610*, 118258.

(27) Abegunde, O. O., Akinlabi, E. T., Oladijo, O. P., Akinlabi, S., and and, A. U. U. (2019). Overview of thin film deposition techniques. *AIMS Materials Science 6*, 174–199.

(28) Martín-Palma, R. J., and Lakhtakia, A. In *Engineered Biomimicry*; Elsevier: 2013, pp 383–398.

(29) Pargellis, A. N. (1989). Evaporating and sputtering: Substrate heating dependence on deposition rate. *Journal of Vacuum Science & Technology A: Vacuum, Surfaces, and Films 7*, 27–30.

(30) In *Handbook of Thick- and Thin-Film Hybrid Microelectronics*; John Wiley & Sons, Inc.: 2004, pp 180–220.

(31) Kelly, P., and Arnell, R. (2000). Magnetron sputtering: a review of recent developments and applications. *Vacuum 56*, 159–172.

(32) Gao, W., Li, Z., and Sammes, N., *An Introduction to Electronic Materials for Engineers*; WORLD SCIENTIFIC: 2011.

(33) Tominaga, K., Adachi, H., and Wasa, K. In *Handbook of Sputtering Technology*; Elsevier: 2012, pp 361–520.

(34) Shiosaki, T., Ohnishi, S., Murakami, Y., and Kawabata, A. (1978). High rate epitaxial growth of ZnO films on sapphire by planar magnetron rf sputtering system. *Journal of Crystal Growth 45*, 346–349.

(35) Thornton, J. A. (1974). Influence of apparatus geometry and deposition conditions on the structure and topography of thick sputtered coatings. *Journal of Vacuum Science and Technology 11*, 666–670.

(36) Movchan, B. A., and Demchishin, A. V. In 1969.

(37) Thornton, J. A. (1975). Influence of substrate temperature and deposition rate on structure of thick sputtered Cu coatings. *Journal of Vacuum Science and Technology 12*, 830–835.

(38) Callister, W., and Rethwisch, D., *Materials Science and Engineering: An Introduction, 8th Edition*; Wiley: 2009.

(39) Singer, X., Wen, H., Singer, W., and Möller, W. (2003). PROPERTIES AND STRUCTURE OF ELECTRODEPOSITED COPPER LAYERS IN PARTS OF THE TTF MAIN COUPLER.

(40) Fouaidy, M., and Hammoudi, N. (2006). RRR of copper coating and low temperature electrical resistivity of material for TTF couplers. *Physica C: Superconductivity 441*, 137–144.

(41) Sahu, D., Chen, C., Lin, S., and Huang, J.-L. (2006). Effect of substrate temperature and annealing treatment on the electrical and optical properties of silver-based multilayer coating electrodes. *Thin Solid Films 515*, 932–935.

(42) Jung, Y. S., Choi, Y. W., Lee, H. C., and Lee, D. W. (2003). Effects of thermal treatment on the electrical and optical properties of silver-based indium tin oxide/metal/indium tin oxide structures. *Thin Solid Films 440*, 278–284.

(43) Klöppel, A., Kriegseis, W., Meyer, B., Scharmann, A., Daube, C., Stollenwerk, J., and Trube, J. (2000). Dependence of the electrical and optical behaviour of ITO–silver–ITO multilayers on the silver properties. *Thin Solid Films 365*, 139–146.

(44) Dannenberg, R., Stach, E., Groza, J. R., and Dresser, B. J. (2000). TEM annealing study of normal grain growth in silver thin films. *Thin Solid Films 379*, 133–138.

(45) Aoshima, Y., Miyazaki, M., Sato, K., Akao, Y., Takaki, S., and Adachi, K. (2000). Development of Silver-Based Multilayer Coating Electrodes with Low Resistance for Use in Flat Panel Displays. *Japanese Journal of Applied Physics 39*, 4884.

(46) Arbab, M. (2001). The base layer effect on the d.c. conductivity and structure of direct current magnetron sputtered thin films of silver. *Thin Solid Films 381*, 15–21.

(47) Hajakbari, F., and Ensandoust, M. (2016). Study of Thermal Annealing Effect on the Properties of Silver Thin Films Prepared by DC Magnetron Sputtering. *Acta Physica Polonica A 129*, 680–682.

(48) Santbergen, R, Temple, T. L., Liang, R, Smets, A. H. M., van Swaaij, R. A. C. M. M., and Zeman, M (2012). Application of plasmonic silver island films in thin-film silicon solar cells. *Journal of Optics 14*, 024010.

(49) Hsieh, J., Li, C., Wu, Y., and Jang, S. (2011). Optoelectronic properties of sputter-deposited Ag–SiO2 nanoparticle films by rapid thermal annealing. *Current Applied Physics 11*, S328–S332.

(50) Omar, M. A., *Elementary solid state physics: principles and applications*; Pearson Education India: 1975.

(51) Fellmuth, B., and Gaiser, C. (2021). Residual resistance ratio as indicator for the influence of impurities on fixed-point temperatures. *Metrologia 58*, 035013.

(52) Mimura, K., Ishikawa, Y., Isshiki, M., and Kato, M. (1997). Precise Purity-Evaluation of High-Purity Copper by Residual Resistivity Ratio. *Materials Transactions, JIM 38*, 714–718.

(53) Luo, E. Z., Heun, S., Kennedy, M., Wollschläger, J., and Henzler, M. (1994). Surface roughness and conductivity of thin Ag films. *Physical Review B 49*, 4858–4865.

(54) Pal, A. K., and Mohan, D. B. (2015). Structural, morphological and optical properties of Ag–AgO thin films with the effect of increasing film thickness and annealing temperature. *Optical Materials 48*, 121–132.

(55) Indiamart Silver Granules `https://www.indiamart.com/proddetail/silver-granules-24325774373.html` (accessed Oct. 10, 2023).

(56) caplinq Polyamide Film with 0.5mil FEP on One Side `https://www.caplinq.com/1mil-fn-polyimide-film-with-0.5mil-fep-on-one-side-no-adhesive-pit1n-fep019-series.html` (accessed Oct. 10, 2023).

(57) Engineering, A. Substrate Stage Assembly, Delft Circuits internal document, 2020.

(58) Osman, I. M., Abdalla, M. D., Elfaki, A. H., Yagoub, K. Y., Hussein, K. I., Eldoma, A. M., Al-atta, N. O., and Siddig, Y. M. O. (2021). Effects of additive and gamma irradiation on the structural and optical properties of polyvinyl alcohol doped with silver nitrate. *GSJ 9*, 1780–1792.

(59) Skipper, N. T., and Neilson, G. W. (1989). X-ray and neutron diffraction studies on concentrated aqueous solutions of sodium nitrate and silver nitrate. *Journal of Physics: Condensed Matter 1*, 4141.

(60) Thompson, C. V. (2012). Solid-State Dewetting of Thin Films. *Annual Review of Materials Research 42*, 399–434.

(61) Presland, A., Price, G., and Trimm, D. (1972). Hillock formation by surface diffusion on thin silver films. *Surface Science 29*, 424–434.

(62) Jacquet, P., Podor, R., Ravaux, J., Teisseire, J., Gozhyk, I., Jupille, J., and Lazzari, R. (2016). Grain growth: The key to understand solid-state dewetting of silver thin films. *Scripta Materialia 115*, 128–132.

(63) Cho, C.-Y., Chang, J.-C., Cai, M.-X., Lin, P.-T., and Yang, Y.-J. (2022). Dewetting Process of Silver Thin Films and Its Application on Percolative Pressure Sensors with High Sensitivity. *Polymers 15*, 180.

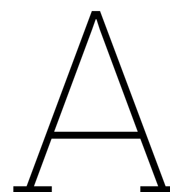

Sample Data

Sample ID	Purity	Thickness (μm)	Deposition Run ID	R_RT (Ω)	R_LiqHe (Ω)	RRR
RRRS_HT_L0_1.json	4N	2	230801	7.82	0.19	40.96
RRRS_HT_L0_2.json	4N	2	230801	8.29	0.19	43.58
RRRS_HT_L0_3.json	4N	2	230801	7.77	0.18	42.85
RRRS_HT_L0_4.json	4N	2	230801	7.65	0.19	40.78
RRRS_HT_L0_5.json	4N	2	230801	8.34	0.41	20.53
RRRS_HT_L0_6.json	4N	2	230801	7.60	0.18	41.96
RRRS_HT_L1_1.json	4N	2	230801	7.87	0.15	51.97
RRRS_HT_L1_2.json	4N	2	230801	7.70	0.15	53.04
RRRS_HT_L1_3.json	4N	2	230801	8.15	0.15	52.68
RRRS_HT_L1_4.json	4N	2	230801	7.65	0.13	57.81
RRRS_HT_L1_5.json	4N	2	230801	8.25	0.14	59.04
RRRS_HT_L1_6.json	4N	2	230801	7.71	0.14	55.81
RRRS_HT_L3_1.json	4N	2	230801	8.04	0.14	58.65
RRRS_HT_L3_2.json	4N	2	230801	7.73	0.15	50.17
RRRS_HT_L3_3.json	4N	2	230801	7.66	0.16	48.90
RRRS_HT_L3_4.json	4N	2	230801	7.63	0.14	53.56
RRRS_HT_L3_5.json	4N	2	230801	7.60	0.14	54.37
RRRS_HT_L3_6.json	4N	2	230801	7.87	0.13	58.53
RRRS_HT_L4_1.json	4N	2	230801	8.14	0.25	32.46
RRRS_HT_L4_2.json	4N	2	230801	7.91	0.22	36.34
RRRS_HT_L4_3.json	4N	2	230801	8.24	0.22	38.19
RRRS_HT_L4_4.json	4N	2	230801	7.73	0.13	60.20
RRRS_HT_L4_5.json	4N	2	230801	8.05	0.16	51.40
RRRS_HT_L4_6.json	4N	2	230801	8.05	0.17	47.33
RRRS_NHT_L0_1.json	4N	2	230801	9.21	0.57	16.11
RRRS_NHT_L0_2.json	4N	2	230801	8.90	0.56	16.00
RRRS_NHT_L0_3.json	4N	2	230801	9.25	0.65	14.27
RRRS_NHT_L0_4.json	4N	2	230801	9.25	0.55	16.81
RRRS_NHT_L0_5.json	4N	2	230801	8.97	0.54	16.63
RRRS_NHT_L0_6.json	4N	2	230801	9.15	0.61	15.06
RRRS_NHT_L1_1.json	4N	2	230801	7.92	0.14	55.85
RRRS_NHT_L1_2.json	4N	2	230801	7.76	0.13	61.85
RRRS_NHT_L1_3.json	4N	2	230801	8.02	0.13	61.19
RRRS_NHT_L1_4.json	4N	2	230801	7.82	0.13	59.61
RRRS_NHT_L1_5.json	4N	2	230801	9.29	0.72	12.89

Table A.1 continued from previous page

Sample ID	Purity	Thickness (μm)	Deposition Run ID	R_RT (Ω)	R_LiqHe (Ω)	RRR
RRRS_NHT_L1_6.json	4N	2	230801	8.16	0.14	58.71
RRRS_NHT_L3_1.json	4N	2	230801	8.03	0.13	63.16
RRRS_NHT_L3_2.json	4N	2	230801	7.66	0.13	61.09
RRRS_NHT_L3_3.json	4N	2	230801	7.92	0.12	66.28
RRRS_NHT_L3_4.json	4N	2	230801	7.91	0.13	61.34
RRRS_NHT_L3_5.json	4N	2	230801	7.69	0.12	62.63
RRRS_NHT_L3_6.json	4N	2	230801	7.85	0.12	63.91
RRRS_NHT_L4_1.json	4N	2	230801	8.06	0.14	58.48
RRRS_NHT_L4_2.json	4N	2	230801	7.74	0.13	60.74
RRRS_NHT_L4_3.json	4N	2	230801	7.99	0.12	66.00
RRRS_NHT_L4_4.json	4N	2	230801	7.81	0.13	61.90
RRRS_NHT_L4_5.json	4N	2	230801	7.97	0.13	59.40
RRRS_NHT_L4_6.json	4N	2	230801	7.83	0.12	64.34

Table A.1: Resistance measurement details of samples from the deposition run 230801

Sample ID	Purity	Thickness (μm)	Deposition Run ID	R_RT (Ω)	R_LiqHe (Ω)	RRR
RRRS231907_3N5_HT_L0_1.json	3N5	2	231907	8.34	0.66	12.55
RRRS231907_3N5_HT_L0_2.json	3N5	2	231907	8.78	0.72	12.21
RRRS231907_3N5_HT_L0_3.json	3N5	2	231907	8.44	0.67	12.57
RRRS231907_3N5_HT_L0_4.json	3N5	2	231907	8.38	0.67	12.48
RRRS231907_3N5_HT_L0_5.json	3N5	2	231907	8.24	0.67	12.28
RRRS231907_3N5_HT_L0_6.json	3N5	2	231907	9.08	0.74	12.26
RRRS231907_3N5_HT_L1_1.json	3N5	2	231907	8.34	0.36	23.47
RRRS231907_3N5_HT_L1_2.json	3N5	2	231907	8.33	0.36	23.06
RRRS231907_3N5_HT_L1_3.json	3N5	2	231907	8.04	0.38	21.13
RRRS231907_3N5_HT_L1_4.json	3N5	2	231907	7.84	0.36	21.60
RRRS231907_3N5_HT_L1_6.json	3N5	2	231907	7.79	0.35	22.17
RRRS231907_3N5_HT_L3_1.json	3N5	2	231907	8.31	0.34	24.14
RRRS231907_3N5_HT_L3_2.json	3N5	2	231907	8.69	0.37	23.53
RRRS231907_3N5_HT_L3_3.json	3N5	2	231907	7.86	0.32	24.91
RRRS231907_3N5_HT_L3_4.json	3N5	2	231907	7.17	0.32	22.76
RRRS231907_3N5_HT_L3_5.json	3N5	2	231907	8.46	0.34	24.68
RRRS231907_3N5_HT_L4_1.json	3N5	2	231907	8.58	0.35	24.69
RRRS231907_3N5_HT_L4_2.json	3N5	2	231907	8.61	0.34	25.62
RRRS231907_3N5_HT_L4_3.json	3N5	2	231907	8.11	0.32	25.67
RRRS231907_3N5_HT_L4_4.json	3N5	2	231907	8.06	0.33	24.66
RRRS231907_3N5_HT_L4_5.json	3N5	2	231907	8.44	0.34	24.57
RRRS231907_3N5_HT_L4_6.json	3N5	2	231907	8.78	0.35	25.43
RRRS231907_3N5_NHT_L0_1.json	3N5	2	231907	8.94	1.09	8.20
RRRS231907_3N5_NHT_L0_2.json	3N5	2	231907	8.95	1.10	8.13
RRRS231907_3N5_NHT_L0_3.json	3N5	2	231907	9.32	1.13	8.26
RRRS231907_3N5_NHT_L0_4.json	3N5	2	231907	9.15	1.10	8.33
RRRS231907_3N5_NHT_L0_5.json	3N5	2	231907	8.89	1.08	8.24
RRRS231907_3N5_NHT_L0_6.json	3N5	2	231907	9.14	1.12	8.14
RRRS231907_3N5_NHT_L1_1.json	3N5	2	231907	7.88	0.20	38.72
RRRS231907_3N5_NHT_L1_2.json	3N5	2	231907	7.92	0.20	39.03
RRRS231907_3N5_NHT_L1_3.json	3N5	2	231907	7.76	0.20	39.34
RRRS231907_3N5_NHT_L1_4.json	3N5	2	231907	8.31	0.21	39.42
RRRS231907_3N5_NHT_L1_5.json	3N5	2	231907	7.88	0.20	38.86

Table A.2 continued from previous page

Sample ID	Purity	Thickness (μm)	Deposition Run ID	R_RT (Ω)	R_LiqHe (Ω)	RRR
RRRS231907_3N5_NHT_L1_6.json	3N5	2	231907	8.12	0.21	38.35
RRRS231907_3N5_NHT_L3_1.json	3N5	2	231907	7.77	0.19	40.48
RRRS231907_3N5_NHT_L3_2.json	3N5	2	231907	8.12	0.20	40.19
RRRS231907_3N5_NHT_L3_3.json	3N5	2	231907	7.78	0.19	40.56
RRRS231907_3N5_NHT_L3_4.json	3N5	2	231907	8.12	0.20	40.08
RRRS231907_3N5_NHT_L3_5.json	3N5	2	231907	7.90	0.20	40.26
RRRS231907_3N5_NHT_L3_6.json	3N5	2	231907	7.91	0.20	40.48
RRRS231907_3N5_NHT_L4_1.json	3N5	2	231907	7.89	0.20	39.69
RRRS231907_3N5_NHT_L4_2.json	3N5	2	231907	7.87	0.20	39.34
RRRS231907_3N5_NHT_L4_3.json	3N5	2	231907	8.07	0.20	40.49
RRRS231907_3N5_NHT_L4_4.json	3N5	2	231907	7.75	0.19	40.36
RRRS231907_3N5_NHT_L4_5.json	3N5	2	231907	7.71	0.19	40.49
RRRS231907_3N5_NHT_L4_6.json	3N5	2	231907	8.03	0.20	40.68

Table A.2: Resistance measurement details of samples from the deposition run 231907

Sample ID	Purity	Thickness (μm)	Deposition Run ID	R_RT (Ω)	R_LiqHe (Ω)	RRR
RRRS231805_3N5_HT_1.json	3N5	2	231805	7.91	0.29	27.30
RRRS231805_3N5_HT_2.json	3N5	2	231805	8.48	0.31	26.95
RRRS231805_3N5_HT_3.json	3N5	2	231805	7.77	0.58	13.31
RRRS231805_3N5_HT_4.json	3N5	2	231805	8.42	0.44	19.08
RRRS231805_3N5_HT_5.json	3N5	2	231805	7.93	0.30	26.77
RRRS231805_3N5_HT_6.json	3N5	2	231805	8.52	0.71	12.01
RRRS231805_3N5_NHT_1.json	3N5	2	231805	9.62	1.06	9.08
RRRS231805_3N5_NHT_2.json	3N5	2	231805	8.94	0.99	9.01
RRRS231805_3N5_NHT_3.json	3N5	2	231805	9.31	1.02	9.13
RRRS231805_3N5_NHT_4.json	3N5	2	231805	9.23	1.02	9.04
RRRS231805_3N5_NHT_5.json	3N5	2	231805	8.84	0.99	8.96
RRRS231805_3N5_NHT_6.json	3N5	2	231805	9.16	1.02	9.00

Table A.3: Resistance measurement details of samples from the deposition run 231805

Sample ID	Purity	Thickness (μm)	Deposition Run ID	R_RT (Ω)	R_LiqHe (Ω)	RRR
RRRS232202_250nm_HT_L0_1.json	3N8	0.25	232202	107.58	14.82	7.26
RRRS232202_250nm_HT_L0_2.json	3N8	0.25	232202	48.92	8.91	5.49
RRRS232202_250nm_HT_L0_3.json	3N8	0.25	232202	77.37	8.62	8.97
RRRS232202_250nm_HT_L0_4.json	3N8	0.25	232202	79.88	8.95	8.92
RRRS232202_250nm_HT_L0_5.json	3N8	0.25	232202	102.01	13.91	7.33
RRRS232202_250nm_HT_white_L0_1.json	3N8	0.25	232202	96.05	19.83	4.84
RRRS232202_250nm_HT_white_L0_2.json	3N8	0.25	232202	90.09	17.68	5.10
RRRS232202_250nm_HT_white_L0_3.json	3N8	0.25	232202	86.46	17.40	4.97
RRRS232202_250nm_HT_white_L0_4.json	3N8	0.25	232202	89.35	17.89	4.99
RRRS232202_250nm_HT_white_L0_5.json	3N8	0.25	232202	93.67	18.83	4.98
RRRS232202_250nm_HT_white_L0_6.json	3N8	0.25	232202	90.40	17.48	5.17
RRRS232202_250nm_NHT_L0_1.json	3N8	0.25	232202	86.09	15.84	5.43
RRRS232202_250nm_NHT_L0_2.json	3N8	0.25	232202	84.72	15.48	5.47
RRRS232202_250nm_NHT_L0_3.json	3N8	0.25	232202	86.10	16.32	5.27
RRRS232202_250nm_NHT_L0_4.json	3N8	0.25	232202	82.41	15.11	5.45

Table A.4 continued from previous page

Sample ID	Purity	Thickness (μm)	Deposition Run ID	R_RT (Ω)	R_LiqHe (Ω)	RRR
RRRS232202_2um_HT_L0_1.json	3N8	2	232202	8.04	0.31	25.66
RRRS232202_2um_HT_L0_2.json	3N8	2	232202	8.41	0.35	24.06
RRRS232202_2um_HT_L0_3.json	3N8	2	232202	8.00	0.27	29.62
RRRS232202_2um_HT_L0_4.json	3N8	2	232202	7.66	0.25	30.05
RRRS232202_2um_HT_L0_6.json	3N8	2	232202	7.78	0.26	29.76
RRRS232202_2um_NHT_L0_1.json	3N8	2	232202	8.77	1.05	8.33
RRRS232202_2um_NHT_L0_2.json	3N8	2	232202	8.96	1.08	8.28
RRRS232202_2um_NHT_L0_3.json	3N8	2	232202	8.79	1.06	8.31
RRRS232202_2um_NHT_L0_4.json	3N8	2	232202	9.72	1.19	8.17
RRRS232202_2um_NHT_L0_5.json	3N8	2	232202	9.36	1.14	8.24
RRRS232202_2um_NHT_L0_6.json	3N8	2	232202	8.82	1.07	8.28

Table A.4: Resistance measurement details of samples from the deposition run 232202. Samples with white surface finish are labeled as "white" in their sample IDs.

Sample ID	Purity	Thickness (μm)	Deposition Run ID	R_RT (Ω)	R_LiqHe (Ω)	RRR
RRRS232301_250nm_HT_L0_1.json	3N8	0.25	232301	83.42	14.90	5.60
RRRS232301_250nm_HT_L0_2.json	3N8	0.25	232301	85.00	15.20	5.59
RRRS232301_250nm_HT_L0_3.json	3N8	0.25	232301	81.70	14.67	5.57
RRRS232301_250nm_HT_L0_4.json	3N8	0.25	232301	82.82	14.87	5.57
RRRS232301_250nm_HT_L0_5.json	3N8	0.25	232301	90.00	16.58	5.43
RRRS232301_250nm_HT_L0_6.json	3N8	0.25	232301	87.97	15.12	5.82
RRRS232301_250nm_HT_L1_1.json	3N8	0.25	232301	83.01	12.55	6.62
RRRS232301_250nm_HT_L1_2.json	3N8	0.25	232301	82.57	12.58	6.56
RRRS232301_250nm_HT_L1_3.json	3N8	0.25	232301	85.70	13.06	6.56
RRRS232301_250nm_HT_L1_4.json	3N8	0.25	232301	86.86	13.33	6.51
RRRS232301_250nm_HT_L1_5.json	3N8	0.25	232301	79.52	11.94	6.66
RRRS232301_250nm_HT_L1_6.json	3N8	0.25	232301	80.94	12.12	6.68
RRRS232301_250nm_HT_L3_1.json	3N8	0.25	232301	80.13	11.95	6.71
RRRS232301_250nm_HT_L3_2.json	3N8	0.25	232301	79.03	11.44	6.91
RRRS232301_250nm_HT_L3_3.json	3N8	0.25	232301	77.87	11.33	6.88
RRRS232301_250nm_HT_L3_4.json	3N8	0.25	232301	78.64	11.59	6.79
RRRS232301_250nm_HT_L3_5.json	3N8	0.25	232301	81.75	12.04	6.79
RRRS232301_250nm_HT_L3_6.json	3N8	0.25	232301	82.26	11.75	7.00
RRRS232301_250nm_HT_L4_1.json	3N8	0.25	232301	79.83	11.53	6.92
RRRS232301_250nm_HT_L4_2.json	3N8	0.25	232301	80.89	12.04	6.72
RRRS232301_250nm_HT_L4_3.json	3N8	0.25	232301	79.75	11.61	6.87
RRRS232301_250nm_HT_L4_4.json	3N8	0.25	232301	79.21	11.50	6.89
RRRS232301_250nm_HT_L4_5.json	3N8	0.25	232301	84.37	12.48	6.76
RRRS232301_250nm_HT_L4_6.json	3N8	0.25	232301	84.68	12.65	6.69
RRRS232301_250nm_NHT_L0_1.json	3N8	0.25	232301	82.25	13.89	5.92
RRRS232301_250nm_NHT_L0_2.json	3N8	0.25	232301	79.18	13.04	6.07
RRRS232301_250nm_NHT_L1_1.json	3N8	0.25	232301	72.62	5.77	12.59
RRRS232301_250nm_NHT_L1_2.json	3N8	0.25	232301	73.05	5.63	12.98
RRRS232301_250nm_NHT_L1_3.json	3N8	0.25	232301	69.98	5.27	13.28
RRRS232301_250nm_NHT_L1_4.json	3N8	0.25	232301	70.72	5.34	13.25
RRRS232301_250nm_NHT_L1_5.json	3N8	0.25	232301	70.78	5.07	13.97
RRRS232301_250nm_NHT_L3_1.json	3N8	0.25	232301	72.43	5.33	13.58
RRRS232301_250nm_NHT_L3_2.json	3N8	0.25	232301	71.52	5.29	13.51
RRRS232301_250nm_NHT_L3_3.json	3N8	0.25	232301	69.92	5.05	13.85

Table A.5 continued from previous page

Sample ID	Purity	Thickness (μm)	Deposition Run ID	R_RT (Ω)	R_LiqHe (Ω)	RRR
RRRS232301_250nm_NHT_L3_4.json	3N8	0.25	232301	68.61	4.97	13.79
RRRS232301_250nm_NHT_L3_5.json	3N8	0.25	232301	71.69	5.20	13.77
RRRS232301_250nm_NHT_L3_6.json	3N8	0.25	232301	74.55	5.43	13.72
RRRS232301_250nm_NHT_L4_1.json	3N8	0.25	232301	76.21	5.60	13.61
RRRS232301_250nm_NHT_L4_2.json	3N8	0.25	232301	74.32	5.46	13.61
RRRS232301_250nm_NHT_L4_3.json	3N8	0.25	232301	70.43	5.07	13.89
RRRS232301_250nm_NHT_L4_4.json	3N8	0.25	232301	70.05	5.01	13.99
RRRS232301_250nm_NHT_L4_5.json	3N8	0.25	232301	71.43	5.39	13.25

Table A.5: Resistance measurement details of samples from the deposition run 232301

Sample ID	Purity	Thickness (μm)	Deposition Run ID	R_RT (Ω)	R_LiqHe (Ω)	RRR
RRRS232702_1um_HT_L0_1.json	3N8	1	232702	16.77	1.10	15.28
RRRS232702_1um_HT_L0_2.json	3N8	1	232702	17.21	1.21	14.26
RRRS232702_1um_HT_L0_3_w.json	3N8	1	232702	17.86	1.55	11.55
RRRS232702_1um_HT_L0_4_w.json	3N8	1	232702	18.14	1.58	11.46
RRRS232702_1um_HT_L0_5.json	3N8	1	232702	17.96	1.12	15.97
RRRS232702_1um_HT_L1_1.json	3N8	1	232702	17.46	1.21	14.46
RRRS232702_1um_HT_L1_2.json	3N8	1	232702	17.95	1.26	14.19
RRRS232702_1um_HT_L1_3.json	3N8	1	232702	18.30	1.28	14.25
RRRS232702_1um_HT_L1_4.json	3N8	1	232702	17.73	1.27	13.97
RRRS232702_1um_HT_L1_5.json	3N8	1	232702	18.53	1.34	13.82
RRRS232702_1um_HT_L1_6.json	3N8	1	232702	17.37	1.22	14.19
RRRS232702_1um_HT_L3_1.json	3N8	1	232702	17.90	1.11	16.14
RRRS232702_1um_HT_L3_2.json	3N8	1	232702	18.28	1.11	16.41
RRRS232702_1um_HT_L3_3.json	3N8	1	232702	17.66	1.15	15.41
RRRS232702_1um_HT_L3_4.json	3N8	1	232702	17.53	1.09	16.07
RRRS232702_1um_HT_L3_5.json	3N8	1	232702	18.25	1.17	15.62
RRRS232702_1um_HT_L3_6.json	3N8	1	232702	17.06	1.09	15.63
RRRS232702_1um_HT_L4_1.json	3N8	1	232702	18.32	1.15	15.87
RRRS232702_1um_HT_L4_2.json	3N8	1	232702	18.67	1.20	15.55
RRRS232702_1um_HT_L4_3.json	3N8	1	232702	17.72	1.18	15.03
RRRS232702_1um_HT_L4_4.json	3N8	1	232702	17.36	1.12	15.53
RRRS232702_1um_HT_L4_5.json	3N8	1	232702	18.08	1.20	15.04
RRRS232702_1um_HT_L4_6.json	3N8	1	232702	18.11	1.23	14.69
RRRS232702_1um_NHT_L0_1.json	3N8	1	232702	19.12	2.45	7.79
RRRS232702_1um_NHT_L0_2.json	3N8	1	232702	19.25	2.45	7.85
RRRS232702_1um_NHT_L0_3.json	3N8	1	232702	19.87	2.51	7.92
RRRS232702_1um_NHT_L0_4.json	3N8	1	232702	19.35	2.47	7.84
RRRS232702_1um_NHT_L0_5.json	3N8	1	232702	19.29	2.46	7.85
RRRS232702_1um_NHT_L0_6.json	3N8	1	232702	18.49	2.39	7.74
RRRS232702_1um_NHT_L1_1.json	3N8	1	232702	17.60	0.63	27.74
RRRS232702_1um_NHT_L1_2.json	3N8	1	232702	17.00	0.61	27.92
RRRS232702_1um_NHT_L1_3.json	3N8	1	232702	17.03	0.62	27.30
RRRS232702_1um_NHT_L1_4.json	3N8	1	232702	16.79	0.59	28.43
RRRS232702_1um_NHT_L1_5.json	3N8	1	232702	16.41	0.59	27.88
RRRS232702_1um_NHT_L1_6.json	3N8	1	232702	16.91	0.61	27.53
RRRS232702_1um_NHT_L3_1.json	3N8	1	232702	16.89	0.59	28.67
RRRS232702_1um_NHT_L3_2.json	3N8	1	232702	16.66	0.59	28.41
RRRS232702_1um_NHT_L3_3.json	3N8	1	232702	17.07	0.57	29.88

Table A.6 continued from previous page

Sample ID	Purity	Thickness (μm)	Deposition Run ID	R_RT (Ω)	R_LiqHe (Ω)	RRR
RRRS232702_1um_NHT_L3_4.json	3N8	1	232702	16.40	0.55	29.81
RRRS232702_1um_NHT_L3_5.json	3N8	1	232702	17.13	0.57	29.87
RRRS232702_1um_NHT_L3_6.json	3N8	1	232702	16.41	0.55	30.01
RRRS232702_1um_NHT_L4_1.json	3N8	1	232702	16.74	0.54	30.76
RRRS232702_1um_NHT_L4_2.json	3N8	1	232702	16.98	0.54	31.16
RRRS232702_1um_NHT_L4_3.json	3N8	1	232702	16.15	0.53	30.76
RRRS232702_1um_NHT_L4_4.json	3N8	1	232702	16.76	0.56	30.06
RRRS232702_1um_NHT_L4_5.json	3N8	1	232702	16.22	0.52	30.89
RRRS232702_1um_NHT_L4_6.json	3N8	1	232702	17.05	0.56	30.23
RRRS232702_2um_HT_L0_1.json	3N8	2	232702	8.65	0.46	18.85
RRRS232702_2um_HT_L0_2.json	3N8	2	232702	8.34	0.43	19.27
RRRS232702_2um_HT_L0_3.json	3N8	2	232702	8.44	0.43	19.70
RRRS232702_2um_HT_L0_4.json	3N8	2	232702	8.78	0.48	18.41
RRRS232702_2um_HT_L0_5.json	3N8	2	232702	8.34	0.42	19.88
RRRS232702_2um_HT_L0_6.json	3N8	2	232702	8.70	0.46	18.87
RRRS232702_2um_NHT_L0_1.json	3N8	2	232702	9.14	1.05	8.74
RRRS232702_2um_NHT_L0_2.json	3N8	2	232702	9.20	1.05	8.80
RRRS232702_2um_NHT_L0_3.json	3N8	2	232702	8.94	1.02	8.78
RRRS232702_2um_NHT_L0_4.json	3N8	2	232702	9.40	1.06	8.88
RRRS232702_2um_NHT_L0_5.json	3N8	2	232702	9.08	1.02	8.86
RRRS232702_2um_NHT_L0_6.json	3N8	2	232702	9.35	1.06	8.81

Table A.6: Resistance measurement details of samples from the deposition run 232702. Samples with white surface finish are labeled with "w" in their sample IDs.

B

RRR vs Film Thickness

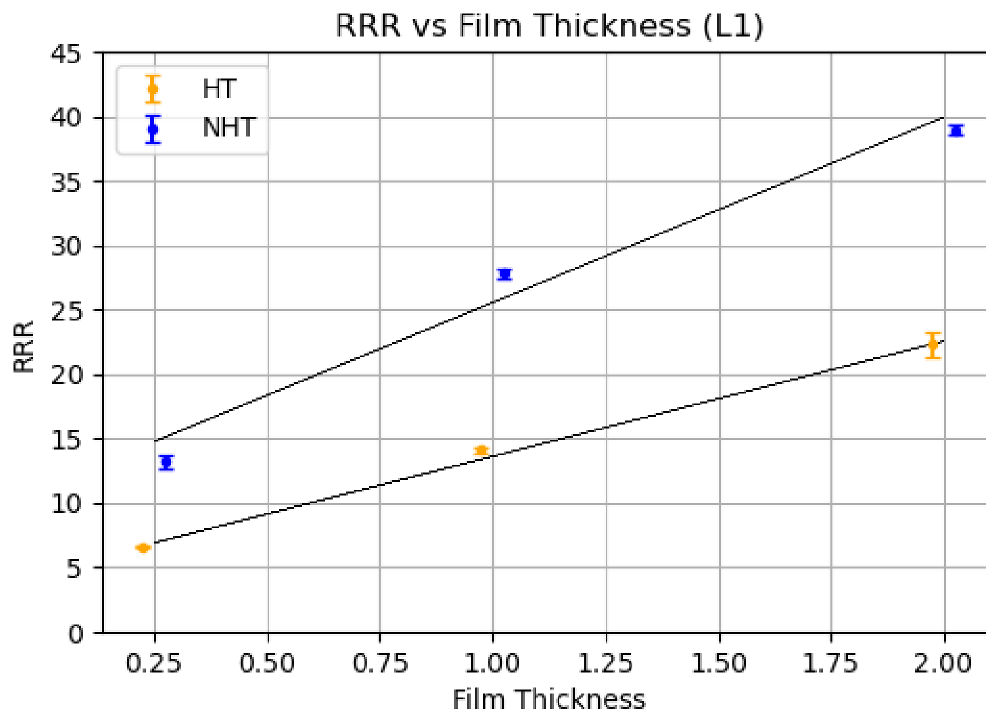

Figure B.1: The RRR behavior of the one-time laminated NHT and HT samples with respect to film thickness. The deposition runs are RRRS232301, RRRS232702 and RRRS231907 for the samples with thicknesses of 0.25, 1 and 2 μm, respectively. The silver purity is 3N8 for 0.25 and 1 μm thick samples, while 2 μm thick samples have 3N5 purity . All sets had six samples unless there is a failure during laser patterning. Solid circles represent the mean value of the set.

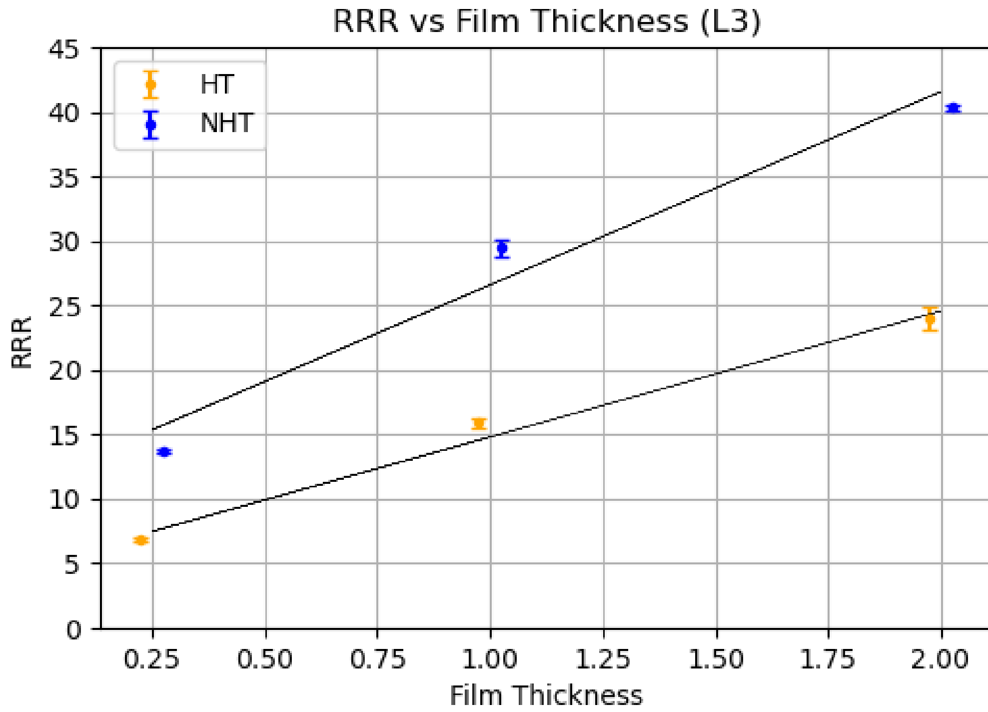

Figure B.2: The RRR behavior of the three-times laminated NHT and HT samples with respect to film thickness. The deposition runs are RRRS232301, RRRS232702 and RRRS231907 for the samples with thicknesses of 0.25, 1 and 2 μm, respectively. The silver purity is 3N8 for 0.25 and 1 μm thick samples, while 2 μm thick samples have 3N5 purity . All sets had six samples unless there is a failure during laser patterning. Solid circles represent the mean value of the set.

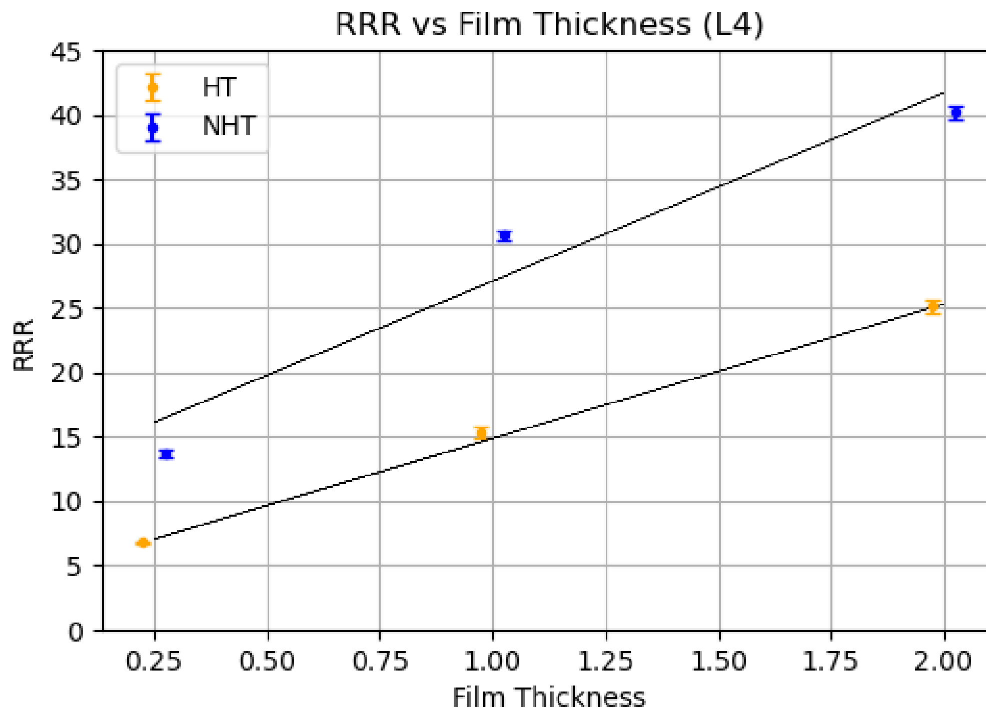

Figure B.3: The RRR behavior of the four-times laminated NHT and HT samples with respect to film thickness. The deposition runs are RRRS232301, RRRS232702 and RRRS231907 for the samples with thicknesses of 0.25, 1 and 2 μm, respectively. The silver purity is 3N8 for 0.25 and 1 μm thick samples, while 2 μm thick samples have 3N5 purity . All sets had six samples unless there is a failure during laser patterning. Solid circles represent the mean value of the set.

C

Additional Figures

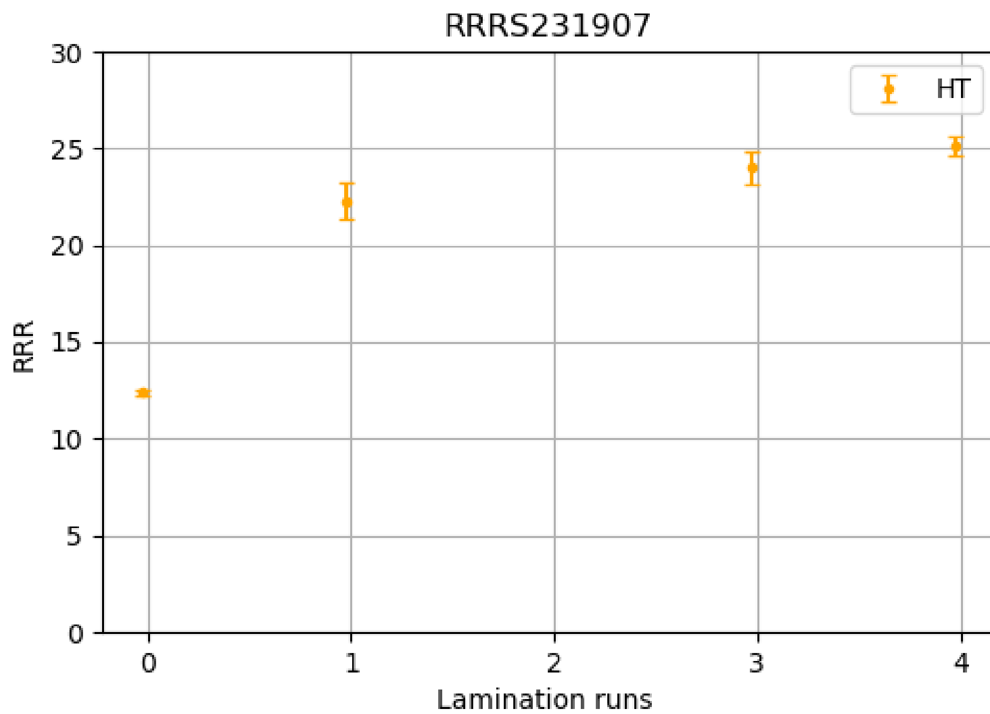

Figure C.1: The effect of several lamination runs on the RRR value of heat-treated (HT) samples with silver purity = 3N5 and film thickness = 2 μm. All sets had six samples. Solid circles represent the mean value of the set.

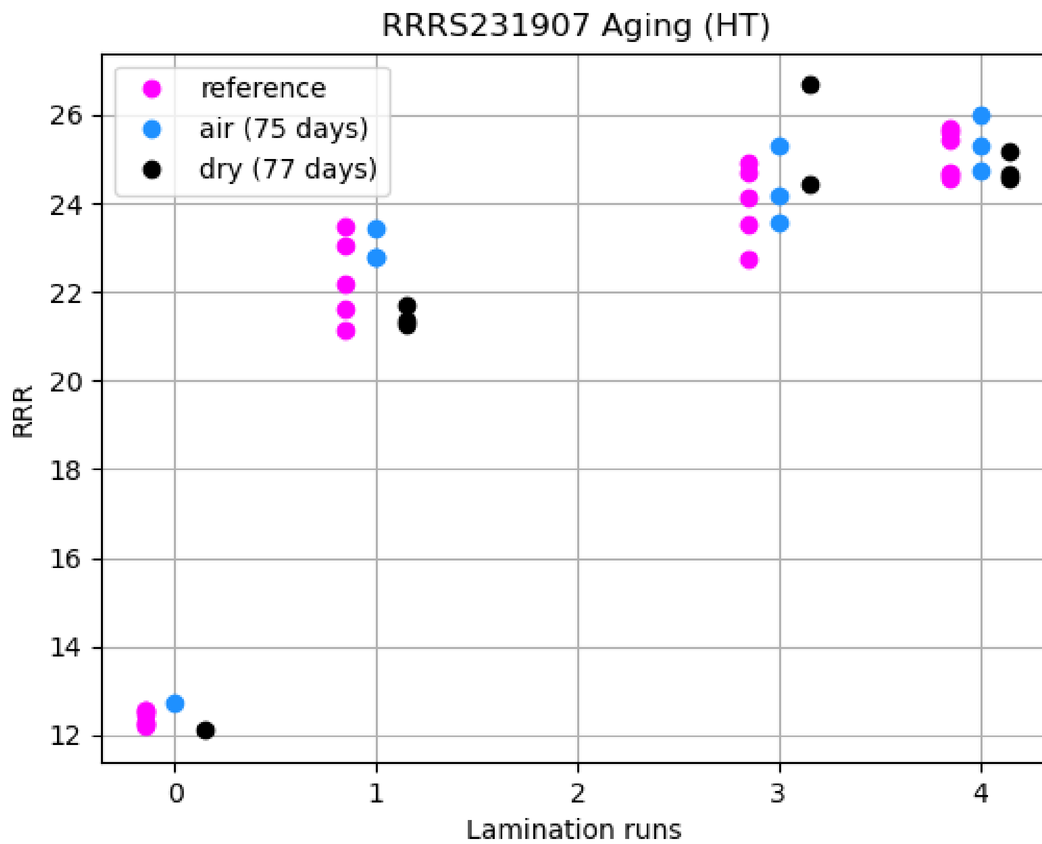

Figure C.2: The effect of aging and storage conditions on the RRR behavior of HT samples with respect to the increasing lamination run from none to four. The silver purity is 3N5 and the film thickness is 2 μm. Reference samples are measured no more than 12 days after the fabrication (see Table A.2) and had six samples for each set, while sample sets of air and dry storage were measured after 75 days and 77 days, respectively and had three samples unless there was an error during the measurements. Each point on the graph represents a sample.

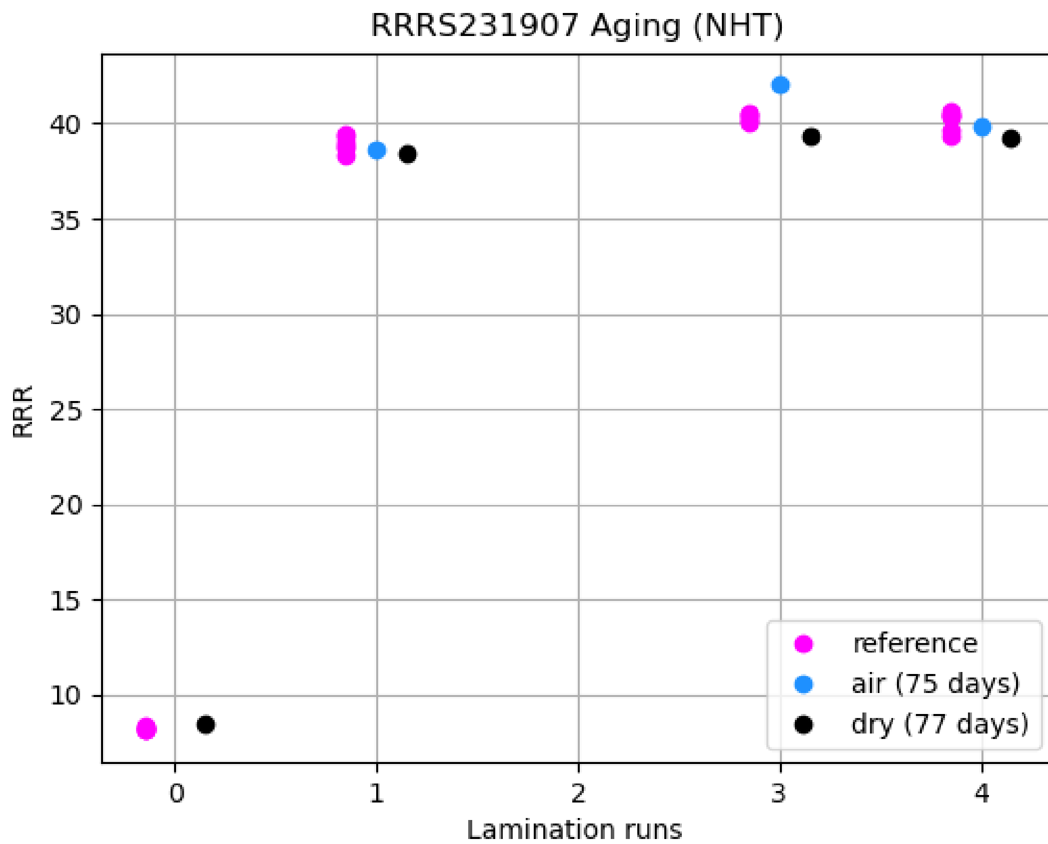

Figure C.3: The effect of aging and storage conditions on the RRR behavior of NHT samples with respect to the increasing lamination run from none to four. The silver purity is 3N5 and the film thickness is 2 μm. Reference samples are measured no more than 12 days after the fabrication (see Table A.2) and had six samples for each set, while sample sets of air and dry storage were measured after 75 days and 77 days, respectively and had three samples unless there was an error during the measurements. Each point on the graph represents a sample.